Department of Precision and Microsystems Engineering

Modelling of Laser Powder Bed Fusion processes in non-convex geometries with a semi-analytical approach

Ana Arrieta Rodríguez

Report no	: 2023.053
Coach	: Dr. Can Ayas
Professor	: Dr. Can Ayas
Specialisation	: Engineering Mechanics
Type of report	: Master Thesis
Date	: 31 August 2023

Delft
University of
Technology

Challenge the future

Modelling of Laser Powder Bed Fusion processes in non-convex geometries with a semi-analytical approach

by

Ana Arrieta Rodríguez

to obtain the degree of Master of Science
at the Delft University of Technology,
to be defended publicly on Thursday August 31, 2023 at 11:00 AM.

Student number:	5395992
Project duration:	September, 2021 – August 2023
Supervisor:	Dr. C. Ayas

Preface

This thesis concludes my studies at TU Deft. During this master thesis, I have been able to learn more and work on topics that have fascinate me since I started my engineering degree in Madrid. For that, I would like to thank Dr. Can Ayas for giving me the opportunity to develop this thesis, as well as guiding me through the project. Moreover, I would like to thank Yang Yang for his availability to help me and give me feedback at any time.

During the three years that I have been at TU Delft, I have been grateful for the constant support of my family and friends back home, specially throughout the tough times over the last couple of years. To all of the friends I have met in Delft, specially Inés, Elke, and Justin, thank you for all the good times at university and outside of it.

Specially, to my parents, thank you for always supporting my ambitions and pushing me to be the best version of myself. To my sisters, Amaia and Berta, thank you for being there for me and for the countless laughs. And to Dani, I am so grateful to have you with me throughout all these years, you have always supported me in every decision and believed in me, thank you.

Ana Arrieta Rodríguez
Delft, August 2023

Abstract

Laser Powder Bed Fusion (LPBF) is a metal additive manufacturing process in which a three-dimensional object is obtained by selectively melting and fusing a metallic powder with a heat source, such as a laser beam, in successive thin layers. This process allows to create lightweight parts with complex geometry. However, parts created by LPBF processes may present poor surface quality and can be prone to high residual stresses and deformations that arise during manufacturing. To be able to understand the process and investigate the relation between the thermal history of the part and the deformations that arise, researchers have proposed different thermal models in literature. Most of these models are purely numerical methods in which the temperature history is predicted by implementing finite element and finite difference schemes. However, a finer discretization is required to capture the steep temperature gradients that arise at the vicinity of the laser spot, which results in computational expensive models.

In the Precision and Microsystems Engineering (PME) Department at TU Delft, a semi-analytical approach was proposed to study the thermal history of LPBF processes. This method combines an analytical solution that captures the high spatial gradients of the laser beam and a numerical solution that corrects the analytical solution and enforces the boundary conditions. When the laser beam is near the boundary, the analytical solution is corrected first with the method of images, which dramatically reduces the computational cost when obtaining the solution. However, this approach is only valid for convex polyhedrons. If the domain is non-convex, the method of images cannot be applied. Therefore, the high spatial gradients have to be dealt with finer discretization, and the numerical correction's computational cost becomes prohibitive.

In this thesis, a thermal model is developed for LPBF processes using the semi-analytical approach with a modification in the method of images for non-convex polyhedrons. In this case, a correction to the method of images, denoted as anisotropic mirror sources, is introduced. This method allows to apply image sources to non-convex geometries. With this modification, the numerical correction in the semi-analytical method can be implemented with a coarse discretization with high computational efficiency.

Predictions of the proposed thermal model are compared to the predictions of a semi-analytical method without using the method of images. This comparison allows us to validate the proposed thermal model's computational efficiency as it can obtain the thermal history of non-convex polyhedrons in a computationally inexpensive manner. More importantly, the thermal model proposed demonstrates the possibility of using the method of images in non-convex polyhedrons.

Contents

List of Figures

List of Tables

1

Introduction

1.1. Additive Manufacturing

Additive manufacturing (AM) is the process of building three-dimensional objects from computer-aided design (CAD) models by adding material in successive thin layers. It is also known as 3D printing, additive fabrication, additive processes, rapid manufacturing and layer manufacturing [1]. AM is a very revolutionary technology as it allows to manufacture parts with complex geometries, it does not require molds to create the parts and reduces manufacturing costs. Its main applications are in the aerospace, automotive, and biomedical industries, among others.

The manufacturing process can be described as follows. A 3D drawing is created in a CAD software and sliced into thin layers of approximately 20 μm - 1 mm [2]. After this, the 3D object is built by successive deposition of individual layers in a build platform. There are different techniques developed in additive manufacturing depending on how the material is deposited, the type of heat source used, that is how heat is applied, and the state of the material before the printing process, which can be liquid, filament, solid or powder [1]. Stereolithography (SLA) and material jetting are processes that use liquid-state materials. These processes use photosensitive polymers as liquid resins and a UV light source is used as the heat source to cure the material. The difference between them is the way the material is deposited. In SLA once one layer is finished, the build platform lowers a distance equal to the layer thickness and a blade recoats the top with resin. On the other hand, material jetting deposits tiny droplets of the resin through multiple nozzles on the build platform [3]. Fused Deposition Modeling (FDM) is the process in which parts are built by deposition of thermoplastics in the form of filaments that are heated at the print head and then extruded through a nozzle to the platform. Laminated Object Manufacturing (LOM) utilizes solid material in the form of a sheet. In this case, a sheet of the material is first spread on the platform where a laser cuts the contour of the part and then a hot roller heats and compresses the sheet, bonding it with the layers underneath [1, 3]. For the case of powder-state processes, the most important AM technologies are Powder Bed Fusion (PBF) and Directed Energy Deposition (DED). PBF and DED are the most important technologies for metal additive manufacturing, in which a heat source, such as a laser or electron beam, is used to selectively melt a metallic powder into solid. The main difference between these processes is also how the material is deposited into the platform. In the case of DED, the powder is fed alongside the heat source simultaneously onto the platform, while in PBF, the powder bed is recoated with a blade with a new layer of powder once the scanning of the previous layer is finished.

For the last decade, AM has attracted much attention and become more relevant because of its numerous advantages. One of these advantages is the ability of reducing the process steps. Conventional manufacturing processes require multiple and iterative steps to built parts and, as the complexity increases, the number of steps does too. AM processes are able to built parts in a single step despite the complexity of the part. Moreover, the number of processes and resources are also reduced in AM. For example, the molding technology is a conventional technique that requires specific molds for different applications, which increases the resources and time necessary to built components. AM processes do not use molds, which reduces the use of resources for specific parts. Additionally, AM technologies are able to create lightweight structures due to the possibility of creating parts with complex geometry such as honeycomb or other shapes with cavities, which can improve the strength to weight ratio of parts [4, 5].

However, AM technologies present different challenges, such as poor part accuracy, limitation of materials, low production speed and limited part sizes. One of the main drawbacks of AM is the poor surface quality and creation of defects on the part. During manufacturing, pores can be created between the layers of the materials, as well as deformations and residual stresses. For example, in SLM this deformations and stresses are caused from thermal expansion and thermal contraction cycles [6]. On the other hand, AM technologies take more time to create parts compared to conventional methods, like casting or extrusion [7], because of the high resolution that is need to build parts. Processes such as SLS or SLM require a longer processing time and higher cost, which also limits the mass production of parts.

Nevertheless, AM technologies have been found to be beneficial to create parts for different industries, such as aerospace, automotive, and medicine, among others. The aerospace industry has been using AM technologies because of the possibility of manufacturing lightweight structures, as well as manufacturing components of complex geometry with advanced materials that are difficult and costly to manufacture. Furthermore, AM techniques are used to repair aircraft parts to reduce cost and extend the lifetime of components, such as compressors, turbine castings or blades [1]. In the automotive industry, the use of AM technologies to build automotive components has increased because it can reduce manufacturing and product costs and shorten the development cycle. It is also used because of the possibility of manufacturing complex components in small quantities and lightweight structures. Some components developed with AM processes are gear box components, engine exhausts and breaking systems [1, 8]. Biomedical parts for medical applications are built with AM technologies because of the ability of creating personalized parts in short fabrication series. With AM processes, customized prosthetic and implants of unique geometry can be obtained, as well as tissue and organ fabrication [1, 8].

1.2. Powder Bed Fusion

As mentioned previously, there are different AM techniques depending on the material used, how the material is deposited and the type of heat source applied. In the past thirty years, different metal additive manufacturing processes have been developed.

Powder Bed Fusion (PBF) is one of the most important technologies for metal additive manufacturing, in which a heat source is used to selectively melt a metallic powder into solid. It can be further divided in different processes, such as Selective Laser Sintering (SLS), Selective Laser Melting (SLM) and Electron Beam Melting (EBM), which are different due to the type of heat source used and how the material is deposited. For the case of SLS and SLM, which are laser powder bed fusion processes, a laser beam passes through lenses and is reflected by a mirror onto the build platform, where there is a layer of powder. After the layer is selectively melted, the platform moves downward and a recoating blade lays another layer of powder on top of the previous layer. This process continues on until the final part is completed. The main difference between SLM and SLS is that SLM completely melts the metal powder, instead of partially. Because the material is fully melted, the part does not require post processing in SLM. On the other hand, EBM uses an electron beam to selectively melt the powder bed. For this process, the electron beam is on top of the powder bed and it is controlled by a lens system. The powder is deposited on the platform via a powder hopper and a rake coats the powder on top of the previously melted layer. When finished, the platform is lowered and metal powder is deposited again [9].

Directed energy deposition (DED) is another important process for metal AM. The technique is similar to the PBF processes, but the main difference between them is the way the material is deposited on the platform. Figure 1.1 shows a comparison between powder bed fusion and directed energy deposition. DED processes use a moving heat source to melt metal powder flow or metal wire which is fed into the platform, instead of using a powder bed. The heat source used in DED can also be a laser or an electron beam [10].

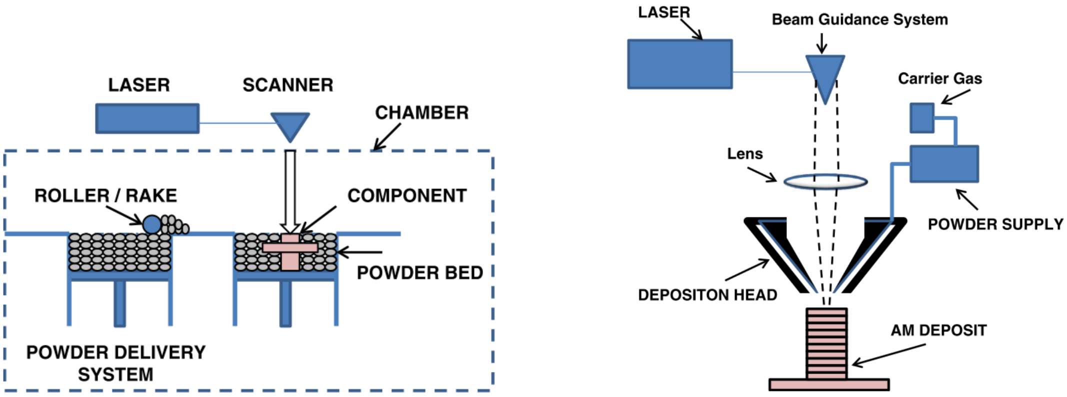

(a) (b)

Figure 1.1: Comparison between Powder Bed Fusion and Directed Energy Deposition. (a) Shows a schematic of the process of powder bed fusion, where the laser beam is reflected by a mirror onto a platform, and a layer of powder is laid by the recoating blade in the powder bed. (b) Shows a schematic of the process of directed energy deposition, where the powder is fed onto the platform from the deposition head instead of using a powder bed. Pictures are reproduced from [11].

As mentioned before, the main difference between PBF and DED is that the powder is pre-placed in the powder bed instead of being fed directly into the build plate. Apart from this, laser powder bed fusion (LPBF) has a much smaller effective heat source diameter than DED, generally 1/10th to 1/20th the size. Moreover, compared to DED, LPBF can use a lower range of power, around 100-250 W, and has a much faster deposition speed, between 50-1000 m/s. Due to the smaller size of the heat source in LPBF processes, a much finer resolution can be achieved in parts created by LPBF compared to DED builds [10]. Because of these advantages, LPBF processes are widely used in metal additive manufacturing and it will be studied in this thesis.

1.2.1. Multi-Laser Powder Bed Fusion

As mentioned in Section 1.1, lightweight components of great complexity can be built with additive manufacturing processes. However, there are two important limitations when using metal printing systems: the production speed is relatively low and the limited part sizes, due to the available build volume.

To be able to overcome these issues, different strategies have been proposed. To improve the build rate in LPBF, the strategy is to modify the process parameters, such as increasing the laser beam diameter, layer thickness and laser power to 1 mm, 200 μm and 1000 W, respectively [12]. Although, this can result in 10% loss of density and poor component geometry accuracy, as well as a decrease in the resolution [12]. Then, an alternative strategy is adding more laser beams to achieve high manufacturing build rates and high precision. Adding more laser beams in the process, which is called Multi-laser Powder Bed Fusion (MLPBF), is considered to be the next generation of powder bed fusion technology.

There are two types of MLPBF technologies that have been developed: single trajectory lasers with multi-beam and multi-trajectory lasers with multi-beam [12]. In single trajectory lasers with multi-beam, a leading laser is followed by a pattern of a second one, all in the same trajectory or with minimum spatial offset. This technique uses the second laser beam as an auxiliary heat source and it has been found that it could heat up the region around the melt-pool and decrease the cooling speed [13]. Furthermore, each laser beam may be produced by an independent source or by diffraction of a single beam source. On the other hand, in multi-trajectory with multi-beam, each laser beam follows independent trajectories and all laser beams act as powder melting heat sources. It has been found that this configuration is more relevant as it improves the productivity rate due to processing in different zones [13].

The advantages of MLPBF is being able to improve the productivity of PBF processes and create bigger parts because the build chambers are larger. Additionally, MLPBF gives the possibility of obtaining more control on the microstructure of the part because of the possibility of using different laser beams, scanning vectors, scanning sequences and process parameters. However, when adding multiple lasers in LPBF processes, the thermal history that the components present is still really complex due to the repeated melting and solidification process. Additionally, the final residual stresses and deformations present on the final part are also dependent on the scanning strategy used during the manufacturing, as well as other process parameters such as the laser power and the powder bed temperature.

Therefore, being able to accurately and efficiently model the thermal history of parts created by single and mutli-laser PBF and determine the optimum scanning strategy to reduce the defects of the final part is a great challenge. In the last years, it has become an interest among researches and an important research focus.

1.3. Modelling of PBF processes

The modeling of powder bed fusion processes is challenging due to different reasons. Firstly, the process involves complex interaction of multiple physical phenomena such as interactions between the laser beam and the powder bed, heat transfer, fluid dynamics and solid mechanics, among others. Secondly, the geometry of the part needs to be accounted for, which introduces a mismatch of length scales. This mismatch of length scales is between the radius of the laser beam, which is usually in the range of micrometers (μm), and the dimension of the part, which is in the range of centimeters (cm).

Due to the different length scales present in LPBF processes, there are three divisions: micro-, meso-, and macro- (part) scales [14]. This categorization is widely used to model the different physical interactions that occur in LPBF processes. At the lowest level, the micro-scale, atomic diffusion occurs when the heat source interacts with the powder particles. Powder deposition, powder flow and laser heating of the powder bed occur at the meso-scale, which is in the range of $\sim$100 μm [15]. The macro-scale accounts for the dimension of the part, as well as the thermal stresses and distortion that the component suffers in LPBF processes.

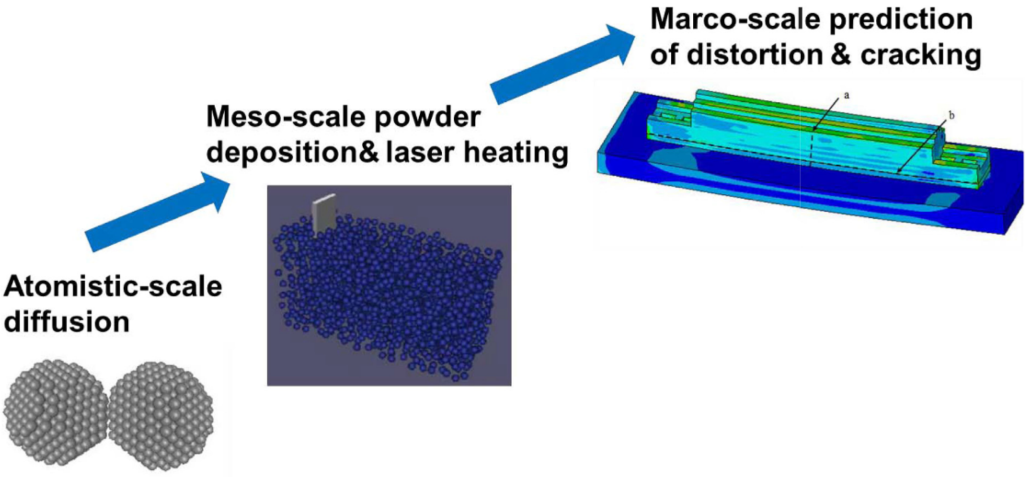

Figure 1.2: Schematic of the multi-scale physics present in laser powder bed fusion processes. Reproduced from [16].

Modelling the micro-scale accounts for the interactions between the heat source and the powder particles, which is fundamental to obtain the melt-pool and resulting thermal fields. Furthermore, different process parameters, such as the laser beam power and scan speed, have significant impacts on the melt-pool dynamics and spatter pattern, and result on the creation of pores and surface roughness of the part [15]. One important purpose of meso-scale modelling is the prediction of porosity and the cooling rates that dictate the microstructure and mechanical properties of the part [15].

On the component scale, one of the main issues when modelling PBF processes is that parts suffer from deformation and residual stresses due to steep temperature gradients. These temperature gradients occur at the vicinity of the laser spot and they are dependent on process parameters and the laser scanning strategy. In addition, the temperature history has a great impact on the microstructure, strength and surface quality of the part. Different thermal models have been proposed on literature to account for these residual stresses and thermal fields. Numerical models have been developed to predict the thermal history of parts based on the finite element method (FEM) and finite difference method (FD). However, most of these numerical models are computationally expensive. This is due to the mismatch of length scales mentioned before, that is being able to solve numerically these steep temperature gradients in the component scale requires a fine spatial and temporal discretization, which result in very high computational efforts [15].

To overcome these challenges, many researchers have developed different methods to optimize the scanning pattern and proposed thermal models to study the thermal history of parts built by single laser PBF and multi-laser PBF.

1.3.1. Scanning strategy

The scanning strategy is the geometrical pattern followed by the laser beam and it has a great effect on the temperature gradients of the part. By adjusting the scanning strategy in single and multi-laser PBF processes, many defects, such as large residual stresses and deformations, can be controlled.

The scanning strategies presented in literature have different scanning directions, scanning sequence, scanning vector rotation angle, scanning vector length, scanning time and hatch space. Figure 1.3 shows the most common scanning strategies used in single LPBF processes at the moment. It can be seen that some have longer scan vectors, while others divide the part in small units to obtain a shorter scan length.

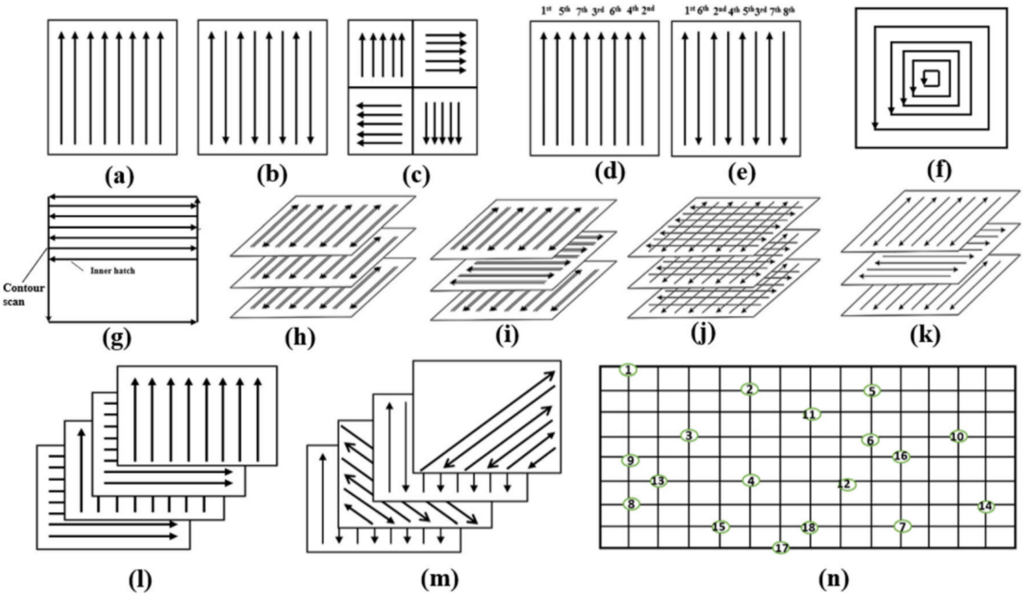

Figure 1.3: Most common scanning strategies presented in literature: a) Unidirectional scan. b) Bi-directional or zigzag scan. c) Island division scan. d) Variation of scanning sequences based on unidirectional scan. e) Variation of scanning sequences based on bi-directional scan. f) Helix scan. g) Contour scan. h) Bi-directional, double pass of laser beam. i) Bi-directional, double pass of laser beam with 90º rotation scan vector between layers. j) Cross scan. k) Bi-directional, single pass laser beam, 90º rotation scan vector between layers. l) Unidirectional with 90º rotation scan vector between layers. m) 45º rotation of scan vector. n) Point melting scan. Reproduced from [17].

An important difference between these scanning patterns is the severity of re-melting which affects the cooling rate and the re-melting after the formation of each layer generally improves the densification, reduces the surface roughness and defects. It has been found that when using long scanning vectors, excessive and accumulated stress is created and this has a negative impact on the part quality. Therefore, a proposal has been to use shorter length scan vectors in an island division scheme as an alternative method to create larger parts with improved quality (Figure 1.3 (c) shows an example of island division scheme) [17].

Many of the scan strategies presented in Figure 1.3 have been adapted to MLPBF processes. As mentioned in Section 1.2.1, there are two types of MLPBF techniques, single-trajectory with multi-beam and multi-trajectory with multi-beam. Most of the researchers, when presenting their optimum MLPBF scan strategy, use multi-trajectory with multi-beam, as this technique is more relevant because it improves the productivity rate.

Zhang *et al.* in [12] developed different simulations to optimize the best scanning strategy for MLPBF and investigated the effect of the scanning strategies on temperature, residual stresses, and the build direction. As shown in Figure 1.4, they developed twelve scanning strategies using single laser, dual laser, four laser, and thirty laser beams to determine which of the scanning strategies presented lower residual stresses, lower peak temperature and lower deflections in the final part. They showed that, for multiple laser beams, the part is manufactured faster and there is less time for the heat to be dispersed compared to single laser PBF. As shown in Figure 1.5, the laser exposure of multiple lasers is lower than when using a single beam, but the peak temperature increases with the number of lasers. This increase is because there is more heat input at any given time and less time for the energy to be dissipated through convection, conduction or radiation. Nonetheless, this decreases the temperature gradient and the cooling rates is slower, which reduces the deflection and residual stresses of the final part. Figure 1.6 shows that when using thirty lasers the part presents a lower value of residual stresses compared to the part created by single laser PBF.

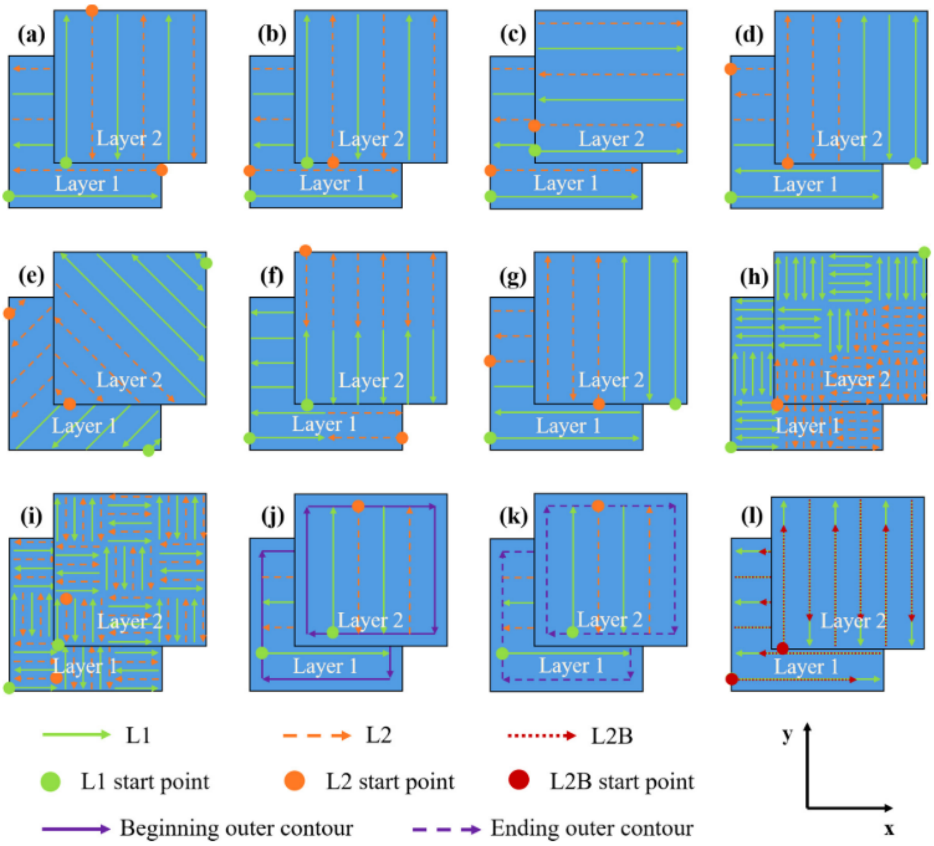

Figure 1.4: Twelve different scanning strategies developed in [12] for dual lasers. The green arrow represents the first laser to act on the part and the orange dotted arrow is the second laser beam. It can be seen that each laser beam follows independent patterns.

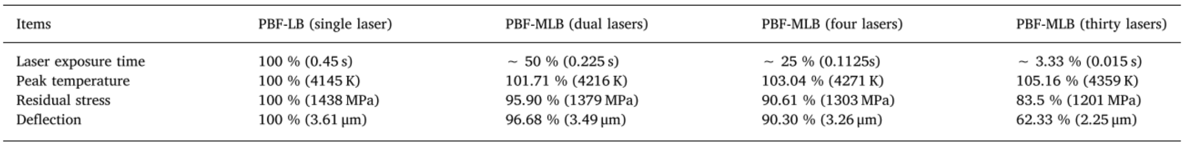

Items	PBF-LB (single laser)	PBF-MLB (dual lasers)	PBF-MLB (four lasers)	PBF-MLB (thirty lasers)
Laser exposure time	100 % (0.45 s)	~ 50 % (0.225 s)	~ 25 % (0.1125s)	~ 3.33 % (0.015 s)
Peak temperature	100 % (4145 K)	101.71 % (4216 K)	103.04 % (4271 K)	105.16 % (4359 K)
Residual stress	100 % (1438 MPa)	95.90 % (1379 MPa)	90.61 % (1303 MPa)	83.5 % (1201 MPa)
Deflection	100 % (3.61 µm)	96.68 % (3.49 µm)	90.30 % (3.26 µm)	62.33 % (2.25 µm)

Figure 1.5: Comparison table of the laser exposure time, the peak temperature, final residual stresses and deflection of a part created by single laser, dual laser, four lasers and thirty laser beams. Reproduced from [12].

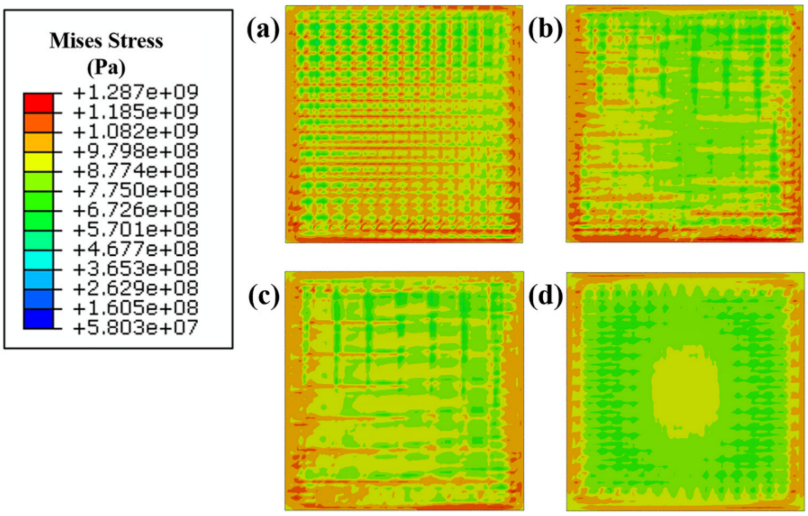

Figure 1.6: Final Von Mises residual stresses of a part created by: a) Single laser beam. b) Dual laser beams. c) Four laser beams. d) Thirty laser beams. Reproduced from [12].

Masoomi *et al.* in [18] simulated laser powder bed fusion and multi-laser powder bed fusion processes of two layers of a parallelepiped to study the effect of the number of layers, island division scheme, laser sweep direction and the number of lasers on the local temperature gradients, melt pool temperatures and heat affected zones (HAZs). They developed simulations with different scanning strategies, using 1, 2 and 4 lasers, and the temperature response of each strategy was studied. They concluded that employing MLPBF reduces the temperature gradient by ~5% and that using multiple lasers decreases the time required to fabricate each layer by ~75%. Furthermore, they stated that obtaining an uniform residual stress distribution depends greatly on the island geometry, as well as the orientation of laser scan vectors between the adjacent islands.

Zou *et al.* in [19] presented a thermo-mechanical model to investigate the effect of scanning strategies for a single laser and multi-lasers on the residual stresses. The numerical simulation model was validated by experimental results, and 18 scanning strategies were simulated, using up to four laser beams, with different scan lengths, scanning directions, sweeping directions, division schemes and sequences, as shown in Figure 1.7. Furthermore, they studied the final residual stresses and the temperature distribution of the cross section of the part. Figure 1.8 shows the stress fields on the first layers of the scanning strategy 4 and 9, respectively (present in Figure 1.7). It can be seen that the value of the residual stress in (a) is lower, which uses four different lasers and an island division scheme, that the one present in (b), which also has an island division scheme but in this case there is only two lasers. On the other hand, Figure 1.9 shows the cross sections of the melt pools of scanning strategies 1, 4 and 8, respectively. It can be seen that when using four lasers the melt-pool dimension is larger than when using a single laser. However, depending on the scanning strategy used for four lasers the melt-pool dimensions vary. Comparing the melt-pool dimension of (b) and (c) in Figure 1.9, it can be seen that using the island division scheme creates a smaller melt-pool than using the ”fourths” division scheme. They concluded that the scanning sequence has little effect on residual stress when using a single laser beam, but when using multiple lasers, the scanning sequence has an effect on residual stresses. Moreover, varying the sweep directions is beneficial for residual stresses to be evenly distributed in both longitudinal and transversal directions, when using multi-laser beams.

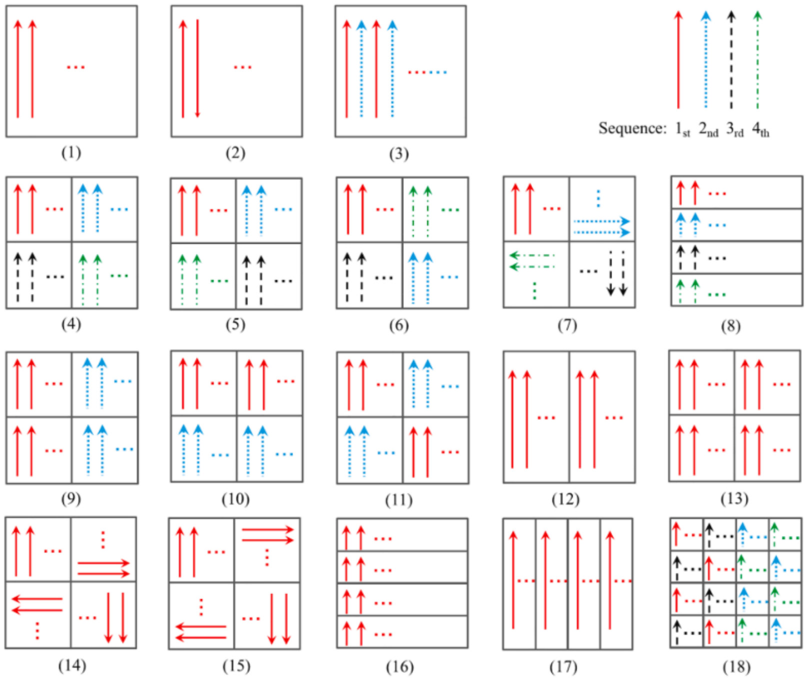

Figure 1.7: Schematic of the 18 scanning strategies simulated in [19]. Each colored arrow represents one laser beam: the first laser is the red arrow, the second is the blue one, the third is the green one and the fourth is the black one.

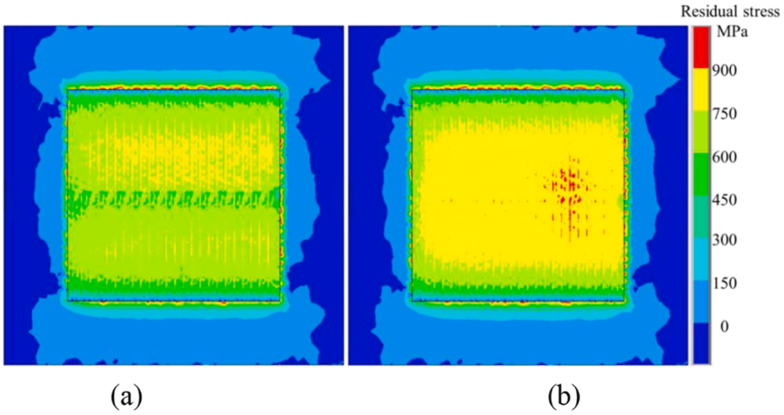

Figure 1.8: Residual stress distribution on the first layers of (a) scanning strategy 4 and (b) scanning strategy 9 (from Figure 1.7). Reproduced from [19].

As it can be seen, the scan pattern and scan strategy has a great influence on the residual stresses and thermo-mechanical properties of parts created by single and multi laser powder bed fusion. It has been found that employing an island division scheme with different sweep directions in MLPBF processes creates a smaller melt-pool dimension, which reduces the final residual stresses of parts. This is because the island division scheme doesn't require long scanning vectors, which create excessive and accumulated stress on the part. Moreover, even though applying more than one laser increases the build rate, the residual stresses of the final parts are reduced due to having slower cooling rates.

1.3.2. Thermal history

The influence of the scanning strategy on the temperature gradients, and consequently, on the formation of residual stresses and deformations, was shown in the previous section. In addition to determining

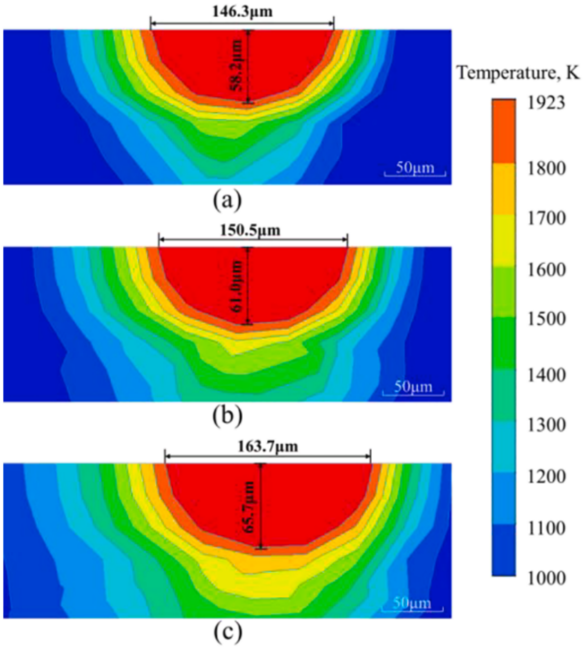

Figure 1.9: Temperature distribution of the cross section of (a) scanning strategy 1, (b) scanning strategy 4 and (c) scanning strategy 8 (from Figure 1.7). Reproduced from [19].

the scanning strategy, being able to accurately represent the temperature distribution on parts created by LPBF processes is an important factor to predict the deformation and residual stresses that arise due to thermal strains.

To study the thermal history of parts created by powder bed fusion processes, researchers have proposed in the available literature thermal models based on numerical and analytical solutions.

Numerical models are based on the finite element method (FEM) and finite difference method (FD). These methods discretise the part studied in a mesh with triangular or rectangular elements in 2D and tetrahedral or hexahedral elements in 3D, among others. The computational time required to model an entire component is extremely high due to the large number of finite elements necessary to model a part of complex geometry, as well as the scan tracks and the additive layers [15]. When using a purely numerical model to obtain the temperature distribution in a part, the quality of the mesh is really important because it has a great influence on the convergence of the numerical computation, the accuracy of computation results and the computational efficiency. This is because using a mesh size that is not fine enough will not provide the correct results. There are mainly two mesh schemes that researchers use to model the additive layers: the uniform mesh and the non-uniform mesh. Most of the researchers use a non-uniform mesh scheme. The non-uniform mesh consists on maintaining a mesh refinement around a region of interest while having a coarser mesh elsewhere. Depending if the mesh is updated during the simulation, this mesh scheme can be further divided in a static and dynamic mesh scheme. When using the dynamic mesh scheme, the density of the mesh can change depending on the value of the thermal gradients. Furthermore, the dynamic mesh scheme allows for the mesh to be refined and coarsened as the heat source moves. On the other hand, the static mesh scheme is constant in the region of interest [20].

However, these techniques have some disadvantages. The static mesh scheme is not suitable to model multi-layers and, as mentioned before, the mesh does not change with the melt-pool. For the case of the dynamic mesh scheme, it has a low computational cost, high accuracy and is suitable for modelling multi-layers. However, it is really difficult to implement and there are only a few available commercial softwares that can model moving meshes. In addition, in these models the temperature data has to be mapped between different meshes, which also introduces more computational effort [20].

Cheng *et al.* in [21] developed a 3D finite element model to study numerically the temperature, stress and deformation of parts created by SLM under eight different scanning strategies. The thermo-mechanical analysis was developed in ABAQUS in a domain of 8 x 8 x 1 mm. They employed a finer mesh in the scanning region, while the mesh size gradually increased with the distance away from the main domain. Overall, the model had 20800 elements and the element dimensions in the scanning domain was 0.2 x 0.2 x 0.015 mm. The thermal simulation that they developed took about 72 h, while the mechanical analysis was about 20 h.

Masoomi *et al.* in [22] estimated the temperature field of the substrate, powder bed, solidified part and melt pool by employing finite differences. For the simulations, they employed a tetrahedral mesh scheme with uniform grid spacing with respect to the Z-direction. As shown in Figure 1.10, a finer spatial mesh was employed for all the layers of the power bed. This finer mesh consisted of cells with approximately 33% of the laser diameter and a volume of approximately 230,000 μm^3. On the other hand, a coarser mesh was used on the substrate that consisted of cells with 200% larger volumes.

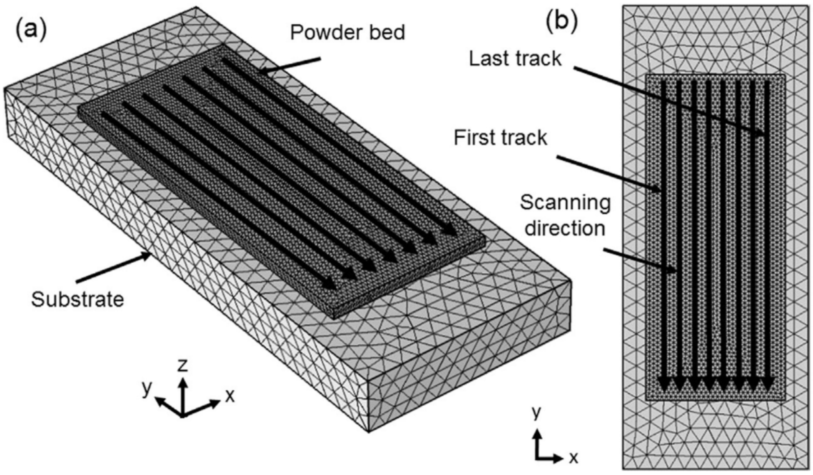

Figure 1.10: Schematic of the meshing scheme developed in the simulations on [22]. They used a mesh refinement on the part while a coarser mesh was used on the base plate.

On a similar approach, Zhang *et al.* in [12], used a mesh size of 20 μm x 20 μm x 20 μm on the part while the base plate was modelled with a coarser mesh of 0.2 mm x 0.2 mm x 0.2 mm. The total number of elements necessary to model the part was of 139,500.

On the other hand, analytical models have been found to be extremely fast and obtain quick solutions, which can be used at the component scale. These models have been used to predict the thermal history of a moving laser with a high computational performance, due to not requiring extensive calculations compared to numerical solutions. However, the disadvantages of these models are that it cannot consider temperature-dependent thermal properties and they are not able to incorporate realistic boundary conditions [15]. Analytical models are based on the solution of the heat equation in semi-infinite space, and modelling parts with a bounded domain analytically underestimates temperatures near the boundaries, as well as not being able to properly incorporate the boundary conditions.

To avoid the problems introduced when using an analytical model, in the Precision and Microsystems Engineering (PME) Department at TU Delft, proposed a semi-analytical model to study the thermal history of parts created by SLM. The semi-analytical approach is a combination of an analytical solution and numerical solution, with the use of the method of images and the superposition principle.

Yang *et al.* in [6] presented a method to investigate how temperature transients affect residual stresses and deformations in parts created by selective laser melting (SLM). As mentioned before, there is a mismatch of length scales between the spot radius of the laser beam and the dimension of the part. This issue makes it really difficult to solve the governing heat equation numerically, for example using finite elements. To overcome this problem, Yang *et al.* introduces a semi-analytical approach and utilizes the superposition principle to accurately describe the temperature distribution in the part, taking into account all the boundary conditions.

In the model, a body V is submerged into the powder bed where is attached to the base plate and the scanning vector is discretized by a finite number of point heat sources. The superposition principle is based on the combination of an analytical solution that captures high spatial gradients, and a numerical solution that ensures compliance with boundary conditions. The temperature field is decomposed in $\tilde{T}$, which is the temperature field of a line discretized in N point heat sources in a semi-infinite space, and $\hat{T}$, which is the temperature field due to the dimension of the powder bed and the boundary conditions, as shown in Figure 1.11. However, when there are point sources within a critical distance from the boundary a finer discretization is required for the numerical solution to capture the steep temperature gradients at the boundary. This makes the solution of $\hat{T}$ computationally complex. For this reason, the use of the method of images is introduced to analytically enforce the boundary conditions for those points located at a critical distance from the boundary.

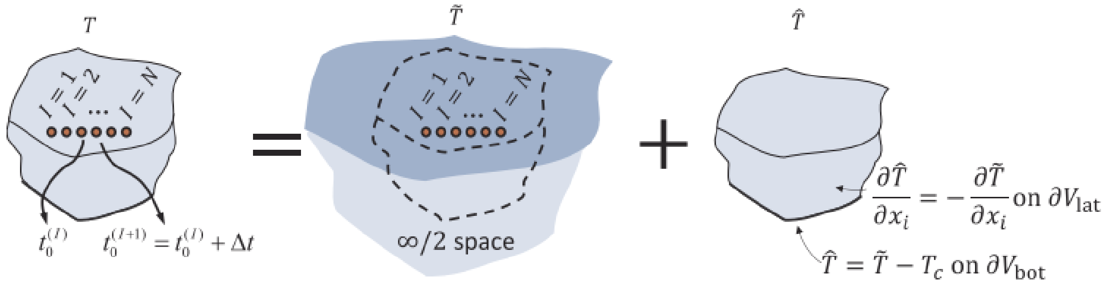

Figure 1.11: Decomposition of the temperature field into $\tilde{T}$, which accounts for N point heat sources, and $\hat{T}$, without the heat sources and accounts for the boundary conditions. Reproduced from [6].

The principle of the method of images is mirroring the original source with respect to the boundary. Figure 1.12 shows a regular source in red, I, and its image sources $J = 1$ and $J = 2$ in blue with respect to the boundaries $\partial B^{(1)}$ and $\partial B^{(2)}$, respectively. If the energy associated with image source $J = 1$ is taken as Q and is identical to the energy of the regular source I, the heat flux at boundary $\partial B^{(1)}$ due to the original source and image source $J = 1$ is zero. Moreover, if the energy associated to image source $J = 1$ is taken as $-Q$, the temperature at boundary $\partial B^{(1)}$ due to the image source $J = 1$ and the regular source I is zero. This is the same for the image source $J = 2$ at boundary $\partial B^{(2)}$.

It can be observed that the existence of image source $J = 2$ has an influence on boundary $\partial B^{(1)}$ and a second order image source is needed to represent this. In this case, image source $J = 3$ is introduced as the mirror image of image source $J = 2$ with respect to boundary $\partial B^{(1)}$. The same happens with image source $J = 1$ with respect to boundary $\partial B^{(2)}$, and image source $J = 4$ is introduced in the same way. This continues on, and an infinite number and order of image sources is necessary to model this. As the order of reflection increases, the distance between the boundary and the image sources also increases. However, the temperature field due to higher order image sources will be smooth at the boundary and it can be accounted in the numerical solution of $\hat{T}$. This means that a limited number of image sources is introduced only when the distance between the regular or image sources and the boundary is less than a critical distance, denoted as H_c.

One important thing to note is that the use of image sources can only be applied when the body V is a convex polyhedron. In Figure 1.13, the boundaries are separated by an angle of 90° (they are orthogonal to each other), which gives a convex corner. When using the method of images in this type of geometry, only a second order image source $J = 3$ is sufficient to properly model it. It can be seen that image source $J = 1$ is the mirror image source created for the point source I with respect to boundary 1, and $J = 2$ is the image source with respect to boundary 2. In addition, $J = 3$ is needed to consider the effect of image source $J = 2$ with respect to boundary 1. Because of symmetry, image

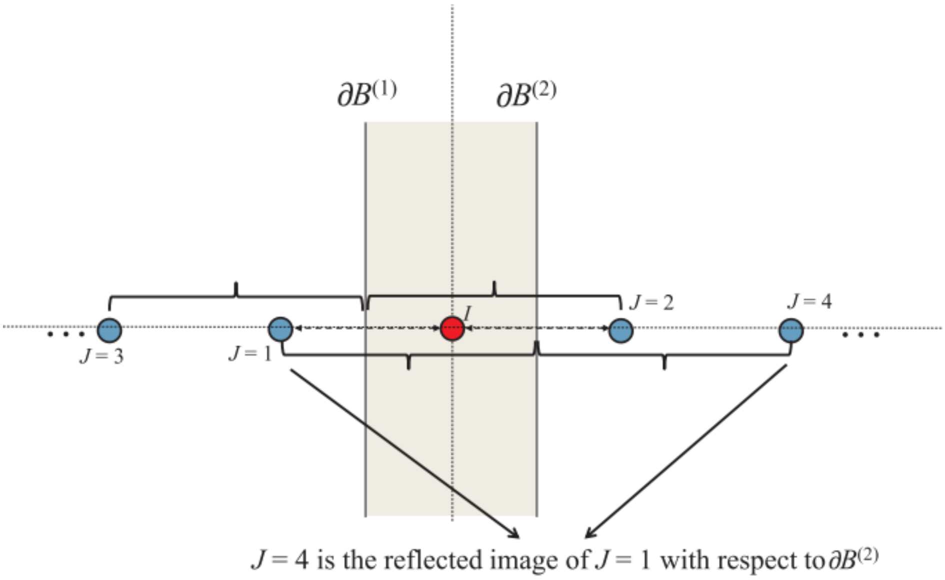

Figure 1.12: Schematic representation of the method of images in 2D. Image sources are shown in blue, while the original source is the red point, and they are taken with respect to boundary $\partial B^{(1)}$ and $\partial B^{(2)}$. J = 1 and J = 2 are the first order image sources with respect to boundary $\partial B^{(1)}$ and $\partial B^{(2)}$, respectively; while, J = 3 and J = 4 are the second order of image sources. Reproduced from [6].

source $J = 4$, which is necessary to model the effect of image source $J = 1$ with respect to boundary 2, lies in the same position as image source $J = 3$.

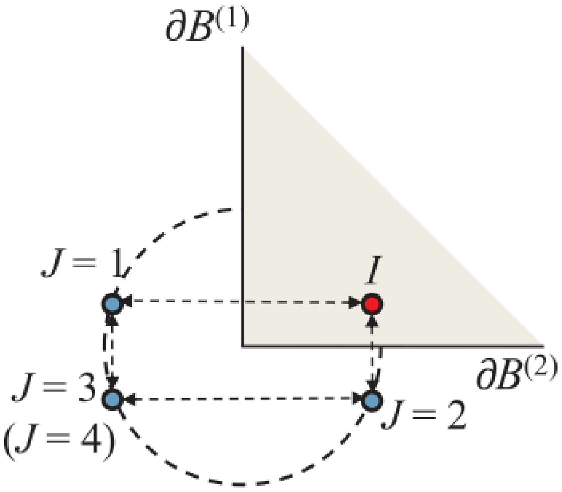

Figure 1.13: Schematic of the method of images in a 2D example where the boundaries $\partial B^{(1)}$ and $\partial B^{(2)}$ are orthogonal to each other. In this case, only a second order image source J = 3 is sufficient to model this. Reproduced from [6].

However, when the boundaries are separated by an angle greater than 180º, a concave corner is created. In Figure 1.14 it can be seen that image source $J = 1$ is the mirror image source of point source I with respect to boundary $\partial B^{(1)}$, and it creates an erroneous heat flux in boundary $\partial B^{(2)}$, represented by the orange arrow. This will create high temperature gradients in boundary $\partial B^{(2)}$ and the boundary conditions mentioned before will not be satisfied. For this reason, it is not suitable to apply the method of images to solve boundary value problems in non-convex domains.

To be able to model a concave polyhedron, Yang *et al.* presented in [23] a semi-analytical approach

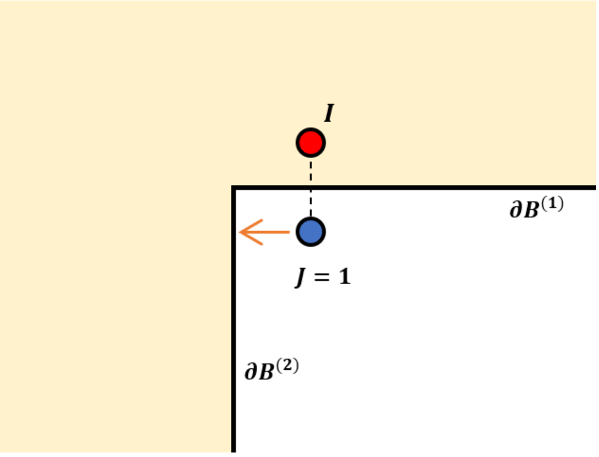

Figure 1.14: Schematic of a concave corner, where the mirror source $J = 1$ creates an erroneous heat flux with respect to boundary $\partial B^{(2)}$, indicated by the orange arrow.

without the use of image sources. In this model, they also used a body V submerged into the powder bed and attached to the base plate. In this case, the laser scanning vector is described as a line source instead of an array of point heat sources. The superposition principle is also utilised to describe the temperature field of the part, combining an analytical solution and a numerical solution. The temperature field is decomposed in $\tilde{T}$, that accounts for the total contribution of all the line sources solutions, and $\hat{T}$, that accounts for all the boundary conditions. In this case, the same happens as described before, when the laser scanning vectors approach the lateral boundary, $\hat{T}$ is less smooth and a finer discretization is necessary to obtain a solution. As mentioned, in this model, image sources are not introduced as the body V has concave surfaces. To be able to solve for the points close to the lateral boundary, a mesh refinement is employed so that $\hat{T}$ can be solved numerically by a finite element analysis, as shown in Figure 1.15.

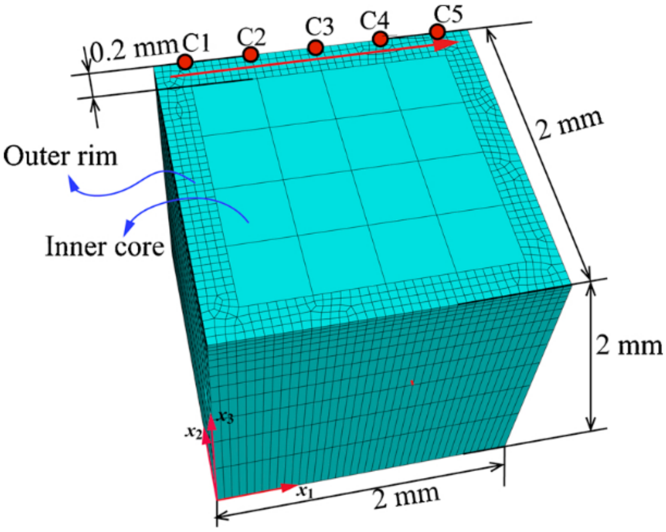

Figure 1.15: Finite element mesh developed in a cubic part. The mesh refinement is developed in the lateral boundary, while a coarser mesh is kept on the rest of the part. The laser scanning vector is represented as the red arrow. Reproduced from [23].

Nevertheless, the semi-analytical approach presented in [23] is not the ideal solution to model the thermal history of a part created by SLM. Even though, it is more computationally efficient than other models, it still employs a great computational effort due to the great number of elements needed to implement the mesh refinement close to the boundary, as shown in Figure 1.16.

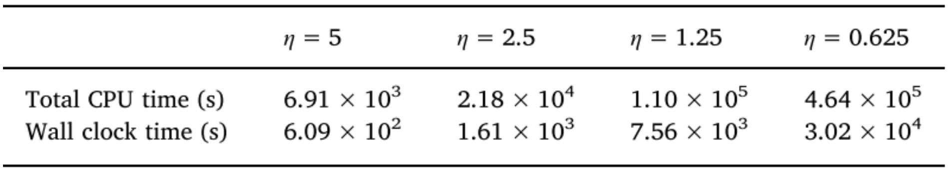

	$\eta = 5$	$\eta = 2.5$	$\eta = 1.25$	$\eta = 0.625$
Total CPU time (s)	6.91×10^3	2.18×10^4	1.10×10^5	4.64×10^5
Wall clock time (s)	6.09×10^2	1.61×10^3	7.56×10^3	3.02×10^4

Figure 1.16: Computational time necessary to model a simple cubic part as a function of mesh density (η). It can be seen that as a finer mesh is implemented, the computational time is increased. Reproduced from [23].

With a different approach, to be able to model a non-convex polyhedron with the method of images, Steuben *et al.* in [24] developed an enriched analytical solution method to obtain the temperature distribution of non-convex parts created by AM. The domain of the model has a curved concave boundary, as shown in Figure 1.17, in which the method of images model is used to impose the boundary conditions for points located at a critical distance to the curve boundary. To use correctly the method of images in a concave boundary, two correction factors are introduced to calculate the analytical temperature distribution of the mirror images. The correction factors account for the boundary curvature and to ”model potential ”clipping” of distributed heat sources located near the boundary” [24]. Then, by the use of the superposition principle, the temperature distribution is obtained analytically. The results of the enriched analytical model were compared to existing finite element analysis (FEA) methods and the relative error between the models were in the range of 2-3%.

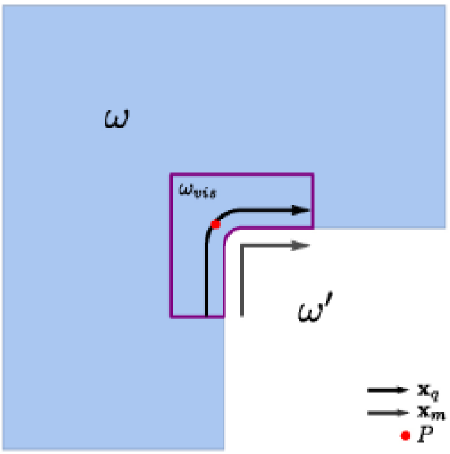

Figure 1.17: Schematic in 2D of the finite non-convex domain studied in [24], in which ω is the 2D AM part domain, ω' is the complement of ω, x_q is the heat source path and x_m is the mirror source path. Reproduced from [24].

However, even though the model is able to accurately imposed the boundary condition in the concave boundary, it does not correctly impose the corresponding boundary conditions on the other boundaries of the domain.

As it can be seen, there are different methods to model the thermal history of parts created by AM. Numerical methods have been proposed to model the temperature distribution by applying the finite element and finite difference method, in which non-uniform mesh schemes have been created to model the heat source with a finer mesh while keeping the rest of the domain with a coarser mesh. However, the computational effort of these numerical solutions is really large as being able to model components of complex geometry require a large number of finite elements. To reduce the computational effort of the numerical models, semi-analytical methods have been found effective to model the thermal history of parts as the models combine an analytical solution with a numerical solution.

1.4. Motivation

As mentioned previously, being able to accurately model the thermal history of a part created by laser powder bed fusion processes, as well as obtain an optimum scanning strategy, is challenging.

Researchers have been able to determine different scanning strategies by changing the scan sweep direction, scan vector length, scan sequence and division schemes, and investigate the effect of them on the temperature gradients, final residual stresses and deformations of the final part. It has been found that employing multiple lasers in powder bed fusion processes reduces the manufacturing time of parts compared to single laser PBF processes, as well as reducing the deflection and residual stresses of the final part. This is due to having less time for heat to be dispersed and energy to be dissipated by convection, conduction and radiation, which reduces the temperature gradients and the cooling rate is slower. In addition, the island division scheme with different sweep directions is an optimum scanning strategy in multi-laser powder bed fusion processes that creates smaller melt-pool dimensions, which reduces the final residual stresses of parts.

On the other hand, different numerical models have been proposed to obtain the thermal history of the part by applying finite element and finite difference schemes. Moreover, non-uniform mesh schemes have been created to be able to reduce the computational effort of these models by performing mesh refinements on the region of interest. However, even with these improvements, the computational effort necessary to model LPBF and MLPBF processes is still really high.

To be able to overcome this, semi-analytical methods have been found to be effective to study the thermal history of parts created by LPBF processes by combining an analytical solution and a numerical solution. As mentioned in Section 1.3, Yang *et al.* in [6] were able to create a thermal model using the semi-analytical approach, as well as the use of the superposition principle and the method of images. However, their main issue was that the model could only be applied to convex polyhedron. On the other hand, Steuben *et al.* in [24] proposed an enriched analytical model in which the method of images was used to obtain the temperature distribution of a non-convex domain. However, the model does not take into account the full boundary value problem, as it only imposes analytically the boundary condition on the concave boundary and the other boundaries are not included in the formulation.

The goal of this project is to obtain a thermal model for laser powder bed fusion processes using the semi-analytical approach, the superposition principle and the method of images for any arbitrary shape. More specifically, a non-convex geometry will be studied and a thermal model based on the semi-analytical model will be proposed, in which a modification to the method of images will be done. This modification will allow to use the method of images in non-convex geometries, while satisfying the boundary conditions in the whole domain.

1.5. Outline of the report

The remainder of the report is divided in four chapters. Chapter 2 presents the formulation of the thermal problem studied. In this chapter, the semi-analytical model is explained in detail, which is based on the superposition principle and the method of images. Furthermore, the corrections used to model non-convex geometries are presented. In Chapter 3 the numerical tools used to obtain the numerical correction field are presented. In Chapter 4 different numerical examples are shown to illustrate the potential and possible limitations of the approach developed. Finally, Chapter 5 gathers the conclusions drawn from the study and recommendations for future work.

2

Formulation

In this chapter the thermal problem studied in this thesis is presented. The thermal formulation to solve the problem is based on [6], in which the superposition principle and the method of images are used.

2.1. Thermal problem

Consider the three-dimensional non-convex body V shown in Figure 2.1 is manufactured by laser powder bed fusion. It is assumed that at time t, the body V and its surface ∂V has already been built and is submerged into the powder bed, where a layer of powder is laid on top of the body. The lateral surface ∂V_{lat} and the top surface ∂V_{top} are covered with powder, while the bottom surface ∂V_{bot} is attached to the base plate. At time t, a laser beam starts scanning the top surface of the powder bed with a predefined scanning pattern and energy is transferred into the body by conduction. Then, the temperature of the body increases following the heat equation

$$\rho c_p \frac{\partial T}{\partial t} = \boldsymbol{\nabla} \cdot (k \boldsymbol{\nabla} T) + Q \quad \text{in } V, \tag{2.1}$$

where T is the temperature, ρ is the density, c_p is the constant-pressure specific heat, k is the thermal conductivity, Q is the rate of volumetric heat generation, and t is time. The thermal parameters of the material, k, ρ, and c_p, are a function of temperature, which means that their values depend on the temperature (and therefore on the spatial coordinates).

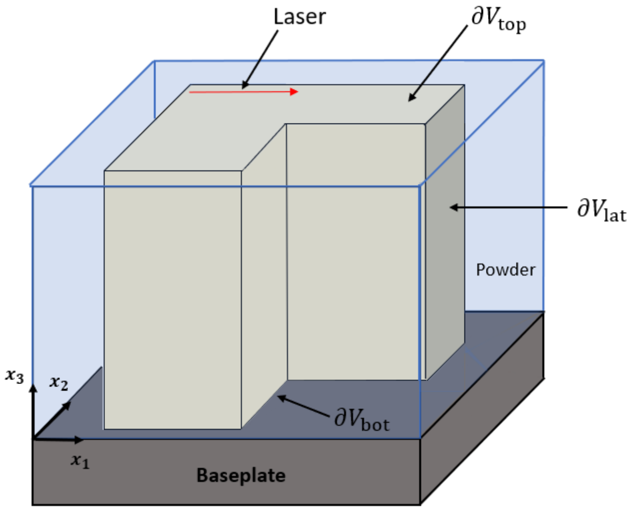

Figure 2.1: Schematic of the three-dimensional non-convex body V used in this thermal model and its surface ∂V, decomposed in ∂V_{top}, ∂V_{lat} and ∂V_{bot}. The body V is submerged into the powder bed and attached to the base plate.

To define a proper boundary problem, the following boundary conditions are determined on ∂V, where $\partial V = \partial V_{\mathrm{top}} \cup \partial V_{\mathrm{lat}} \cup \partial V_{\mathrm{bot}}$. The conductivity of the powder covering $\partial V_{\mathrm{lat}}$ and $\partial V_{\mathrm{top}}$ is approximately 100 times smaller than that of the material of body V [6], hence the powder has negligible conductivity and it can be assumed that the powder is insulating. Moreover, the powder at $\partial V_{\mathrm{top}}$ is melted by the laser, which enables energy transfer through radiation and convection. However, the heat transferred within the body occurs mainly by conduction and in comparison the heat lost by radiation and convection is negligible. Thus, the energy lost by radiation and convection is not included in the formulation. Therefore, a zero heat flux condition is imposed in $\partial V_{\mathrm{lat}}$ and $\partial V_{\mathrm{top}}$. Furthermore, during PBF processes the base plate is maintained at a constant temperature. Taking this into account, a prescribed temperature boundary condition is imposed on the bottom surface $\partial V_{\mathrm{bot}}$ that is bonded to the base plate.

The resulting boundary conditions are the following

$$\frac{\partial T}{\partial \mathbf{x}} \cdot \mathbf{n} = 0 \quad \text{on } \partial V_{\mathrm{lat}}, \tag{2.2}$$

$$\frac{\partial T}{\partial \mathbf{x}} \cdot \mathbf{m} = 0 \quad \text{on } \partial V_{\mathrm{top}}, \tag{2.3}$$

$$T = T_c \quad \text{on } \partial V_{\mathrm{bot}}, \tag{2.4}$$

where **n** and **m** are the outward facing normal vectors in $\partial V_{\mathrm{lat}}$ and $\partial V_{\mathrm{top}}$, respectively, and T_c is the known temperature in the base plate. Following the coordinate system of Figure 2.1, it can be noted that the outward facing normal vector of the top surface $\partial V_{\mathrm{top}}$ is $\mathbf{m} = [0, 0, 1]$, while the normal vectors of the lateral surfaces vary (although the component n_3 of **n** is always 0).

As mentioned in Section 1.3, solving numerically this thermal problem is computationally expensive due to the dimensions of the domain. To be able to capture numerically the steep temperature gradients that arise in the vicinity of the laser spot, a fine spatial discretization of the order of the laser spot size is required. Since the laser scans everywhere in the part, the fine discretization is required in the whole domain. However, due to the large dimensions of the domain, modelling the body V at the scale of the laser spot size requires a great computational effort because of the high number of elements necessary to model it. As explained before, there is a mismatch of length scales between the radius of the laser spot r, which is usually in the range of 10-15 μm, and the dimension of the body, which is on the order of 10-100 mm.

To be able to reduce the computational time and make the solution tractable, the semi-analytical model proposed in [6], which is based on the superposition principle and the method of images, will be used.

2.2. Semi-analytical model

The semi-analytical method in [6] proposes to use the combination of an analytical solution, which captures the high spatial gradients of the laser beam by using the analytical temperature solution of point sources in semi-infinite space, and a numerical solution that ensures that the boundary conditions are satisfied in the domain.

Firstly, the temperature dependence of the thermal parameters k, ρ, and c_p is neglected, that is their values are assumed to be constant with temperature. For many materials, the variation of the values of these thermal parameters with temperature is not as large in a specific temperature interval [25]. Then, it is common practice to assume an average value for these parameters and treat it as constant [6, 25]. Moreover, assuming the thermal parameters have a constant value with temperature, makes Equation 2.1 linear, which is necessary for the superposition principle to be applied. It allows for the thermal conductivity to be taken out of the derivative in Equation 2.1, which results in the following equation

$$\frac{\partial T}{\partial t} = \alpha \boldsymbol{\nabla}^2 T + \frac{Q}{\rho c_p} \quad \text{in } V, \tag{2.5}$$

where α is the thermal diffusivity, defined as $\alpha = k/\rho c_p$.

As shown in Figure 2.2, the laser scanning vector is represented by a finite number of point heat sources indexed by I, where $I = 1, ..., N$. Point I is created at time $t_0^{(I)}$, while source $I+1$ is created at time $t_0^{(I+1)} = t_0^{(I)} + \Delta t$, where Δt is the time step for the time integration. The predefined scanning pattern determines the location of each point heat source. Moreover, each heat source is separated by the neighbouring heat sources by $v\Delta t$, where v is the speed of the laser beam.

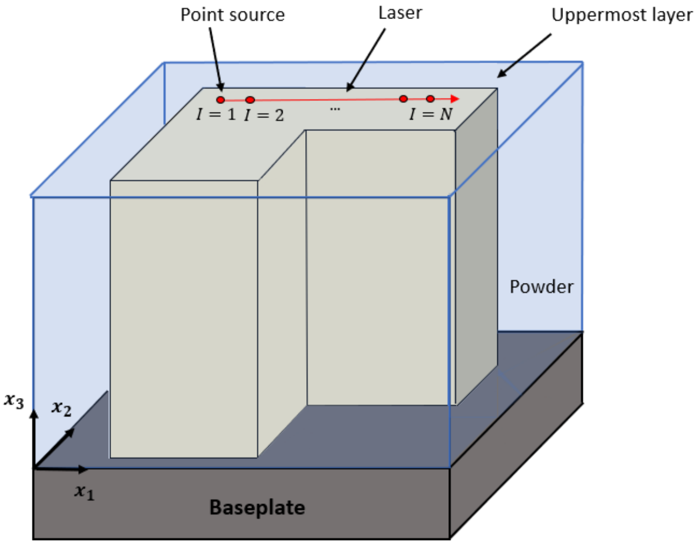

Figure 2.2: Schematic of the body V submerged in the powder bed where ∂V_{bot} is attached to the base plate and the laser beam, which is applied in the uppermost layer, is discretised by point heat sources.

This model is then solved by applying the superposition principle, which decomposes the total temperature field T as

$$T = \tilde{T} + \hat{T}, \tag{2.6}$$

where $\tilde{T}$ is the temperature field due to N point heat sources in a semi-infinite space and $\hat{T}$ is the temperature field that accounts for the finite dimensions of the powder bed, as well as the boundary conditions described in Section 2.1.

To represent the temperature field of the N point sources, $\tilde{T}(x_1, x_2, x_3, t)$, that comprise the scanning vector, the temperature distribution of each point source is summed as

$$\tilde{T}(x_1, x_2, x_3, t) = \sum_{I=1}^{N} \tilde{T}^{(I)}(x_1, x_2, x_3, t). \tag{2.7}$$

The temperature field $\tilde{T}^{(I)}(x_1, x_2, x_3, t)$ of a point source I is determined analytically as

$$\tilde{T}^{(I)}(x_1, x_2, x_3, t) = \frac{Q^{(I)} A}{4\rho c_p (\pi\alpha(t - t_0^{(I)}))^{3/2}} exp\left(\frac{-(R^{(I)})^2}{4\alpha(t - t_0^{(I)})}\right), \tag{2.8}$$

where $Q^{(I)}$ is the energy associated to source I, A is the fraction of energy of the laser beam absorbed by the powder, and $R^{(I)}$ is the distance between the material point of interest (x_1, x_2, x_3) and the location of the point heat source $(x_1^{(I)}, x_2^{(I)}, x_3^{(I)})$, that is $(R^{(I)})^2 = (x_1 - x_1^{(I)})^2 + (x_2 - x_2^{(I)})^2 + (x_3 - x_3^{(I)})^2$. When the time step Δt is really small, $Q^{(I)}$ is defined as $Q^{(I)} = P\Delta t$, where P is the power of the laser beam in watts.

When $t \geq t_0^{(I)}$, Equation 2.8 is the analytical solution of the linear heat equation (Equation 2.5) for a point source I in a semi-infinite space. If $t < t_0^{(I)}$, then $\tilde{T}^{(I)}(x_1, x_2, x_3, t) = 0$. It can be noted that when the source is created at $t = t_0^{(I)}$, Equation 2.8 becomes singular. As a matter of fact, as t approaches $t_0^{(I)}$, $\tilde{T}^{(I)}(x_1, x_2, x_3, t)$ goes to infinity. To avoid this singularity, in [6], it is assumed that the laser heat source has a Gaussian distribution with a finite spot radius, r, and a time shift, $\tau_0^{(I)}$, is introduced in Equation 2.8 to represent this effect. This time shift allows for the point source I to diffuse a distance equal to the laser spot radius before $t = t_0^{(I)}$. Therefore, the temperature field $\tilde{T}^{(I)}(x_1, x_2, x_3, t)$ is given by

$$\tilde{T}^{(I)}(x_1, x_2, x_3, t) = \frac{Q^{(I)}A}{4\rho c_p(\pi\alpha(t - \tau_0^{(I)}))^{3/2}} exp\left(\frac{-(R^{(I)})^2}{4\alpha(t - \tau_0^{(I)})}\right), \tag{2.9}$$

where

$$\tau_0^{(I)} = t_0^{(I)} - \frac{r^2}{8\alpha}. \tag{2.10}$$

Observe that: $t - \tau_0^{(I)} = t - t_0^{(I)} + \frac{r^2}{8\alpha}$. The term $\frac{r^2}{8\alpha}$ eliminates the singularity of Equation 2.9 as t approaches $t_0^{(I)}$.

On the other hand, as mentioned before, from Equation 2.6, $\hat{T}$ is the temperature field that accounts for the finite dimensions of the powder bed, as well as the boundary conditions. This field is governed by the following equation

$$\frac{\partial \hat{T}}{\partial t} = \alpha \boldsymbol{\nabla}^2 \hat{T} \quad \text{in } V, \tag{2.11}$$

with boundary conditions

$$\hat{T} = T_c - \tilde{T} \quad \text{in } \partial V_{\text{bot}}, \tag{2.12}$$

$$\frac{\partial \hat{T}}{\partial \mathbf{x}} \cdot \mathbf{n} = -\frac{\partial \tilde{T}}{\partial \mathbf{x}} \cdot \mathbf{n} \quad \text{on } \partial V_{\text{lat}}, \tag{2.13}$$

$$\frac{\partial \hat{T}}{\partial \mathbf{x}} \cdot \mathbf{m} = -\frac{\partial \tilde{T}}{\partial \mathbf{x}} \cdot \mathbf{m} \quad \text{on } \partial V_{\text{top}}, \tag{2.14}$$

where **n** and **m** are, as in Equations 2.2 and 2.3, the outward facing normal in ∂V_{lat} and ∂V_{top}, respectively, and T_c is the temperature of the base plate. It can be noted that the temperature gradients of $\tilde{T}$ in Equations 2.13 and 2.14, that is $\frac{\partial \tilde{T}}{\partial \mathbf{x}} \cdot \mathbf{n}$ and $\frac{\partial \tilde{T}}{\partial \mathbf{x}} \cdot \mathbf{m}$, are known as they can be obtained analytically from Equation 2.9. Moreover, it can be seen that, because the vector normal of ∂V_{top} is $\mathbf{m} = [0, 0, 1]$, the term $\frac{\partial \tilde{T}}{\partial \mathbf{x}} \cdot \mathbf{m}$ in Equation 2.14 can be written as

$$\frac{\partial \tilde{T}}{\partial \mathbf{x}} \cdot \mathbf{m} = \left[\frac{\partial \tilde{T}}{\partial x_1}, \frac{\partial \tilde{T}}{\partial x_2}, \frac{\partial \tilde{T}}{\partial x_3}\right] [0, 0, 1]^{\text{T}} = \frac{\partial \tilde{T}}{\partial x_3}, \tag{2.15}$$

where only the x_3 component of the temperature gradient of $\tilde{T}$ is needed. Then, calculating analytically $\frac{\partial \tilde{T}}{\partial x_3}$ from Equation 2.9 gives

$$\frac{\partial \tilde{T}}{\partial x_3} = \frac{Q^{(I)}A}{4\rho c_p(\pi\alpha(t - \tau_0^{(I)}))^{3/2}} exp\left(\frac{-(R^{(I)})^2}{4\alpha(t - \tau_0^{(I)})}\right)\left(-\frac{2(x_3 - x_3^{(I)})}{4\alpha(t - \tau_0^{(I)})}\right) = 0, \tag{2.16}$$

where it can be seen is equal to zero. This is because, as shown in Figure 2.2, in this case, the x_3-coordinate of the point heat sources has the same value as the x_3-coordinate of the material points of interest on ∂V_{top}. Thus, the temperature gradient in Equation 2.16 is equal to zero. This satisfies the boundary condition of no-heat flux on ∂V_{top}, which can be seen is already implicit on the solution of $\tilde{T}$. Then, the term $\frac{\partial \tilde{T}}{\partial \mathbf{x}} \cdot \mathbf{m}$ in Equation 2.14 is zero and Equation 2.14 can be rewritten as

$$\frac{\partial \hat{T}}{\partial \mathbf{x}} \cdot \mathbf{m} = 0 \quad \text{on } \partial V_{\text{top}}. \tag{2.17}$$

It is important to observe that, when $\tilde{T}$ and its gradients on the boundary $\partial V_{\text{lat}} \cup \partial V_{\text{bot}}$ are not too large, Equation 2.11 is smooth and can be solved by a standard numerical method such as finite differences. However, point sources created at a location close to the boundary $\partial V_{\text{lat}} \cup \partial V_{\text{bot}}$ produce very large gradients of $\tilde{T}$ in the region of the boundary near the point sources. In this situation, solving Equation 2.11 will require a discretization on the boundary of the order of the laser radius that makes the solution of Equation 2.11 computationally intractable. Therefore, to be able to correctly enforce the boundary conditions for the point sources located within a critical distance from the boundary $\partial V_{\text{lat}} \cup \partial V_{\text{bot}}$, a correction to the temperature field $\tilde{T}$ is introduced with the method of images creating the analytical temperature field $\check{T}$. The temperature gradients of the analytical solution $\tilde{T} + \check{T}$ will not be too large at the boundary $\partial V_{\text{lat}} \cup \partial V_{\text{bot}}$ and it will allow to solve Equation 2.11 with a numerical method with a coarse dicretization and step sizes.

The total temperature field is then modified to

$$T = \tilde{T} + \hat{T} + \check{T}. \tag{2.18}$$

2.3. Method of images

As explained in Section 1.3.2, the idea of the method of images is mirroring the point sources, I, with respect to the boundaries located at a critical distance H_c, and creating image sources, J. To find the location of the image sources, first, it is determined which boundaries are located at a distance smaller than H_c from the point heat sources. Then, the image sources are reflected symmetrically with respect to these boundaries. Figure 2.3a shows a point heat source, I, located close to boundary $\partial B^{(1)}$. To visually demonstrate the distance between the point heat source and the boundaries, the point source is enclosed in the grey square shown in Figure 2.3a. The distance between the point heat source and the boundary $\partial B^{(1)}$ is smaller than H_c. Therefore, the method of images should be applied. In this case, an image source, J, is reflected with respect to $\partial B^{(1)}$ with a distance of H. This image source will have identical energy as the point heat source so that the heat flux in boundary $\partial B^{(1)}$ is zero. For this reason, the method of images is a useful solution to analytically enforce boundary conditions for the point sources located within a critical distance from the boundary. Since the point heat source, I is located at a distance greater than H_c from boundary $\partial B^{(2)}$, no image source is reflected with respect to this boundary. In this case, the numerical correction $\hat{T}$ will impose numerically the boundary conditions on the boundaries far away from the point and image sources, like boundary $\partial B^{(2)}$ in Figure 2.3a. On the other hand, Figure 2.3b shows a point heat source, I, located close to boundaries $\partial B^{(1)}$ and $\partial B^{(2)}$. In this case, the distance between the point heat source and both boundaries is smaller than H_c, so an image source is created with respect to each boundary, $J = 1$ and $J = 2$. Moreover, second order image sources are created as the reflection of image source $J = 1$ with respect to $\partial B^{(2)}$ and image source $J = 2$ with respect to $\partial B^{(1)}$. Since these second order image sources have the same location, due to the orthogonality of $\partial B^{(1)}$ and $\partial B^{(2)}$, just one second order image source, $J = 3$, is necessary, as shown in Figure 2.3b.

To represent the temperature field of all image sources, the temperature distribution of each image source is summed as

$$\check{T}(x_1, x_2, x_3, t) = \sum_{I=1}^{N} \sum_{J=1}^{N_I} \check{T}^{(J)}(x_1, x_2, x_3, t), \tag{2.19}$$

where N_I is the total number of image sources associated to the point source I, and $\check{T}^{(J)}(x_1, x_2, x_3, t)$ is the temperature field due to an image source J, where $J = 1, ..., N_I$. When $t \geq t_0^{(I)}$, $\check{T}^{(J)}(x_1, x_2, x_3, t)$ is represented by

$$\check{T}^{(J)}(x_1, x_2, x_3, t) = \frac{Q^{(J)} A}{4 \rho c_p (\pi \alpha (t - \tau_0^{(I)}))^{3/2}} exp\left(\frac{-(R^{(J)})^2}{4 \alpha (t - \tau_0^{(I)})} \right), \tag{2.20}$$

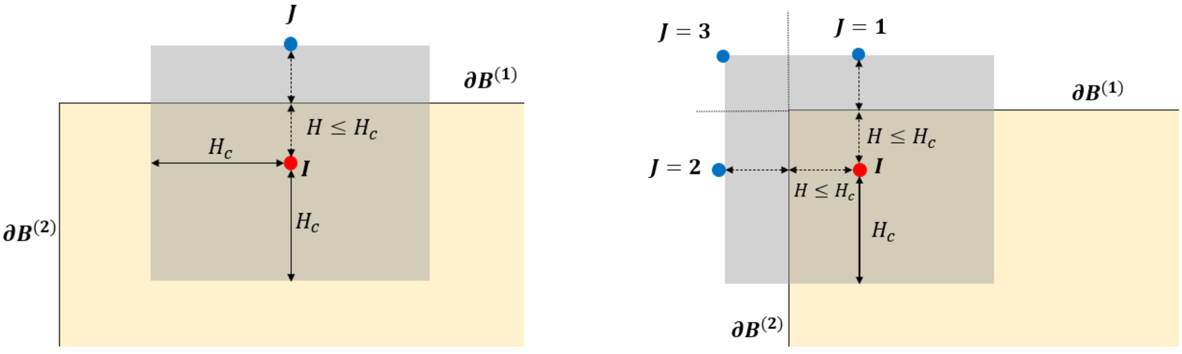

(a) (b)

Figure 2.3: Schematic illustration of the point heat source, I, and the creation of image sources, J. (a) Shows the point heat source, I, as the red point, located at a distance smaller than H_c from the boundary $\partial B^{(1)}$. An image source, J, represented by the blue point, is reflected symmetrically with respect to $\partial B^{(1)}$. Since the distance between this point source and boundary $\partial B^{(2)}$ is greater than H_c, no image source is reflected with respect to $\partial B^{(2)}$. (b) Shows the point heat source, I, located at a distance smaller than H_c from boundaries $\partial B^{(1)}$ and $\partial B^{(2)}$. Then, two image sources, $J = 1$ and $J = 2$, are reflected symmetrically with respect to $\partial B^{(1)}$ and $\partial B^{(2)}$, respectively. An additional image source, $J = 3$, is sufficient to reflect $J = 1$ with respect to $\partial B^{(2)}$ and $J = 2$ with respect to $\partial B^{(1)}$.

which is similar to $\tilde{T}^{(I)}(x_1, x_2, x_3, t)$ in Equation 2.9. As in Equation 2.9, A is the absorptivity fraction, and, in this case, $R^{(J)}$ is the distance between the material point of interest (x_1, x_2, x_3) and the position of the image source $(x_1^{(J)}, x_2^{(J)}, x_3^{(J)})$, that is: $(R^{(J)})^2 = (x_1 - x_1^{(J)})^2 + (x_2 - x_2^{(J)})^2 + (x_3 - x_3^{(J)})^2$. Furthermore, $Q^{(J)}$ is the energy associated to the image source, which is set equal to $Q^{(I)}$.

However, as explained before, the method of images used in [6] can only be applied in convex polyhedrons. As shown in Figure 2.1, the geometry of the body V of this thermal model is a non-convex polyhedron due to the L-shape corner. Because of this, if the method of images were to be employed as explained before and near the concave corner, it will not satisfy the boundary conditions. An erroneous heat flux will be created near the concave corner, as shown in Figure 1.14, and high temperature gradients will arise.

To be able to overcome these limitations and be able to use the method of images for any arbitrary shape, specifically be able to apply it in a non-convex polyhedron, the anisotropic mirror source model is proposed in this thesis.

2.4. Anisotropic mirror source

Figure 2.4 shows an schematic of the top surface of the domain in Figure 2.1, where the scan track (highlighted in red) is located near the concave corner. It can be seen that the scan track is divided in point heat sources $I = 1, \dots, N$, and each point source has a mirror image source $J = 1, \dots, N_I$ with respect to boundary $\partial B^{(1)}$. Due to the nature of Equation 2.20, the temperature distribution of the image sources J has the same distribution as the point sources I, as shown by the contour lines of point source $I = 1$ and mirror source $J = 1$ in Figure 2.4. From the point heat sources and the mirror image sources, heat will diffuse in the x_1, x_2 and x_3-direction, following Equations 2.8 and 2.20. As explained before, the use of mirror sources analytically enforces the boundary conditions on the boundaries close to the point heat sources. In this case, in Figure 2.4, the mirror sources correctly enforce the boundary condition of no heat flux in $\partial B^{(1)}$. This is because the steep temperature gradients of $\tilde{T}$ in the x_2-direction are cancelled out by the steep temperature gradients of $\check{T}$ in the x_2-direction. However, it can be seen that mirror sources located within a critical distance from boundary $\partial B^{(2)}$ also create steep temperature gradients in this boundary in the x_1-direction, which are not cancelled out by the temperature gradients of $\tilde{T}$. Moreover, these large temperature gradients of $\check{T}$ in the x_1-direction cannot be handled by the numerical correction of $\hat{T}$. Thus, the mirror sources closest to boundary $\partial B^{(2)}$ create a finite heat flux in the boundary, which interferes with the boundary condition of no heat flux imposed on ∂V_{lat}.

To overcome this problem, anisotropic mirror sources are introduced. The basis of the anisotropic

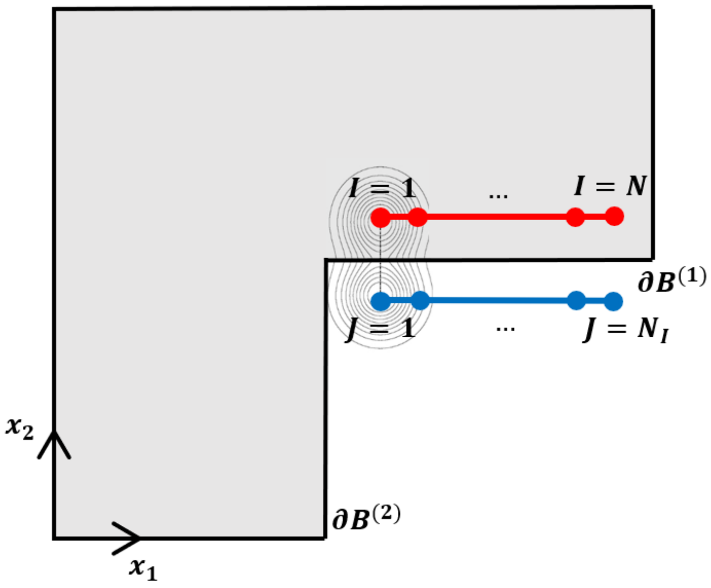

Figure 2.4: Schematic of the top surface of the non-convex domain of Figure 2.1, where the scan track of the point heat sources I are highlighted in red, and the mirror image sources J, highlighted in blue, are created with respect to boundary $\partial B^{(1)}$. The contour lines show how heat is diffused along x_1, x_2 and x_3-direction from the point heat sources and the mirror image sources. Note that the x_3-direction is perpendicular to x_1 and x_2, and it goes out the paper.

mirror sources is avoiding the creation of high heat flux in the boundaries near the concave corner. These type of mirror sources are anisotropic because they have high thermal conductivity in one direction and lower thermal conductivity in the other directions. Thus, heat flux will only be created in the directions where the thermal conductivity is lower. Depending on the boundary with respect to which the image source is reflected, the thermal conductivity will be different.

To represent the analytical solution of the temperature distribution of anisotropic mirror sources, from Equation 2.20, the thermal conductivity is changed by assigning k_1 to the x_1-direction, k_2 to the x_2-direction and k_3 to the x_3-direction, as shown in Equation 2.21.

$$\breve{T}^{(J)}(x_1, x_2, x_3, t) = \frac{Q^{(J)}A}{4\rho c_p(\pi\alpha(t-\tau_0^{(I)}))^{3/2}} exp\left[-\frac{1}{\frac{4}{\rho c_p}(t-\tau_0^{(I)})}\left(\frac{(x_1-x_1^{(J)})^2}{k_1}+\frac{(x_2-x_2^{(J)})^2}{k_2}+\frac{(x_3-x_3^{(J)})^2}{k_3}\right)\right] \tag{2.21}$$

Taking the example from Figure 2.4, the mirror sources $J = 1, ..., N_I$ of the point sources $I = 1, ..., N$ are reflected with respect to boundary $\partial B^{(1)}$. Since $\partial B^{(1)}$ is parallel to the x_1-direction, the thermal conductivity of the anisotropic mirror sources in the x_1-direction, k_1, will be higher than the thermal conductivity in the x_2- and x_3-direction, k_2 and k_3, respectively. For this reason, the temperature gradients with respect to x_1-direction of the anisotropic mirror sources will be zero and no heat flux will be created in the x_1-direction. This will satisfy the boundary condition of zero heat flux in $\partial B^{(2)}$ and mirror sources can be used to also ensure analytically the boundary condition in $\partial B^{(1)}$.

Hence, for the example in Figure 2.4, the thermal conductivity related to the x_1-direction of the mirror sources is considered to be much larger than the thermal conductivity of the other two directions (k_2 and k_3). This will affect the term $\frac{(x_1^{(J)}-x_1)^2}{k_1}$ as it would be zero as k_1 approaches to ∞.

Considering k_1 approaches to ∞, then $\frac{(x_1^{(J)}-x_1)^2}{k_1}$ becomes zero and Equation 2.21 is changed to the following expression:

$$\check{T}^{(J)}(x_2,x_3,t) = \frac{Q^{(J)}A}{4\rho c_p(\pi\alpha(t-\tau_0^{(I)}))^{3/2}} exp\left[-\frac{1}{\frac{4}{\rho c_p}(t-\tau_0^{(I)})}\left(\frac{(x_2-x_2^{(J)})^2}{k_2}+\frac{(x_3-x_3^{(J)})^2}{k_3}\right)\right]. \tag{2.22}$$

It can be seen that with this correction the temperature field of the mirror sources is no longer dependent on the x_1-coordinate. This changes the analytical solution of $\check{T}^{(J)}$ from a 3D case to 2D, in which only the x_2- and x_3-coordinates are taken into account in the formulation. Since the analytical solution is reduced to a 2D case, the term $(\pi\alpha(t-\tau_0^{(I)}))^{3/2}$ in Equation 2.22 needs to be change to $(\pi\alpha(t-\tau_0^{(I)}))^{2/2}$, following the fundamental solution of the heat equation [26, 27]. Moreover, it can be noted that the mirror sources are always created in the x_2-x_3 plane but in a line along the x_1-direction, as they have to replicate the scan track that the point heat sources create (as shown in Figure 2.4). To represent this effect, the anisotropic mirror sources are considered to be instantaneous point sources distributed in a line along the x_1-direction [28]. In this case, the heat represented by the anisotropic mirror sources is defined per unit length as: $Q^{(J)}/l$, where l is the length of the domain. Introducing these changes results in the following expression:

$$\check{T}^{(J)}(x_2,x_3,t) = \frac{Q^{(J)}A}{4\pi kl(t-\tau_0^{(I)})} exp\left[-\frac{1}{\frac{4}{\rho c_p}(t-\tau_0^{(I)})}\left(\frac{(x_2-x_2^{(J)})^2}{k_2}+\frac{(x_3-x_3^{(J)})^2}{k_3}\right)\right]. \tag{2.23}$$

Equation 2.23 is the analytical solution of the temperature distribution of the anisotropic mirror sources $J = 1,...,N_I$ of Figure 2.4.

This correction in the analytical solution of the anisotropic mirror sources created with respect to boundary $\partial B^{(1)}$ will not produce heat flux in the x_1-direction, as the thermal conductivity k_1 is high. This effect can be easily seen by deriving the temperature gradients of $\check{T}^{(J)}$ with respect to x_1, x_2 and x_3, as follows

$$\frac{\partial\check{T}}{\partial x_1} = 0, \tag{2.24}$$

$$\frac{\partial\check{T}}{\partial x_2} = \frac{Q^{(J)}A}{4\pi kl(t-\tau_0^{(I)})} exp\left[-\frac{1}{\frac{4}{\rho c_p}(t-\tau_0^{(I)})}\left(\frac{(x_2-x_2^{(J)})^2}{k_2}+\frac{(x_3-x_3^{(J)})^2}{k_3}\right)\right]\left(-\frac{2(x_2-x_2^{(J)})}{4\frac{k_2}{\rho c_p}(t-\tau_0^{(I)})}\right), \tag{2.25}$$

$$\frac{\partial\check{T}}{\partial x_3} = \frac{Q^{(J)}A}{4\pi kl(t-\tau_0^{(I)})} exp\left[-\frac{1}{\frac{4}{\rho c_p}(t-\tau_0^{(I)})}\left(\frac{(x_2-x_2^{(J)})^2}{k_2}+\frac{(x_3-x_3^{(J)})^2}{k_3}\right)\right]\left(-\frac{2(x_3-x_3^{(J)})}{4\frac{k_3}{\rho c_p}(t-\tau_0^{(I)})}\right). \tag{2.26}$$

It can be seen that because the temperature gradients of the mirror sources $J = 1,...,N_I$ are only created in the x_2 and x_3-directions, no heat flux will be created in the x_1-direction and it will satisfy the boundary condition on $\partial B^{(2)}$.

If the original point heat sources are placed differently, for example, as shown in Figure 2.5, parallel to boundary $\partial B^{(2)}$, Equation 2.21 will change. In this case, the mirror sources are reflected with respect to boundary $\partial B^{(2)}$. Thus, the thermal conductivity in x_2-direction will approach to infinity and the heat flux in the x_2-direction will be neglected. The analytical solution of the temperature distribution of image sources $J = 1,...,N_I$ will be described as shown in Equation 2.27, where no heat flux will be created in the x_2-direction and the boundary condition in $\partial B^{(1)}$ will be satisfied:

$$\check{T}^{(J)}(x_1,x_3,t) = \frac{Q^{(J)}A}{4\pi kw(t-\tau_0^{(I)})} exp\left[-\frac{1}{\frac{4}{\rho c_p}(t-\tau_0^{(I)})}\left(\frac{(x_1^{(J)}-x_1)^2}{k_1}+\frac{(x_3^{(J)}-x_3)^2}{k_3}\right)\right]. \tag{2.27}$$

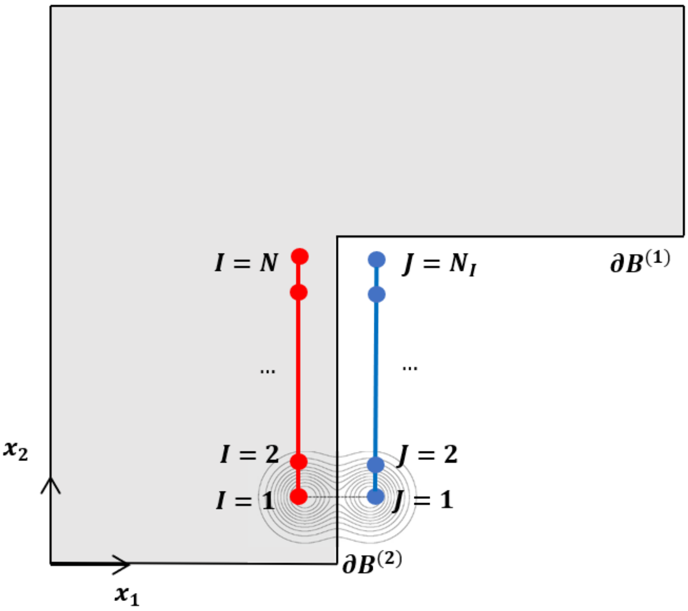

Figure 2.5: Schematic of the top surface of the domain of Figure 2.1, where the scan track of the point heat sources I, highlighted in red, is located parallel to $\partial B^{(2)}$, and its corresponding mirror image sources J, represented as the blue points, are reflected with respect to $\partial B^{(2)}$. As before, note that the x_3-direction is perpendicular to x_1 and x_2, and it goes out the paper.

Note that in this case the anisotropic mirror sources are distributed in a line along the x_2-direction and the heat represented by each mirror source is defined as $Q^{(J)}/w$, where w is the width of the domain. It can be seen that depending on the location of the anisotropic mirror sources, the heat represented is defined in terms of the dimension of the part parallel to the boundary of reflection.

Furthermore, the temperature field due to all image sources, $\check{T}$, is represented as shown in Equation 2.19, where the temperature field of each image source, $\check{T}^{(J)}$, is summed.

Finally, as mentioned in Section 2.2, the total temperature field, T, is modified to Equation 2.18 due to the addition of the correction done though the use of the method of images. Moreover, the temperature field $\hat{T}$ is still governed by Equation 2.11, but the boundary conditions are modified to

$$\hat{T} = T_c - \tilde{T} - \check{T} \quad \text{on } \partial V_{\text{bot}}, \tag{2.28}$$

$$\frac{\partial \hat{T}}{\partial \mathbf{x}} \cdot \mathbf{n} = -\frac{\partial \tilde{T}}{\partial \mathbf{x}} \cdot \mathbf{n} - \frac{\partial \check{T}}{\partial \mathbf{x}} \cdot \mathbf{n} \quad \text{on } \partial V_{\text{lat}}, \tag{2.29}$$

$$\frac{\partial \hat{T}}{\partial \mathbf{x}} \cdot \mathbf{m} = -\frac{\partial \tilde{T}}{\partial \mathbf{x}} \cdot \mathbf{m} - \frac{\partial \check{T}}{\partial \mathbf{x}} \cdot \mathbf{m} \quad \text{on } \partial V_{\text{top}}. \tag{2.30}$$

Both the temperature gradients of $\tilde{T}$ and $\check{T}$ are known as they can be calculated analytically. As in Equation 2.17, the temperature gradient of $\tilde{T}$ on ∂V_{top} is equal to zero. Moreover, with the same analysis, the temperature gradient of $\check{T}$ on ∂V_{top}, that is $\frac{\partial \check{T}}{\partial \mathbf{x}} \cdot \mathbf{m}$, is also equal to zero. The x_3-coordinate of the mirror sources has the same value as the x_3-coordinate of the material points of interest on ∂V_{top}. Therefore, Equation 2.30 can be rewritten as

$$\frac{\partial \hat{T}}{\partial \mathbf{x}} \cdot \mathbf{m} = 0 \quad \text{on } \partial V_{\text{top}}. \tag{2.31}$$

3

Numerical tools

In this chapter, the numerical tools used to obtain the temperature field $\hat{T}$, which will correct the analytical solution and enforce the boundary conditions, will be explained in detail. In the first section, the finite difference method will be explained using as an example a 3D convex polyhedron. Then, in the second section, the finite volume method will be introduced as an alternative to numerically calculate temperature fields in non-convex geometries.

3.1. Finite Difference Method

The finite difference method is an effective method to numerically solve the heat equation. With this method, temperature values at discrete spatial points in the domain can be calculated at different time instants by correctly discretizing the mathematical equations.

To be able to correctly explain how the finite difference method is implemented, as well as the corresponding boundary conditions, a simple cube which is a 3D convex polyhedron will be taken as an example. The convex polyhedron will be discretized in a finite number of grid points, as shown in Figure 3.1. In this case, an hexahedral finite difference cell with 8 grid points will be used. It can be seen in Figure 3.1 that there are five hexahedral cells in x-, y-, and z-directions, forming a 3D grid of the domain. Therefore, the blue points are the grid points where the temperature field should be determined. The distance between the grid points in the x-direction is Δx, in the y-direction is Δy, and in the z-direction is Δz.

Once the grid is formed, the finite difference method can be implemented. First, consider the interior grid points that are not part of the boundary. For these points, the heat equation (Equation 3.1) can be solved by approximating $\hat{T}$ with first order forward difference with respect to time and with second order center difference with respect to space, as shown in Equations 3.2,3.3, 3.4, and 3.5 respectively.

$$\frac{\partial \hat{T}}{\partial t} = \alpha\left(\frac{\partial^2 \hat{T}}{\partial x^2} + \frac{\partial^2 \hat{T}}{\partial y^2} + \frac{\partial^2 \hat{T}}{\partial z^2}\right) \tag{3.1}$$

$$\frac{\partial \hat{T}}{\partial t} = \frac{\hat{T}(x^{(i)}, y^{(j)}, z^{(k)}, t^{(n+1)}) - \hat{T}(x^{(i)}, y^{(j)}, z^{(k)}, t^{(n)})}{\Delta t} \tag{3.2}$$

$$\frac{\partial^2 \hat{T}}{\partial x^2} = \frac{\hat{T}(x^{(i-1)}, y^{(j)}, z^{(k)}, t^{(n)}) - 2\hat{T}(x^{(i)}, y^{(j)}, z^{(k)}, t^{(n)}) + \hat{T}(x^{(i+1)}, y^{(j)}, z^{(k)}, t^{(n)})}{(\Delta x)^2} \tag{3.3}$$

$$\frac{\partial^2 \hat{T}}{\partial y^2} = \frac{\hat{T}(x^{(i)}, y^{(j-1)}, z^{(k)}, t^{(n)}) - 2\hat{T}(x^{(i)}, y^{(j)}, z^{(k)}, t^{(n)}) + \hat{T}(x^{(i)}, y^{(j+1)}, z^{(k)}, t^{(n)})}{(\Delta y)^2} \tag{3.4}$$

$$\frac{\partial^2 \hat{T}}{\partial y^2} = \frac{\hat{T}(x^{(i)}, y^{(j)}, z^{(k-1)}, t^{(n)}) - 2\hat{T}(x^{(i)}, y^{(j)}, z^{(k)}, t^{(n)}) + \hat{T}(x^{(i)}, y^{(j)}, z^{(k+1)}, t^{(n)})}{(\Delta z)^2} \tag{3.5}$$

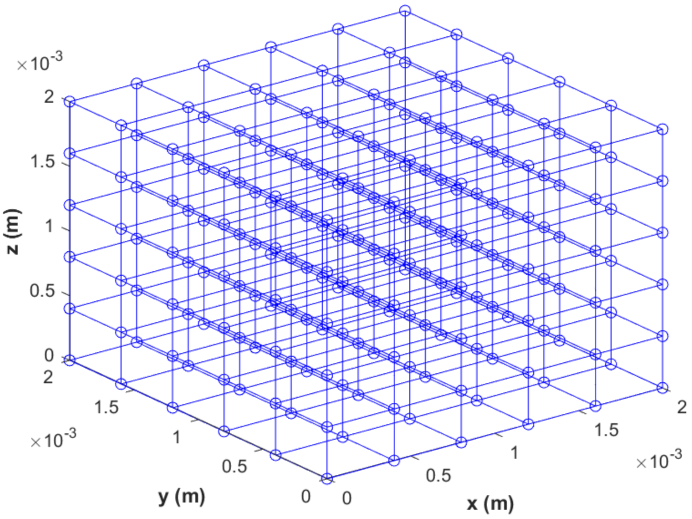

Figure 3.1: Schematic illustration of the 3D grid used to discretize a convex polyhedron. The distance between the grid points in the x-direction is Δx, in the y-direction is Δy, and in the z-direction is Δz.

Where x, y and z are the coordinates of the grid points and i, j and k are indices to locate the grid points in each direction in Figure 3.1. In the positive x-direction, the grid points are represented by i, where $i = 1, 2, 3, 4, 5, 6$, in the positive y-direction, $j = 1, 2, 3, 4, 5, 6$ and in the positive z-direction, $k = 1, 2, 3, 4, 5, 6$. For example, in Figure 3.1, the node located in $(x, y, z) = (0, 0, 0)$ m corresponds to $(i, j, k) = (1, 1, 1)$. On the other hand, t represents the time at which the temperature value of each node is calculated, where n discretizes t in different time steps.

By combining Equations 3.2, 3.3, 3.4 and 3.5 into Equation 3.1, the following expression is obtained

$$\begin{aligned}\frac{\hat{T}(x^{(i)}, y^{(j)}, z^{(k)}, t^{(n+1)}) - \hat{T}(x^{(i)}, y^{(j)}, z^{(k)}, t^{(n)})}{\Delta t} &= \\ \alpha\Bigg(\frac{\hat{T}(x^{(i-1)}, y^{(j)}, z^{(k)}, t^{(n)}) - 2\hat{T}(x^{(i)}, y^{(j)}, z^{(k)}, t^{(n)}) + \hat{T}(x^{(i+1)}, y^{(j)}, z^{(k)}, t^{(n)})}{(\Delta x)^2} \\ + \frac{\hat{T}(x^{(i)}, y^{(j-1)}, z^{(k)}, t^{(n)}) - 2\hat{T}(x^{(i)}, y^{(j)}, z^{(k)}, t^{(n)}) + \hat{T}(x^{(i)}, y^{(j+1)}, z^{(k)}, t^{(n)})}{(\Delta y)^2} \\ + \frac{\hat{T}(x^{(i)}, y^{(j)}, z^{(k-1)}, t^{(n)}) - 2\hat{T}(x^{(i)}, y^{(j)}, z^{(k)}, t^{(n)}) + \hat{T}(x^{(i)}, y^{(j)}, z^{(k+1)}, t^{(n)})}{(\Delta z)^2}\Bigg),\end{aligned} \tag{3.6}$$

and by simplifying, the temperature value of $\hat{T}$ at point $(x^{(i)}, y^{(j)}, z^{(k)})$ and time step $t^{(n+1)}$ is determined as follows

$$\begin{aligned}\hat{T}(x^{(i)}, y^{(j)}, z^{(k)}, t^{(n+1)}) &= \hat{T}(x^{(i)}, y^{(j)}, z^{(k)}, t^{(n)}) \\ &+ \alpha\Delta t\Bigg(\frac{\hat{T}(x^{(i-1)}, y^{(j)}, z^{(k)}, t^{(n)}) - 2\hat{T}(x^{(i)}, y^{(j)}, z^{(k)}, t^{(n)}) + \hat{T}(x^{(i+1)}, y^{(j)}, z^{(k)}, t^{(n)})}{(\Delta x)^2} \\ &+ \frac{\hat{T}(x^{(i)}, y^{(j-1)}, z^{(k)}, t^{(n)}) - 2\hat{T}(x^{(i)}, y^{(j)}, z^{(k)}, t^{(n)}) + \hat{T}(x^{(i)}, y^{(j+1)}, z^{(k)}, t^{(n)})}{(\Delta y)^2} \\ &+ \frac{\hat{T}(x^{(i)}, y^{(j)}, z^{(k-1)}, t^{(n)}) - 2\hat{T}(x^{(i)}, y^{(j)}, z^{(k)}, t^{(n)}) + \hat{T}(x^{(i)}, y^{(j)}, z^{(k+1)}, t^{(n)})}{(\Delta z)^2}\Bigg).\end{aligned} \tag{3.7}$$

For the interior grid points, the surrounding nodes are clearly defined and the temperature values of them are calculated easily in each time step.

To simplify the notation for the remaining of the chapter, the approximate value of $\hat{T}$ at the spatial point $(x^{(i)}, y^{(j)}, z^{(k)})$ at the temporal point $t^{(n)}$ will be denoted by $\hat{T}^{(n)}_{i,j,k}$, that is: $\hat{T}^{(n)}_{i,j,k} = \hat{T}(x^{(i)}, y^{(j)}, z^{(k)}, t^{(n)})$. Moreover, the spatial point will be denoted as (i, j, k) instead of $(x^{(i)}, y^{(j)}, z^{(k)})$, and the temporal point as n, instead of $t^{(n)}$.

Next, consider the points that are part of the boundary. As explained in Chapter 2, the boundary conditions imposed in the thermal problem are of type Dirichlet on ∂V_{bot} (Equation 2.28) and Neumann on ∂V_{lat} (Equation 2.29). For the points located in ∂V_{bot}, as shown in Figure 3.2, the boundary condition is easily imposed as it is dependent on the temperature of the base plate, T_c, and the analytical value of $\tilde{T}$ and $\check{T}$ of those points at the corresponding time step, as shown in Equation 2.28.

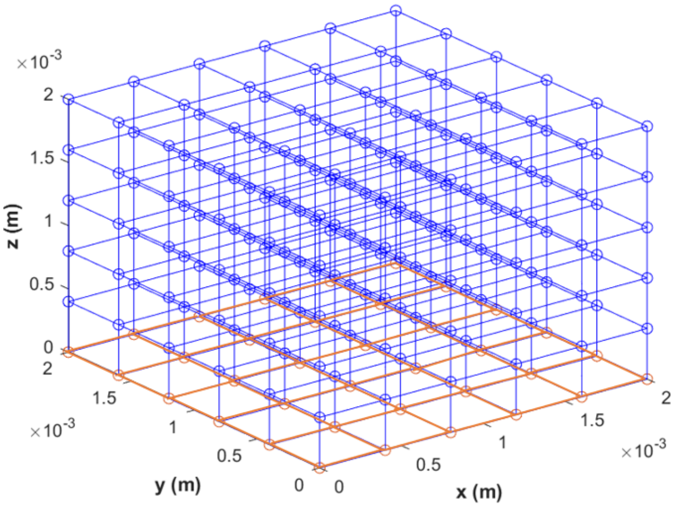

Figure 3.2: The grid points located at the bottom surface, ∂V_{bot}, are highlighted in orange.

For the points located in ∂V_{lat}, the boundary condition for $\hat{T}$ is of type Neumann with zero-heat flux, that is $\frac{\partial \hat{T}}{\partial \mathbf{x}} \cdot \mathbf{n} = 0$. Since the total temperature field is $T = \tilde{T} + \hat{T} + \check{T}$, this boundary condition is expressed in ∂V_{lat} as in Equation 2.29, that is the zero-heat flux condition is obtained by subtracting the temperature gradients of $\tilde{T}$ and $\check{T}$ with respect to the vector normal of each boundary point. To correctly apply the boundary conditions in ∂V_{lat}, each grid point should be classified in advance, given that, depending on the location of the grid points, the boundary conditions are implemented differently.

Figure 3.3 shows as an example the lateral boundary points of the front face of the convex shape. In this case, it is important to make a clear distinction between three different type of boundary points, which are highlighted in green, black and pink in Figure 3.3. The green grid point is a surface point, it is part of only one boundary (the front face of the domain). The black grid point is an edge point, as it is part of two boundaries and it is located on an edge of the cube. The pink grid point is a vertex or corner point, as it is part of three boundaries and it is located on a corner of the cube. This distinction is necessary because depending on the location of the boundary point, the finite difference scheme is applied different as these boundary points have different number of surrounding points to calculate the temperature gradients from. Figure 3.4 shows the difference between these boundary points, highlighting also their neighbouring points.

Consider the surface point in Figure 3.4, which is highlighted in green. The finite difference scheme for this point is implemented the same way as shown in Equation 3.7. However, it can be noted in Figure 3.5, that the point (i, j, k) only has five surrounding grid points and that the point that corresponds to $(i, j-1, k)$ is not part of the domain. This point is actually a virtual node of which the temperature is unknown. Moreover, the point (i, j, k) is a boundary point and the corresponding boundary conditions

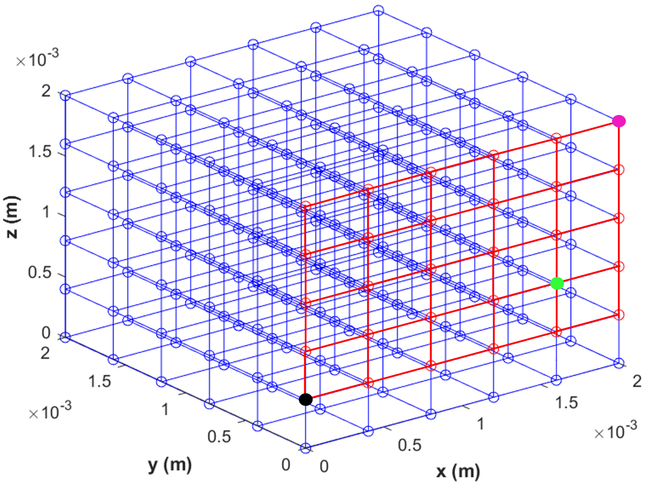

Figure 3.3: Example of lateral boundary points in the 3D grid. The red points are boundary points in the front face of the domain, and highlighted in green, black and pink are the three type of boundary points. It can be seen that the points on the bottom (with $z = 0$) are not highlighted in red as these points are part of the bottom boundary and they are not considered boundary points of ∂V_{lat}. It is also important to clarify that there are boundary points in the other three surfaces of ∂V_{lat} that are not highlighted in this figure.

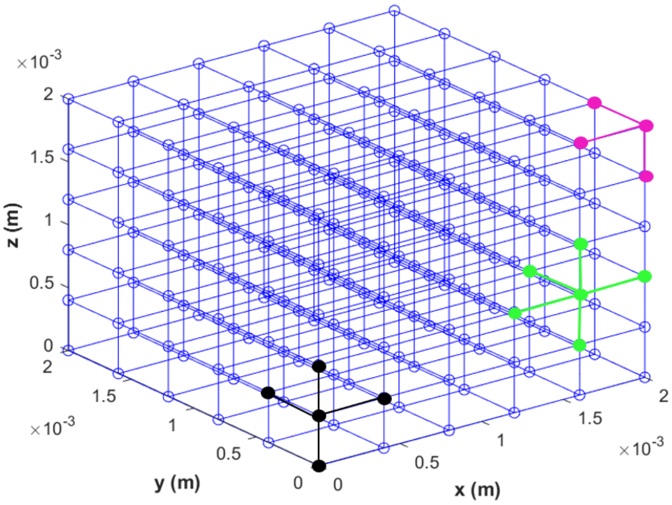

Figure 3.4: Example of the three different type of boundary points, surface, edge and vertex point, and its neighbouring grid points.

should be apply. Since this boundary point is located in ∂V_{lat}, Equation 2.29 will be used to apply boundary conditions. It can be seen in Equation 2.29 that the gradients of $\hat{T}$, $\tilde{T}$ and $\check{T}$ are in terms of the outward facing normal of the point of interest. The outward facing normal that corresponds to this surface point is **n** = [0, -1, 0], as it can be seen in Figure 3.5. Then, the first term of Equation 2.29 for this specific boundary point is the following

$$\frac{\partial \hat{T}}{\partial \mathbf{x}} \cdot \mathbf{n} = \left[\frac{\partial \hat{T}}{\partial x}, \frac{\partial \hat{T}}{\partial y}, \frac{\partial \hat{T}}{\partial z}\right] [0, -1, 0]^{\mathrm{T}} = -\frac{\partial \hat{T}}{\partial y}. \tag{3.8}$$

With the same analysis, the second term of Equation 2.29 can be calculated as follows

$$-\frac{\partial \tilde{T}}{\partial \mathbf{x}} \cdot \mathbf{n} - \frac{\partial \check{T}}{\partial \mathbf{x}} \cdot \mathbf{n} = -\left[\frac{\partial \tilde{T}}{\partial x}, \frac{\partial \tilde{T}}{\partial y}, \frac{\partial \tilde{T}}{\partial z}\right] [0, -1, 0]^{\mathrm{T}} - \left[\frac{\partial \check{T}}{\partial x}, \frac{\partial \check{T}}{\partial y}, \frac{\partial \check{T}}{\partial z}\right] [0, -1, 0]^{\mathrm{T}} = \left(\frac{\partial \tilde{T}}{\partial y} + \frac{\partial \check{T}}{\partial y}\right). \tag{3.9}$$

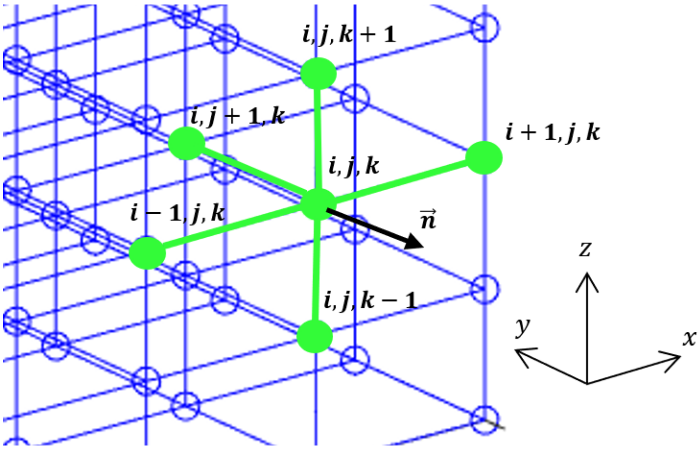

Figure 3.5: Example of a surface point and its corresponding surrounding grid points. The vector normal, **n**, related to the grid point is highlighted in black. This is a close up of Figure 3.4.

It can be noted that the terms related to x- and z-direction are eliminated in Equations 3.8 and 3.9, resulting in Equation 3.10. In this case, only the temperature gradients in the y-direction are considered as they are in the direction of the vector normal and they will generate the heat flux into the domain. Moreover, the heat flux created by the temperature gradients in the x- and z-direction are tangential to the surface so its influence in the heat flux is not relevant.

$$\frac{\partial \hat{T}}{\partial y} = -\left(\frac{\partial \tilde{T}}{\partial y} + \frac{\partial \check{T}}{\partial y}\right)\Bigg|_{i,j,k}^{n} \tag{3.10}$$

Note that the temperature gradients of $\tilde{T}$ and $\check{T}$ are evaluated on the grid point of interest (i, j, k) at n. Then, to apply the boundary conditions to this surface point, Equation 3.10 will be use. The term on the left will be approximated with second order center difference with respect to space, as follows

$$\frac{\partial \hat{T}}{\partial y} = \frac{\hat{T}^{(n)}_{i,j+1,k} - \hat{T}^{(n)}_{i,j-1,k}}{2\Delta y}. \tag{3.11}$$

By combining Equations 3.10 and 3.11, an expression for the temperature of the virtual point $(i, j-1, k)$ can be obtained, as shown in Equation 3.12, and be used to calculate the temperature of the point of interest (i, j, k).

$$\hat{T}^{(n)}_{i,j-1,k} = \hat{T}^{(n)}_{i,j+1,k} + 2\Delta y\left(\frac{\partial \tilde{T}}{\partial y} + \frac{\partial \check{T}}{\partial y}\right)\Bigg|_{i,j,k}^{n} \tag{3.12}$$

Then, combining Equations 3.7 and 3.12 results in the following expression

$$\begin{aligned}\hat{T}^{(n+1)}_{i,j,k} = \hat{T}^{(n)}_{i,j,k} + \alpha\Delta t \Bigg(&\frac{\hat{T}^{(n)}_{i-1,j,k} - 2\hat{T}^{(n)}_{i,j,k} + \hat{T}^{(n)}_{i+1,j,k}}{(\Delta x)^2} + \frac{\hat{T}^{(n)}_{i,j+1,k} + 2\Delta y\left(\frac{\partial \tilde{T}}{\partial y} + \frac{\partial \check{T}}{\partial y}\right)\Big|_{i,j,k}^{n} - 2\hat{T}^{(n)}_{i,j,k} + \hat{T}^{(n)}_{i,j+1,k}}{(\Delta y)^2} \\ &+ \frac{\hat{T}^{(n)}_{i,j,k-1} - 2\hat{T}^{(n)}_{i,j,k} + \hat{T}^{(n)}_{i,j,k-1}}{(\Delta z)^2}\Bigg).\end{aligned} \tag{3.13}$$

Lastly, rearranging the terms results in Equation 3.14 and the temperature at the surface point (i, j, k) can be calculated at every time step.

$$\hat{T}^{(n+1)}_{i,j,k} = \hat{T}^{(n)}_{i,j,k} + \alpha\Delta t\left(\frac{\hat{T}^{(n)}_{i-1,j,k} - 2\hat{T}^{(n)}_{i,j,k} + \hat{T}^{(n)}_{i+1,j,k}}{(\Delta x)^2} + \frac{2\hat{T}^{(n)}_{i,j+1,k} - 2\hat{T}^{(n)}_{i,j,k}}{(\Delta y)^2} + \frac{\hat{T}^{(n)}_{i,j,k-1} - 2\hat{T}^{(n)}_{i,j,k} + \hat{T}^{(n)}_{i,j,k+1}}{(\Delta z)^2} \right.$$
$$\left. + \frac{2}{\Delta y}\left(\frac{\partial \tilde{T}}{\partial y} + \frac{\partial \check{T}}{\partial y}\right)\Bigg|^{n}_{i,j,k}\right) \tag{3.14}$$

As it can be seen, the virtual point is used to correctly impose the boundary conditions on the boundary points, as well as being able to obtain an expression for the temperature of the point of interest (i, j, k) at any time step n.

For the case of the points on the edges, which are points that are part of two boundaries, the temperature values of $\hat{T}^{(n+1)}_{i,j,k}$ can be derived in the same way as before. In this case, as shown in Figure 3.6, these type of points have four surrounding points, so to accurately calculate the temperature of point (i, j, k), two virtual nodes should be defined by the boundary conditions. For this point, the virtual nodes correspond to $(i-1, j, k)$ and $(i, j-1, k)$.

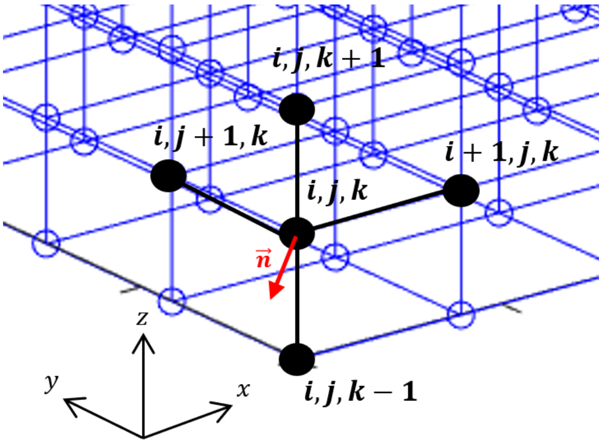

Figure 3.6: Example of an edge point, where its corresponding vector normal is highlighted in red. This is a close up of Figure 3.4.

It can be seen that for the point in Figure 3.6, the unit vector normal is $\mathbf{n}$ = [$\frac{-1}{\sqrt{2}}$, $\frac{-1}{\sqrt{2}}$, 0]. Then, Equation 2.29 can be used as before as follows

$$\frac{\partial \hat{T}}{\partial \mathbf{x}} \cdot \mathbf{n} = \left[\frac{\partial \hat{T}}{\partial x}, \frac{\partial \hat{T}}{\partial y}, \frac{\partial \hat{T}}{\partial z}\right]\left[\frac{-1}{\sqrt{2}}, \frac{-1}{\sqrt{2}}, 0\right]^{\mathrm{T}}, \tag{3.15}$$

$$-\frac{\partial \tilde{T}}{\partial \mathbf{x}} \cdot \mathbf{n} - \frac{\partial \check{T}}{\partial \mathbf{x}} \cdot \mathbf{n} = -\left[\frac{\partial \tilde{T}}{\partial x}, \frac{\partial \tilde{T}}{\partial y}, \frac{\partial \tilde{T}}{\partial z}\right]\left[\frac{-1}{\sqrt{2}}, \frac{-1}{\sqrt{2}}, 0\right]^{\mathrm{T}} - \left[\frac{\partial \check{T}}{\partial x}, \frac{\partial \check{T}}{\partial y}, \frac{\partial \check{T}}{\partial z}\right]\left[\frac{-1}{\sqrt{2}}, \frac{-1}{\sqrt{2}}, 0\right]^{\mathrm{T}}. \tag{3.16}$$

By combining the term in the x-direction of Equation 3.15 with Equation 3.16 and the term in the y-direction of Equation 3.15 with Equation 3.16, the finite difference scheme can be applied on the right hand side of the equation to obtain an expression for each virtual node.

$$\frac{\partial \hat{T}}{\partial x} = -\left(\frac{\partial \tilde{T}}{\partial x} + \frac{\partial \check{T}}{\partial x}\right)\Bigg|^{n}_{i,j,k} \tag{3.17}$$

$$\frac{\partial \hat{T}}{\partial x} = \frac{\hat{T}^{(n)}_{i+1,j,k} - \hat{T}^{(n)}_{i-1,j,k}}{2\Delta x} \tag{3.18}$$

$$\hat{T}^{(n)}_{i-1,j,k} = \hat{T}^{(n)}_{i+1,j,k} + 2\Delta x \left(\frac{\partial \tilde{T}}{\partial x} + \frac{\partial \breve{T}}{\partial x} \right) \Bigg|^{n}_{i,j,k} \tag{3.19}$$

$$\frac{\partial \hat{T}}{\partial y} = - \left(\frac{\partial \tilde{T}}{\partial y} + \frac{\partial \breve{T}}{\partial y} \right) \Bigg|^{n}_{i,j,k} \tag{3.20}$$

$$\frac{\partial \hat{T}}{\partial y} = \frac{\hat{T}^{(n)}_{i,j+1,k} - \hat{T}^{(n)}_{i,j-1,k}}{2\Delta y} \tag{3.21}$$

$$\hat{T}^{(n)}_{i,j-1,k} = \hat{T}^{(n)}_{i,j+1,k} + 2\Delta y \left(\frac{\partial \tilde{T}}{\partial y} + \frac{\partial \breve{T}}{\partial y} \right) \Bigg|^{n}_{i,j,k} \tag{3.22}$$

Then, substituting Equations 3.19 and 3.22 in Equation 3.7 results in the following expression

$$\begin{aligned} \hat{T}^{(n+1)}_{i,j,k} = \hat{T}^{(n)}_{i,j,k} + \alpha \Delta t \Bigg(& \frac{\hat{T}^{(n)}_{i+1,j,k} + 2\Delta x \left(\frac{\partial \tilde{T}}{\partial x} + \frac{\partial \breve{T}}{\partial x} \right) \Big|^{n}_{i,j,k} - 2\hat{T}^{(n)}_{i,j,k} + \hat{T}^{(n)}_{i+1,j,k}}{(\Delta x)^2} \\ & + \frac{\hat{T}^{(n)}_{i,j+1,k} + 2\Delta y \left(\frac{\partial \tilde{T}}{\partial y} + \frac{\partial \breve{T}}{\partial y} \right) \Big|^{n}_{i,j,k} - 2\hat{T}^{(n)}_{i,j,k} + \hat{T}^{(n)}_{i,j+1,k}}{(\Delta y)^2} + \frac{\hat{T}^{(n)}_{i,j,k-1} - 2\hat{T}^{(n)}_{i,j,k} + \hat{T}^{(n)}_{i,j,k+1}}{(\Delta z)^2} \Bigg). \end{aligned} \tag{3.23}$$

Rearranging the terms gives Equation 3.24, where the temperature value of $\hat{T}$ at the edge point (i, j, k) can be calculated at every time step by applying the boundary conditions correctly.

$$\begin{aligned} \hat{T}^{(n+1)}_{i,j,k} = \hat{T}^{(n)}_{i,j,k} + \alpha \Delta t \Bigg(& \frac{2\hat{T}^{(n)}_{i+1,j,k} - 2\hat{T}^{(n)}_{i,j,k}}{(\Delta x)^2} + \frac{2\hat{T}^{(n)}_{i,j+1,k} - 2\hat{T}^{(n)}_{i,j,k}}{(\Delta y)^2} + \frac{\hat{T}^{(n)}_{i,j,k-1} - 2\hat{T}^{(n)}_{i,j,k} + \hat{T}^{(n)}_{i,j,k+1}}{(\Delta z)^2} \\ & + \frac{2}{\Delta x} \left(\frac{\partial \tilde{T}}{\partial x} + \frac{\partial \breve{T}}{\partial x} \right) \Bigg|^{n}_{i,j,k} + \frac{2}{\Delta y} \left(\frac{\partial \tilde{T}}{\partial y} + \frac{\partial \breve{T}}{\partial y} \right) \Bigg|^{n}_{i,j,k} \Bigg) \end{aligned} \tag{3.24}$$

Lastly, for the points located in the corners of the convex domain, which are part of three boundaries, the analysis is done the same way. As an example, Figure 3.7, shows a corner point. It can be noted that it has three surrounding nodes, so three virtual nodes will be necessary to accurately calculate $\hat{T}$ for point (i, j, k). The virtual nodes are $(i + 1, j, k)$, $(i, j - 1, k)$, and $(i, j, k + 1)$. For this point, the corresponding unit vector normal is $\mathbf{n} = [\frac{1}{\sqrt{3}}, \frac{-1}{\sqrt{3}}, \frac{1}{\sqrt{3}}]$. Then, to accurately apply the boundary conditions, Equation 2.29 can be derived for this corner point as follows

$$\frac{\partial \hat{T}}{\partial \mathbf{x}} \cdot \mathbf{n} = \left[\frac{\partial \hat{T}}{\partial x}, \frac{\partial \hat{T}}{\partial y}, \frac{\partial \hat{T}}{\partial z} \right] \left[\frac{1}{\sqrt{3}}, \frac{-1}{\sqrt{3}}, \frac{1}{\sqrt{3}} \right]^{\mathrm{T}}, \tag{3.25}$$

$$-\frac{\partial \tilde{T}}{\partial \mathbf{x}} \cdot \mathbf{n} - \frac{\partial \breve{T}}{\partial \mathbf{x}} \cdot \mathbf{n} = - \left[\frac{\partial \tilde{T}}{\partial x}, \frac{\partial \tilde{T}}{\partial y}, \frac{\partial \tilde{T}}{\partial z} \right] \left[\frac{1}{\sqrt{3}}, \frac{-1}{\sqrt{3}}, \frac{1}{\sqrt{3}} \right]^{\mathrm{T}} - \left[\frac{\partial \breve{T}}{\partial x}, \frac{\partial \breve{T}}{\partial y}, \frac{\partial \breve{T}}{\partial z} \right] \left[\frac{1}{\sqrt{3}}, \frac{-1}{\sqrt{3}}, \frac{1}{\sqrt{3}} \right]^{\mathrm{T}}, \tag{3.26}$$

$$\frac{\partial \hat{T}}{\partial x} = - \left(\frac{\partial \tilde{T}}{\partial x} + \frac{\partial \breve{T}}{\partial x} \right) \Bigg|^{n}_{i,j,k}, \tag{3.27}$$

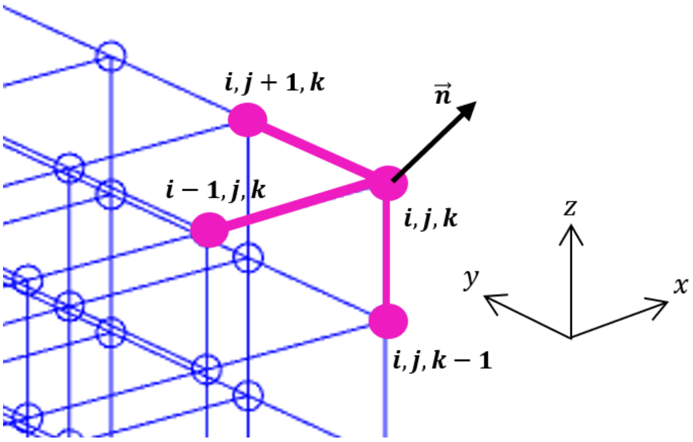

Figure 3.7: Example of a vertex or corner point. This is a close up of Figure 3.4.

$$\frac{\partial \hat{T}}{\partial x} = \frac{\hat{T}^{(n)}_{i+1,j,k} - \hat{T}^{(n)}_{i-1,j,k}}{2\Delta x}, \tag{3.28}$$

$$\hat{T}^{(n)}_{i+1,j,k} = \hat{T}^{(n)}_{i-1,j,k} - 2\Delta x \left(\frac{\partial \tilde{T}}{\partial x} + \frac{\partial \breve{T}}{\partial x} \right) \bigg|^{n}_{i,j,k}, \tag{3.29}$$

$$\frac{\partial \hat{T}}{\partial y} = -\left(\frac{\partial \tilde{T}}{\partial y} + \frac{\partial \breve{T}}{\partial y} \right) \bigg|^{n}_{i,j,k}, \tag{3.30}$$

$$\frac{\partial \hat{T}}{\partial y} = \frac{\hat{T}^{(n)}_{i,j+1,k} - \hat{T}^{(n)}_{i,j-1,k}}{2\Delta y}, \tag{3.31}$$

$$\hat{T}^{(n)}_{i,j-1,k} = \hat{T}^{(n)}_{i,j+1,k} + 2\Delta y \left(\frac{\partial \tilde{T}}{\partial y} + \frac{\partial \breve{T}}{\partial y} \right) \bigg|^{n}_{i,j,k}, \tag{3.32}$$

$$\frac{\partial \hat{T}}{\partial z} = -\left(\frac{\partial \tilde{T}}{\partial z} + \frac{\partial \breve{T}}{\partial z} \right) \bigg|^{n}_{i,j,k}, \tag{3.33}$$

$$\frac{\partial \hat{T}}{\partial z} = \frac{\hat{T}^{(n)}_{i,j,k+1} - \hat{T}^{(n)}_{i,j,k-1}}{2\Delta z}, \tag{3.34}$$

$$\hat{T}^{(n)}_{i,j,k+1} = \hat{T}^{(n)}_{i,j,k-1} - 2\Delta z \left(\frac{\partial \tilde{T}}{\partial z} + \frac{\partial \breve{T}}{\partial z} \right) \bigg|^{n}_{i,j,k}. \tag{3.35}$$

Furthermore, substituting Equations 3.29, 3.32 and 3.35 into Equation 3.7 results in the following expression

$$\hat{T}_{i,j,k}^{(n+1)} = \hat{T}_{i,j,k}^{(n)} + \alpha\Delta t \left(\frac{\hat{T}_{i-1,j,k}^{(n)} - 2\hat{T}_{i,j,k}^{(n)} + \hat{T}_{i-1,j,k}^{(n)} - 2\Delta x \left(\frac{\partial \tilde{T}}{\partial x} + \frac{\partial \breve{T}}{\partial x} \right) \Big|_{i,j,k}^{n}}{(\Delta x)^2} \right.$$
$$\left. + \frac{\hat{T}_{i,j+1,k}^{(n)} + 2\Delta y \left(\frac{\partial \tilde{T}}{\partial y} + \frac{\partial \breve{T}}{\partial y} \right) \Big|_{i,j,k}^{n} - 2\hat{T}_{i,j,k}^{(n)} + \hat{T}_{i,j+1,k}^{(n)}}{(\Delta y)^2} + \frac{\hat{T}_{i,j,k-1}^{(n)} - 2\hat{T}_{i,j,k}^{(n)} + \hat{T}_{i,j,k-1}^{(n)} - 2\Delta z \left(\frac{\partial \tilde{T}}{\partial z} + \frac{\partial \breve{T}}{\partial z} \right) \Big|_{i,j,k}^{n}}{(\Delta z)^2} \right). \tag{3.36}$$

Finally, rearranging the terms results in Equation 3.37, which calculates the temperature value of $\hat{T}$ at point (i, j, k) in each time step:

$$\hat{T}_{i,j,k}^{(n+1)} = \hat{T}_{i,j,k}^{(n)} + \alpha\Delta t \left(\frac{2\hat{T}_{i-1,j,k}^{(n)} - 2\hat{T}_{i,j,k}^{(n)}}{(\Delta x)^2} + \frac{2\hat{T}_{i,j+1,k}^{(n)} - 2\hat{T}_{i,j,k}^{(n)}}{(\Delta y)^2} + \frac{2\hat{T}_{i,j,k-1}^{(n)} - 2\hat{T}_{i,j,k}^{(n)}}{(\Delta z)^2} \right.$$
$$\left. - \frac{2}{\Delta x} \left(\frac{\partial \tilde{T}}{\partial x} + \frac{\partial \breve{T}}{\partial x} \right) \Big|_{i,j,k}^{n} + \frac{2}{\Delta y} \left(\frac{\partial \tilde{T}}{\partial y} + \frac{\partial \breve{T}}{\partial y} \right) \Big|_{i,j,k}^{n} - \frac{2}{\Delta z} \left(\frac{\partial \tilde{T}}{\partial z} + \frac{\partial \breve{T}}{\partial z} \right) \Big|_{i,j,k}^{n} \right). \tag{3.37}$$

3.2. Finite Volume Method in Non-Convex Geometries

For the anisotropic mirror source model that is presented in this thesis, the geometry to be consider is the non-convex domain of Figure 2.1. As it can be seen in Figure 3.8, the grid of the non-convex domain is created in the same way as the convex domain of Figure 3.1, where the distance between the grid points in the x-direction is Δx, in the y-direction is Δy, and in the z-direction is Δz. The temperature field $\hat{T}$ is calculated as explained in the previous section, by imposing the boundary conditions and obtaining the correct expressions for each virtual point of the boundary points. However, in the non-convex domain, it can be noted that there are grid points located right at the boundary where the concave corner is formed, as highlighted in Figure 3.9. These points are boundary points to which the corresponding boundary conditions must be enforced. However, because these points have six surrounding nodes, as shown in Figure 3.10, that are part of the domain, the temperature value of these boundary points can be easily calculated at every time step following Equation 3.7. But by just applying Equation 3.7 in these concave boundary points, the temperature value of $\hat{T}$ at point (i, j, k) will not be correctly calculated because the boundary conditions will not be taken into account.

To be able to correctly impose the boundary conditions and calculate $\hat{T}$ in these concave boundary points, a similar method to the finite difference method will be used: the finite volume method. The finite volume method was developed to be able to solve heat-flow problems of complex geometry, like the one presented in Figure 3.8. This method is based on an energy (heat) balance for an isolated finite volume, in which the conservation laws are applied to specific regions in space called control volumes. The domain, in which the energy balance is applied, is divided in control volumes that are related to the grid points. By satisfying the heat balance for each individual control volume, the heat flux and temperature distribution can be determined with high accuracy in the domain [29, 30].

To explain the finite volume method, consider the example given by the 2D L-shape domain shown in Figure 3.11. Assume that the boundaries of the domain are insulated, which means that a zero-heat flux boundary condition should be imposed, and the domain is divided in control volumes. In this case, the boundaries of the control volumes will be located halfway between the grid points, which establishes the grid points in the geometric center of the control volume. As explained in the previous section, the blue points in Figure 3.11 are the grid points where the temperature field $\hat{T}$ should be determined.

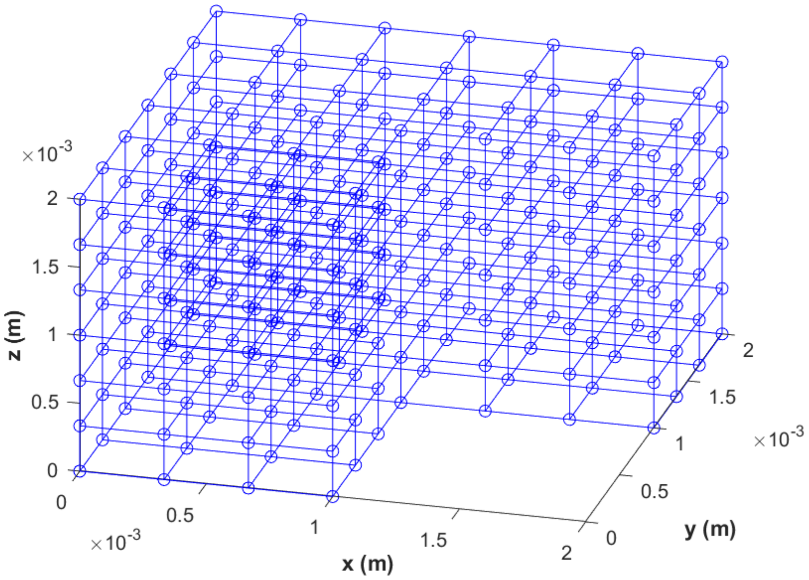

Figure 3.8: Schematic illustration of a 3D grid used in the non-convex domain. This grid is coarser than the one use for the implementation but gives an idea of how the grid points are connected between each other. The distance between the grid points in the x-direction is Δx, in the y-direction is Δy, and in the z-direction is Δz.

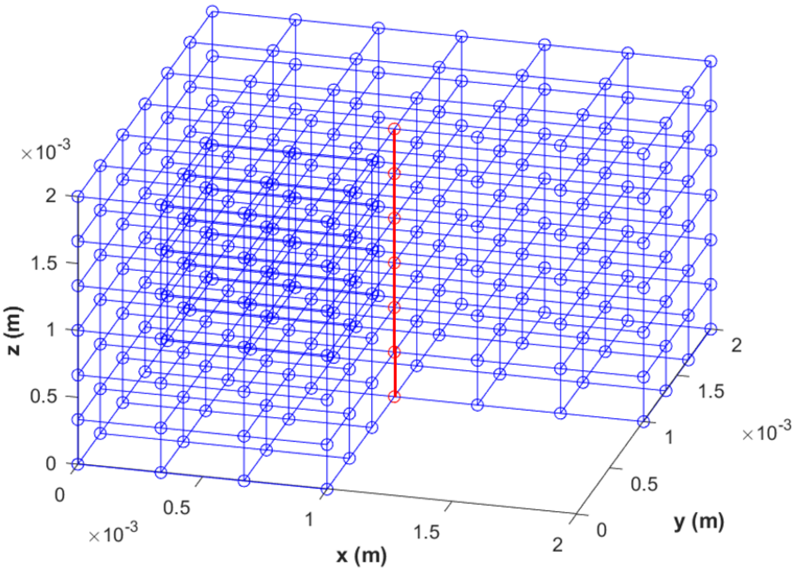

Figure 3.9: The red points represent the concave boundary points of this 3D non-convex domain. The edge is also highlighted in red, it can be seen that this edge is part of two boundaries.

First, consider the interior grid points that are not part of the boundary. For these points, the heat equation (Equation 3.38) can be solved with the finite difference method, by approximating with forward difference with respect to time and with center difference with respect to space, as shown in Equations 3.39, 3.40, 3.41, respectively:

$$\frac{\partial \hat{T}}{\partial t} = \alpha \left(\frac{\partial^2 \hat{T}}{\partial x^2} + \frac{\partial^2 \hat{T}}{\partial y^2} \right), \tag{3.38}$$

$$\frac{\partial \hat{T}}{\partial t} = \frac{\hat{T}_{i,j}^{(n+1)} - \hat{T}_{i,j}^{(n)}}{\Delta t}, \tag{3.39}$$

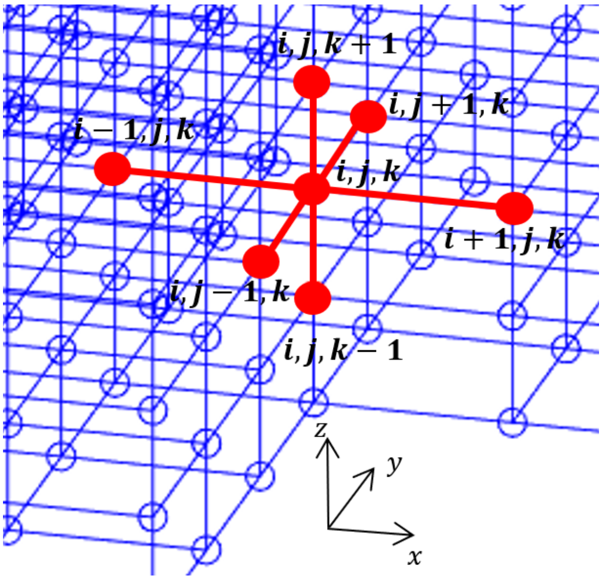

Figure 3.10: Close up view of the concave boundary point (i, j, k), where it can be seen its corresponding six neighboring grid points are also highlighted in red.

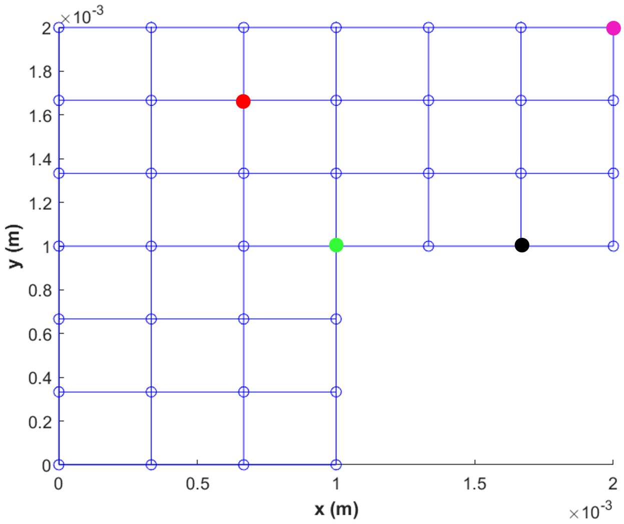

Figure 3.11: Schematic of the uniform grid of a 2D L-shape domain, where the blue points are the grid points. The distance between the grid points in the x-direction is Δx and in the y-direction is Δy. The red point represents an interior grid point, while the black, pink and green points represent an edge, vertex and inner corner point, respectively, which are boundary points.

$$\frac{\partial^2 \hat{T}}{\partial x^2} = \frac{\hat{T}^{(n)}_{i-1,j} - 2\hat{T}^{(n)}_{i,j} + \hat{T}^{(n)}_{i+1,j}}{(\Delta x)^2}, \tag{3.40}$$

$$\frac{\partial^2 \hat{T}}{\partial y^2} = \frac{\hat{T}^{(n)}_{i,j-1} - 2\hat{T}^{(n)}_{i,j} + \hat{T}^{(n)}_{i,j+1}}{(\Delta y)^2}. \tag{3.41}$$

Note that the same notation as the previous section is adopted here but in a 2D coordinate system, where the spatial point is denoted by (i, j), the temporal point is denoted by n, and the temperature field is denoted as $\hat{T}^{(n)}_{i,j}$.

As in the previous section, combining Equations 3.39, 3.40 and 3.41 results in Equation 3.42. This expression calculates the temperature field $\hat{T}$ of all the interior points in the 2D L-shape.

$$\hat{T}_{i,j}^{(n+1)} = \hat{T}_{i,j}^{(n)} + \alpha\Delta t\left(\frac{\hat{T}_{i-1,j}^{(n)} - 2\hat{T}_{i,j}^{(n)} + \hat{T}_{i+1,j}^{(n)}}{(\Delta x)^2} + \frac{\hat{T}_{i,j-1}^{(n)} - 2\hat{T}_{i,j}^{(n)} + \hat{T}_{i,j+1}^{(n)}}{(\Delta y)^2}\right) \tag{3.42}$$

It is important to emphasize that Equation 3.42 can also be obtained using the finite volume method and the energy balance equation. In this case, the energy balance should be applied to a control volume where the time rate at which the energy stored in the volume increases must equal to the net rate at which energy is transferred into the volume. For the interior grid point, highlighted in red in Figure 3.11, the control volume in which the energy balance equation should be applied is shown in Figure 3.12, highlighted in black. As the example is a 2D case, the control volume becomes a control area, denoted by S, that has a size of Δx Δy, and it is the square highlighted in black in Figure 3.12. The boundaries of the control area, S, are highlighted in yellow in Figure 3.12, where L represents the contour of the control area.

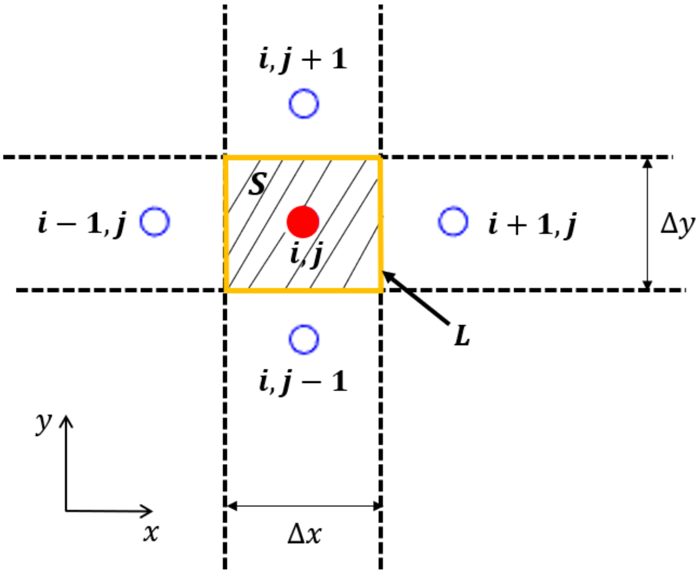

Figure 3.12: Example of an interior point (i, j) and its corresponding control area, S. It can be seen that the control area is the square highlighted in black and it has a size of Δx Δy. The boundaries of the control area are highlighted in yellow, where L represents the contour of the area. In this control area the finite volume method will be applied for this specific grid point (i, j).

Following the formulation of [30], first integrating over the control area, the 2D heat conduction equation (Equation 3.38) results in the following expression.

$$\iint_S \left(\rho c_p \frac{\partial \hat{T}}{\partial t} + \nabla \mathbf{q}\right) dxdy = 0, \tag{3.43}$$

where **q** is the heat flux vector given by **q** = $-k\nabla\hat{T}$. Applying the divergence theorem gives the following result

$$\iint_S \rho c_p \frac{\partial \hat{T}}{\partial t}\, dxdy + \oint_L \mathbf{q}\cdot\mathbf{n}\, ds = 0. \tag{3.44}$$

The term on the left represents the time rate at which the energy stored in the area, S, increases and can be evaluated by assuming that the temperature at the point (i,j) is the mean value for the area, by applying a first order forward difference with respect to time, as follows

$$\rho c_p \frac{(\hat{T}_{i,j}^{(n+1)} - \hat{T}_{i,j}^{(n)})}{\Delta t}\Delta x\Delta y. \tag{3.45}$$

The term on the right in Equation 3.44 represents the net rate at which energy is transferred into the area. In this case, it represents the heat flow out of the four boundaries of the control area for point

(i,j). For each boundary of the control area, S, the heat flux vector, **q**, should be evaluated in terms of the vector normal, **n**, of each boundary. The heat flow is represented by the heat flux components in terms of the temperature: $q_x = -k\frac{\partial \hat{T}}{\partial x}$ and $q_y = -k\frac{\partial \hat{T}}{\partial y}$. Hence, the right term results in the following expression

$$-k\Delta y \frac{\partial \hat{T}}{\partial x}\bigg|_{i+\frac{1}{2},j} - k\Delta x \frac{\partial \hat{T}}{\partial y}\bigg|_{i,j+\frac{1}{2}} + k\Delta y \frac{\partial \hat{T}}{\partial x}\bigg|_{i-\frac{1}{2},j} + k\Delta x \frac{\partial \hat{T}}{\partial y}\bigg|_{i,j-\frac{1}{2}}. \tag{3.46}$$

The $\frac{1}{2}$ subscript represents the halfway between the grid points where the boundary of the control area is located at. The following equation is obtained by approximating the spatial derivatives of Equation 3.46 by first order central difference with respect to space, taking the points $(i+\frac{1}{2},j)$, $(i-\frac{1}{2},j)$, etc., as the center points and combining it with Equation 3.45.

$$\rho c_p \frac{(\hat{T}_{i,j}^{(n+1)} - \hat{T}_{i,j}^{(n)})}{\Delta t}\Delta x\Delta y + k\Delta y\frac{(\hat{T}_{i,j}^{(n)} - \hat{T}_{i+1,j}^{(n)})}{\Delta x} + k\Delta x\frac{(\hat{T}_{i,j}^{(n)} - \hat{T}_{i,j+1}^{(n)})}{\Delta y} + k\Delta y\frac{(\hat{T}_{i,j}^{(n)} - \hat{T}_{i-1,j}^{(n)})}{\Delta x} + k\Delta x\frac{(\hat{T}_{i,j}^{(n)} - \hat{T}_{i,j-1}^{(n)})}{\partial y} = 0 \tag{3.47}$$

Rearranging the terms and setting the diffusivity as $\alpha = k/\rho c_p$, results in Equation 3.48, which can be seen corresponds to the finite difference expression of the 2D heat equation shown before, in Equation 3.42.

$$\hat{T}_{i,j}^{(n+1)} = \hat{T}_{i,j}^{(n)} + \alpha\Delta t\left(\frac{\hat{T}_{i-1,j}^{(n)} - 2\hat{T}_{i,j}^{(n)} + \hat{T}_{i+1,j}^{(n)}}{(\Delta x)^2} + \frac{\hat{T}_{i,j-1}^{(n)} - 2\hat{T}_{i,j}^{(n)} + \hat{T}_{i,j+1}^{(n)}}{(\Delta y)^2}\right) \tag{3.48}$$

This same analysis can be applied to obtain an expression of the temperature field $\hat{T}$ for the boundary points of Figure 3.11. As mentioned in the previous section, for the points located at the boundaries, the corresponding boundary conditions must be applied. In this case, the boundaries of Figure 3.11 are considered to be fully insulated, so a zero-heat flux boundary condition is imposed. Figure 3.13 shows a boundary point, which is an edge point, and its corresponding control area. In this case, the control area has a size of Δx Δy/2, since the point $(i,j-1)$ is not part of the domain and it is considered as a virtual point.

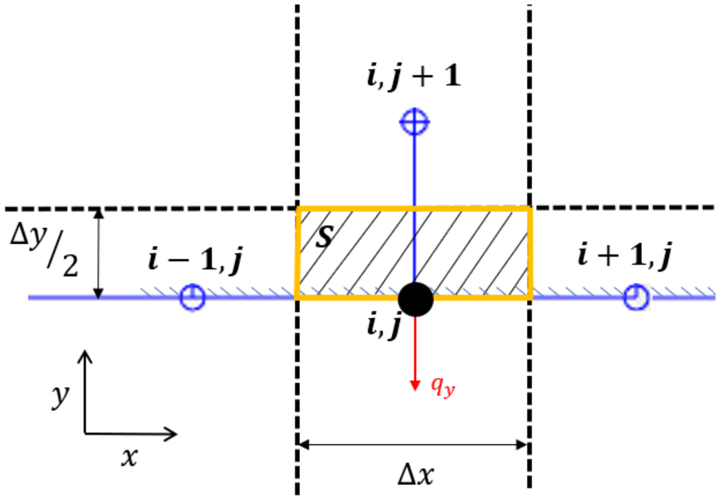

Figure 3.13: Example of a boundary point and its corresponding control area. In this case, the boundary point is an edge point and the control area, which is highlighted in black shadow, has a size of Δx Δy/2. The heat flow out of the bottom boundary of the control area is highlighted in red. Recall that the yellow lines represent the boundary of the control area.

Following the same steps as before, the left term of Equation 3.44 can be expanded as follows, taking into account the size of control area shown as Δx Δy/2:

$$\rho c_p \frac{(\hat{T}_{i,j}^{(n+1)} - \hat{T}_{i,j}^{(n)})}{\Delta t} \Delta x \frac{\Delta y}{2}. \tag{3.49}$$

For the case of the right term of Equation 3.44, the heat flow out of the control area of Figure 3.13 should be considered. It can be seen, that the bottom boundary of the control area doesn't have a corresponding grid point, due to (i, j) being a boundary point. For this reason, the heat flux out of this boundary will be due to the gradients of the analytical solutions of $\tilde{T}$ and $\check{T}$ so that a zero-heat flux boundary condition is imposed, following Equation 2.29. As shown in Figure 3.13, the heat flux vector of the bottom boundary of the control area is in the negative y-direction. This is because the outward vector normal of this boundary is **n** = [0, -1]. Therefore, the heat flux vector will be defined as follows

$$\mathbf{q} = -k \frac{\partial \hat{T}}{\partial \mathbf{x}} \cdot \mathbf{n}, \tag{3.50}$$

$$\mathbf{q} = -k \frac{\partial \hat{T}}{\partial \mathbf{x}} \cdot \mathbf{n} = -k \left[\frac{\partial \hat{T}}{\partial x}, \frac{\partial \hat{T}}{\partial y} \right] [0, -1]^{\mathrm{T}} = -k \left(-\frac{\partial \hat{T}}{\partial y} \right). \tag{3.51}$$

The temperature gradients of $\hat{T}$ are defined by the temperature gradients of $\tilde{T}$ and $\check{T}$, following Equation 2.29. Thus, the heat flux of the bottom boundary of the control area of Figure 3.13 will be defined as follows

$$-\frac{\partial \tilde{T}}{\partial \mathbf{x}} \cdot \mathbf{n} - \frac{\partial \check{T}}{\partial \mathbf{x}} \cdot \mathbf{n} = -\left[\frac{\partial \tilde{T}}{\partial x}, \frac{\partial \tilde{T}}{\partial y} \right] [0, -1]^{\mathrm{T}} - \left[\frac{\partial \check{T}}{\partial x}, \frac{\partial \check{T}}{\partial y} \right] [0, -1]^{\mathrm{T}} = \frac{\partial \tilde{T}}{\partial y} + \frac{\partial \check{T}}{\partial y}, \tag{3.52}$$

$$\frac{\partial \hat{T}}{\partial y} = -\left(\frac{\partial \tilde{T}}{\partial y} + \frac{\partial \check{T}}{\partial y} \right) \bigg|_{i,j}^{n}, \tag{3.53}$$

$$q_y = -k \left(-\frac{\partial \hat{T}}{\partial y} \right) = -k \left(\frac{\partial \tilde{T}}{\partial y} + \frac{\partial \check{T}}{\partial y} \right) \bigg|_{i,j}^{n}. \tag{3.54}$$

As explained previously, note that the temperature gradients of $\tilde{T}$ and $\check{T}$ are evaluated on the grid point (i, j) at time step n.

For the other three boundaries of the control volume, the heat flux vectors are obtained as shown in Equation 3.46. However, in this case, the boundary condition of Equation 3.54 should be included instead of the heat flux of the virtual point $(i, j-1)$, as shown Equation 3.55.

$$-k \frac{\Delta y}{2} \frac{\partial \hat{T}}{\partial x} \bigg|_{i+\frac{1}{2},j} - k \Delta x \frac{\partial \hat{T}}{\partial y} \bigg|_{i,j+\frac{1}{2}} + k \frac{\Delta y}{2} \frac{\partial \hat{T}}{\partial x} \bigg|_{i-\frac{1}{2},j} - k \Delta x \left(\frac{\partial \tilde{T}}{\partial y} + \frac{\partial \check{T}}{\partial y} \right) \bigg|_{i,j}^{n} \tag{3.55}$$

Then, approximating the spatial derivatives of Equation 3.55 by first order central difference and combining it with Equation 3.49 results in the following expression

$$\begin{aligned} \rho c_p \frac{(\hat{T}_{i,j}^{(n+1)} - \hat{T}_{i,j}^{(n)})}{\Delta t} \Delta x \frac{\Delta y}{2} + k \frac{\Delta y}{2} \frac{(\hat{T}_{i,j}^{(n)} - \hat{T}_{i+1,j}^{(n)})}{\Delta x} + k \Delta x \frac{(\hat{T}_{i,j}^{(n)} - \hat{T}_{i,j+1}^{(n)})}{\Delta y} + k \frac{\Delta y}{2} \frac{(\hat{T}_{i,j}^{(n)} - \hat{T}_{i-1,j}^{(n)})}{\Delta x} \\ - k \Delta x \left(\frac{\partial \tilde{T}}{\partial y} + \frac{\partial \check{T}}{\partial y} \right) \bigg|_{i,j}^{n} = 0. \end{aligned} \tag{3.56}$$

Rearranging the terms results in Equation 3.57, which gives the temperature value of $\hat{T}$ at the surface point (i, j) in each time step. It can be noted that Equation 3.57 is a similar expression to Equation 3.14 but in two dimensions.

$$\hat{T}_{i,j}^{(n+1)} = \hat{T}_{i,j}^{(n)} + \alpha \Delta t \left(\frac{\hat{T}_{i-1,j}^{(n)} - 2\hat{T}_{i,j}^{(n)} + \hat{T}_{i+1,j}^{(n)}}{(\Delta x)^2} + \frac{2\hat{T}_{i,j+1}^{(n)} - 2\hat{T}_{i,j}^{(n)}}{(\Delta y)^2} + \frac{2}{\Delta y} \left(\frac{\partial \tilde{T}}{\partial y} + \frac{\partial \breve{T}}{\partial y} \right) \Big|_{i,j}^{n} \right) \tag{3.57}$$

For the boundary points located in the convex corners of the domain, as the one highlighted in pink in Figure 3.11, the temperature field $\hat{T}$ is calculated in the same way as explained before. Figure 3.14 shows the vertex point (i, j) and its corresponding control area, highlighted in black, and neighboring grid points.

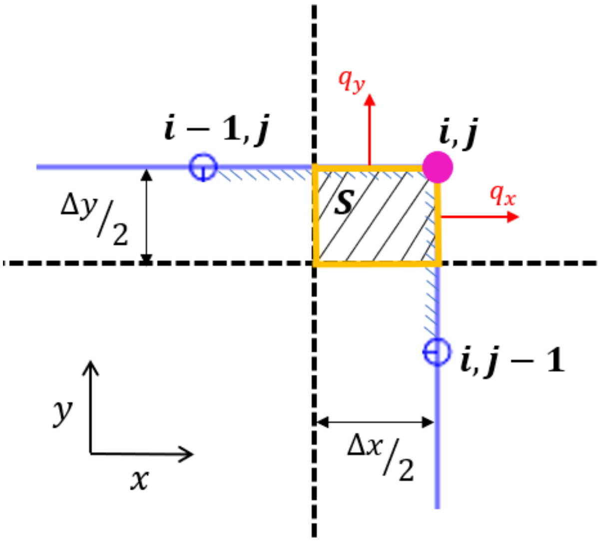

Figure 3.14: Example of a vertex point and its corresponding control area. In this case, the control area, which is highlighted in black shadow, has a size of Δx/2 Δy/2. The heat flow out of the right and top boundaries are highlighted in red. Recall that the yellow lines represent the boundary of the control area.

The left term of Equation 3.44 for this corner point is as follows and it can be seen, that, in this case, the control area has a size of Δx/2 Δy/2

$$\rho c_p \frac{(\hat{T}_{i,j}^{(n+1)} - \hat{T}_{i,j}^{(n)})}{\Delta t} \frac{\Delta x}{2} \frac{\Delta y}{2}. \tag{3.58}$$

The right term of Equation 3.44 is derived as before, by taking into consideration the corresponding boundary conditions in the top and right boundaries of the control area and following Equation 2.29. As shown in Figure 3.14, the heat flux vector of the right boundary is in the positive x-direction. This is because the outward vector normal is **n** = [1, 0] on this boundary. As derived before, the heat flux vector is derived as follows

$$\mathbf{q} = -k \frac{\partial \hat{T}}{\partial \mathbf{x}} \mathbf{n}, \tag{3.59}$$

$$\mathbf{q} = -k \frac{\partial \hat{T}}{\partial \mathbf{x}} \mathbf{n} = -k \left[\frac{\partial \hat{T}}{\partial x}, \frac{\partial \hat{T}}{\partial y} \right] [1, 0]^{\mathrm{T}} = -k \left(\frac{\partial \hat{T}}{\partial x} \right), \tag{3.60}$$

$$-\frac{\partial \tilde{T}}{\partial \mathbf{x}} \cdot \mathbf{n} - \frac{\partial \breve{T}}{\partial \mathbf{x}} \cdot \mathbf{n} = -\left[\frac{\partial \tilde{T}}{\partial x}, \frac{\partial \tilde{T}}{\partial y} \right] [1, 0]^{\mathrm{T}} - \left[\frac{\partial \breve{T}}{\partial x}, \frac{\partial \breve{T}}{\partial y} \right] [1, 0]^{\mathrm{T}} = -\frac{\partial \tilde{T}}{\partial x} - \frac{\partial \breve{T}}{\partial x}, \tag{3.61}$$

$$\frac{\partial \hat{T}}{\partial x} = -\left(\frac{\partial \tilde{T}}{\partial x} + \frac{\partial \breve{T}}{\partial x} \right) \Big|_{i,j}^{n}, \tag{3.62}$$

$$q_x = -k \frac{\partial \hat{T}}{\partial x} = -k \left(-\left(\frac{\partial \tilde{T}}{\partial x} + \frac{\partial \breve{T}}{\partial x} \right) \Big|_{i,j}^{n} \right) = k \left(\frac{\partial \tilde{T}}{\partial x} + \frac{\partial \breve{T}}{\partial x} \right) \Big|_{i,j}^{n}. \tag{3.63}$$

Similarly, the heat flux vector of the top boundary is in the positive y-direction because the outward vector normal is **n** = [0, 1] on this boundary. Then, its heat flux vector is defined as follows

$$\mathbf{q} = -k\frac{\partial \hat{T}}{\partial \mathbf{x}} \cdot \mathbf{n}, \tag{3.64}$$

$$\mathbf{q} = -k\frac{\partial \hat{T}}{\partial \mathbf{x}} \cdot \mathbf{n} = -k\left[\frac{\partial \hat{T}}{\partial x}, \frac{\partial \hat{T}}{\partial y}\right][0,1]^{\mathrm{T}} = -k\left(\frac{\partial \hat{T}}{\partial y}\right), \tag{3.65}$$

$$-\frac{\partial \tilde{T}}{\partial \mathbf{x}} \cdot \mathbf{n} - \frac{\partial \breve{T}}{\partial \mathbf{x}} \cdot \mathbf{n} = -\left[\frac{\partial \tilde{T}}{\partial x}, \frac{\partial \tilde{T}}{\partial y}\right][0,1]^{\mathrm{T}} - \left[\frac{\partial \breve{T}}{\partial x}, \frac{\partial \breve{T}}{\partial y}\right][0,1]^{\mathrm{T}} = -\frac{\partial \tilde{T}}{\partial y} - \frac{\partial \breve{T}}{\partial y}, \tag{3.66}$$

$$\frac{\partial \hat{T}}{\partial y} = -\left(\frac{\partial \tilde{T}}{\partial y} + \frac{\partial \breve{T}}{\partial y}\right)\Bigg|_{i,j}^{n}, \tag{3.67}$$

$$q_y = -k\frac{\partial \hat{T}}{\partial y} = -k\left(-\left(\frac{\partial \tilde{T}}{\partial y} + \frac{\partial \breve{T}}{\partial y}\right)\Bigg|_{i,j}^{n}\right) = k\left(\frac{\partial \tilde{T}}{\partial y} + \frac{\partial \breve{T}}{\partial y}\right)\Bigg|_{i,j}^{n}. \tag{3.68}$$

Therefore, the heat flow out of all four boundaries of the control volume is the following

$$k\frac{\Delta y}{2}\left(\frac{\partial \tilde{T}}{\partial x} + \frac{\partial \breve{T}}{\partial x}\right)\Bigg|_{i,j}^{n} + k\frac{\Delta x}{2}\left(\frac{\partial \tilde{T}}{\partial y} + \frac{\partial \breve{T}}{\partial y}\right)\Bigg|_{i,j}^{n} + k\frac{\Delta y}{2}\frac{\partial \hat{T}}{\partial x}\bigg|_{i-\frac{1}{2},j} + k\frac{\Delta x}{2}\frac{\partial \hat{T}}{\partial x}\bigg|_{i,j-\frac{1}{2}}. \tag{3.69}$$

By approximating the spatial derivatives of Equation 3.69 by first order central difference and combining it with Equation 3.58, results in the following expression

$$\rho c_p \frac{(\hat{T}_{i,j}^{(n+1)} - \hat{T}_{i,j}^{(n)})}{\Delta t}\frac{\Delta x}{2}\frac{\Delta y}{2} + k\frac{\Delta y}{2}\left(\frac{\partial \tilde{T}}{\partial x} + \frac{\partial \breve{T}}{\partial x}\right)\Bigg|_{i,j}^{n} + k\frac{\Delta x}{2}\left(\frac{\partial \tilde{T}}{\partial y} + \frac{\partial \breve{T}}{\partial y}\right)\Bigg|_{i,j}^{n} + k\frac{\Delta y}{2}\frac{(\hat{T}_{i,j}^{(n)} - \hat{T}_{i-1,j}^{(n)})}{\Delta x} + k\frac{\Delta x}{2}\frac{(\hat{T}_{i,j}^{(n)} - \hat{T}_{i,j-1}^{(n)})}{\Delta y} = 0. \tag{3.70}$$

Lastly, Equation 3.71 gives the temperature field $\hat{T}$ of the corner point (i, j) at any time step with the corresponding boundary conditions

$$\hat{T}_{i,j}^{(n+1)} = \hat{T}_{i,j}^{(n)} + \alpha\Delta t\left(\frac{2\hat{T}_{i-1,j}^{(n)} - 2\hat{T}_{i,j}^{(n)}}{(\Delta x)^2} + \frac{2\hat{T}_{i,j-1}^{(n)} - 2\hat{T}_{i,j}^{(n)}}{(\Delta y)^2} - \frac{2}{\Delta x}\left(\frac{\partial \tilde{T}}{\partial x} + \frac{\partial \breve{T}}{\partial x}\right)\Bigg|_{i,j}^{n} - \frac{2}{\Delta y}\left(\frac{\partial \tilde{T}}{\partial y} + \frac{\partial \breve{T}}{\partial y}\right)\Bigg|_{i,j}^{n}\right). \tag{3.71}$$

For the boundary point located in the concave boundary of the domain, the temperature field $\hat{T}$ is calculated similarly. Figure 3.15 shows an inner corner and its corresponding control area. In this case, it can be seen that the size of the control area is $\frac{3}{4}$ ΔxΔy. This point has four neighboring grid points from which the heat flow out of the corresponding boundaries of the control area can be calculated. However, the control area of the inner corner has six boundaries. Thus, applying naively the finite difference method will not take into consideration the heat flow out of the two remaining boundaries. For this reason, the finite volume method is the best approach to obtain an expression of the temperature field $\hat{T}$ for the inner corner (i, j), as it is able to correctly impose the boundary conditions on all the surrounding boundaries of the inner corner.

To obtain the temperature field $\hat{T}$ of the inner corner point (i, j), the analysis is carried out in the same way as before. The left term of Equation 3.44 for the inner corner is as follows

$$\rho c_p \frac{(\hat{T}_{i,j}^{(n+1)} - \hat{T}_{i,j}^{(n)})}{\Delta t}\frac{3}{4}\Delta x\Delta y. \tag{3.72}$$

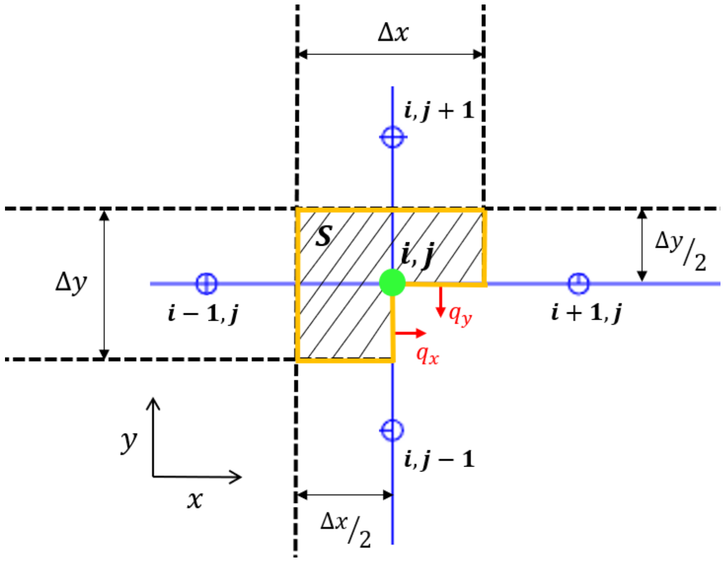

Figure 3.15: Example of an inner corner point and its corresponding control area. In this case, the control area, which is highlighted in black shadow, has a size of $\frac{3}{4}$ ΔxΔy. The heat flux vectors of the boundaries of the control area where the boundary conditions must be applied are highlighted in red.

The right term of Equation 3.44 is derived the same way as before, by correctly imposing the boundary conditions and following Equation 2.29. The heat flux vector, as shown in Figure 3.15, of the right boundary is obtained as follows

$$\mathbf{q} = -k\frac{\partial \hat{T}}{\partial \mathbf{x}} \cdot \mathbf{n}, \tag{3.73}$$

$$\mathbf{q} = -k\frac{\partial \hat{T}}{\partial \mathbf{x}} \cdot \mathbf{n} = -k\left[\frac{\partial \hat{T}}{\partial x}, \frac{\partial \hat{T}}{\partial y}\right][1,0]^{\mathrm{T}} = -k\left(\frac{\partial \hat{T}}{\partial x}\right), \tag{3.74}$$

$$-\frac{\partial \tilde{T}}{\partial \mathbf{x}} \cdot \mathbf{n} - \frac{\partial \check{T}}{\partial \mathbf{x}} \cdot \mathbf{n} = -\left[\frac{\partial \tilde{T}}{\partial x}, \frac{\partial \tilde{T}}{\partial y}\right][1,0]^{\mathrm{T}} - \left[\frac{\partial \check{T}}{\partial x}, \frac{\partial \check{T}}{\partial y}\right][1,0]^{\mathrm{T}} = -\frac{\partial \tilde{T}}{\partial x} - \frac{\partial \check{T}}{\partial x}, \tag{3.75}$$

$$\frac{\partial \hat{T}}{\partial x} = -\left(\frac{\partial \tilde{T}}{\partial x} + \frac{\partial \check{T}}{\partial x}\right)\Bigg|_{i,j}^{n}, \tag{3.76}$$

$$q_x = -k\frac{\partial \hat{T}}{\partial x} = -k\left(-\left(\frac{\partial \tilde{T}}{\partial x} + \frac{\partial \check{T}}{\partial x}\right)\Bigg|_{i,j}^{n}\right) = k\left(\frac{\partial \tilde{T}}{\partial x} + \frac{\partial \check{T}}{\partial x}\right)\Bigg|_{i,j}^{n}. \tag{3.77}$$

The heat flux vector, as highlighted in Figure 3.15, of the bottom boundary is obtained as follows

$$\mathbf{q} = -k\frac{\partial \hat{T}}{\partial \mathbf{x}} \cdot \mathbf{n}, \tag{3.78}$$

$$\mathbf{q} = -k\frac{\partial \hat{T}}{\partial \mathbf{x}}\mathbf{n} = -k\left[\frac{\partial \hat{T}}{\partial x}, \frac{\partial \hat{T}}{\partial y}\right][0,-1]^{\mathrm{T}} = -k\left(-\frac{\partial \hat{T}}{\partial y}\right), \tag{3.79}$$

$$-\frac{\partial \tilde{T}}{\partial \mathbf{x}} \cdot \mathbf{n} - \frac{\partial \check{T}}{\partial \mathbf{x}} \cdot \mathbf{n} = -\left[\frac{\partial \tilde{T}}{\partial x}, \frac{\partial \tilde{T}}{\partial y}\right][0,-1]^{\mathrm{T}} - \left[\frac{\partial \check{T}}{\partial x}, \frac{\partial \check{T}}{\partial y}\right][0,-1]^{\mathrm{T}} = \frac{\partial \tilde{T}}{\partial y} + \frac{\partial \check{T}}{\partial y}, \tag{3.80}$$

$$\frac{\partial \hat{T}}{\partial y} = -\left(\frac{\partial \tilde{T}}{\partial y} + \frac{\partial \check{T}}{\partial y}\right)\Bigg|_{i,j}^{n}, \tag{3.81}$$

$$q_y = -k\left(-\frac{\partial \hat{T}}{\partial y}\right) = -k\left(\frac{\partial \tilde{T}}{\partial y} + \frac{\partial \check{T}}{\partial y}\right)\Bigg|_{i,j}^{n}. \tag{3.82}$$

Combining the heat flow out of the six boundaries of the control volume of Figure 3.15, results in the following expression

$$-k\frac{\Delta y}{2}\frac{\partial \hat{T}}{\partial x}\bigg|_{i+\frac{1}{2},j} - k\Delta x\frac{\partial \hat{T}}{\partial x}\bigg|_{i,j+\frac{1}{2}} + k\Delta y\frac{\partial \hat{T}}{\partial x}\bigg|_{i-\frac{1}{2},j} + k\frac{\Delta x}{2}\frac{\partial \hat{T}}{\partial x}\bigg|_{i,j-\frac{1}{2}} + k\frac{\Delta y}{2}\left(\frac{\partial \tilde{T}}{\partial x} + \frac{\partial \check{T}}{\partial x}\right)\bigg|_{i,j}^{n} - k\frac{\Delta x}{2}\left(\frac{\partial \tilde{T}}{\partial y} + \frac{\partial \check{T}}{\partial y}\right)\bigg|_{i,j}^{n}. \tag{3.83}$$

Then, approximating the spatial derivatives of Equation 3.83 by first order central difference and combining it with Equation 3.72 gives the following expression

$$\begin{aligned}\rho c_p\frac{(\hat{T}_{i,j}^{(n+1)} - \hat{T}_{i,j}^{(n)})}{\Delta t}\frac{3}{4}\Delta x\Delta y - k\frac{\Delta y}{2}\frac{(\hat{T}_{i,j}^{(n)} - \hat{T}_{i+1,j}^{(n)})}{\Delta x} + k\frac{\Delta y}{2}\left(\frac{\partial \tilde{T}}{\partial x} + \frac{\partial \check{T}}{\partial x}\right)\bigg|_{i,j}^{n} + k\frac{\Delta y}{2}\frac{(\hat{T}_{i,j}^{(n)} - \hat{T}_{i-1,j}^{(n)})}{\Delta x}\\ - k\Delta x\frac{(\hat{T}_{i,j}^{(n)} - \hat{T}_{i,j+1}^{(n)})}{\Delta y} - k\frac{\Delta x}{2}\left(\frac{\partial \tilde{T}}{\partial y} + \frac{\partial \check{T}}{\partial y}\right)\bigg|_{i,j}^{n} + k\frac{\Delta x}{2}\frac{(\hat{T}_{i,j}^{(n)} - \hat{T}_{i,j-1}^{(n)})}{\Delta y} = 0.\end{aligned} \tag{3.84}$$

Lastly, Equation 3.85 is obtained to calculate the temperature $\hat{T}$ of the inner corner (i,j) at every time step

$$\begin{aligned}\hat{T}_{i,j}^{(n+1)} = \hat{T}_{i,j}^{(n)} + \frac{2}{3}\alpha\Delta t\Bigg(&\frac{2\hat{T}_{i-1,j}^{(n)} - 3\hat{T}_{i,j}^{(n)} + \hat{T}_{i+1,j}^{(n)}}{(\Delta x)^2} + \frac{\hat{T}_{i,j-1}^{(n)} - 3\hat{T}_{i,j}^{(n)} + 2\hat{T}_{i,j+1}^{(n)}}{(\Delta y)^2} - \frac{1}{\Delta x}\left(\frac{\partial \tilde{T}}{\partial x} + \frac{\partial \check{T}}{\partial x}\right)\bigg|_{i,j}^{n}\\ &+\frac{1}{\Delta y}\left(\frac{\partial \tilde{T}}{\partial y} + \frac{\partial \check{T}}{\partial y}\right)\bigg|_{i,j}^{n}\Bigg).\end{aligned} \tag{3.85}$$

As it can be seen, the finite volume method is an alternative approach to solve heat conduction problems. For the case of non-convex geometries, the finite volume method is able to obtain an expression of the temperature field of the grid points located in concave corners. It can be observed that Equation 3.85 gives an expression to calculate the temperature field $\hat{T}$ for the inner corner of Figure 3.15, where the influence of each neighboring grid point is taken into account, as well as the corresponding boundary conditions. As it was mentioned before, if the finite difference method was used for the inner corners, Equation 3.42 will have been used as its neighbouring grid points are clearly defined at any time step. In this case, the temperature $\hat{T}$ will have been wrongfully calculated as the influence of each neighboring will have been taken equal (without considering the complex geometry) and the boundary conditions would not have been included. For this reason, the finite volume method is specially helpful to solve problems with complex geometry. For the other boundary points, the finite volume method obtains the same expression as the finite difference method. It can be seen that Equation 3.57, obtained with the finite volume method, for the edge point is the same expression in 2D as Equation 3.24, obtained with FD. For the case of the vertex, Equation 3.71 is the same in 2D as Equation 3.37.

4

Results and Discussion

In this chapter, numerical examples will be investigated to illustrate the potential and possible limitations of the anisotropic mirror source in the semi-analytical model. First, simulations will be performed on a convex geometry and the anisotropic mirror source in the semi-analytical model will be compared to the semi-analytical model in [6]. Recall that the semi-analytical model in [6] employed the method of images to analytically enforce the boundary conditions when point heat sources are within a critical distance from the boundary but this method could only be applied to convex domains. Comparing the anisotropic mirror source model with the semi-analytical model in [6] will be useful to determine if the anisotropic mirror sources are capable of correctly enforcing the boundary conditions for point sources near the boundary. Then, to fully investigate the potential of the anisotropic mirror source model, simulations will be developed on a non-convex geometry. The results obtained will be compared to a semi-analytical model with no mirror sources. This comparison will help illustrate the computational efficiency of the anisotropic mirror source in the semi-analytical model.

4.1. Finite convex domain

In this section the temperature distribution predicted by the anisotropic mirror source in the semi-analytical model will be compared to the semi-analytical model proposed in [6]. Recall that the semi-analytical model in [6] proposed to use the superposition principle to combine an analytical solution, which captures the high spatial gradients of point heat sources in semi-infinite space, with a numerical solution that enforces the boundary conditions. For point heat sources within a critical distance from the boundaries, the method of images was employed to analytically enforce the boundary conditions. However, this could only be done for convex geometries. Therefore, the comparison between the anisotropic mirror source model and the semi-analytical model in [6] will be done in a bounded domain of convex geometry, as shown in Figure 4.1.

The dimensions of the part in Figure 4.1a are 2 mm x 2 mm x 2 mm. The part is built by adding layers in the positive z-direction and the bottom surface, ∂V_{bot}, is attached to the base plate. The temperature of the base plate is assumed to be constant and equal to T_c, while the top surface, ∂V_{top}, and the lateral surfaces, ∂V_{lat}, are insulated. The material of the part is Ti-6Al-4V and its properties are shown in Table 4.1. Recall that, in the formulation of the thermal problem (described in Chapter 2), the thermal parameters of the material, that is k, ρ and c_p, were assumed to be constant with temperature.

Table 4.1: Material properties of Ti-6Al-4V

Conductivity k (W/m K)	42
Density ρ (kg/m^3)	4420
Heat capacity c_p (J/kg K)	990
Melting temperature T_m (K)	1928
Absorptivity fraction (-)	0.818

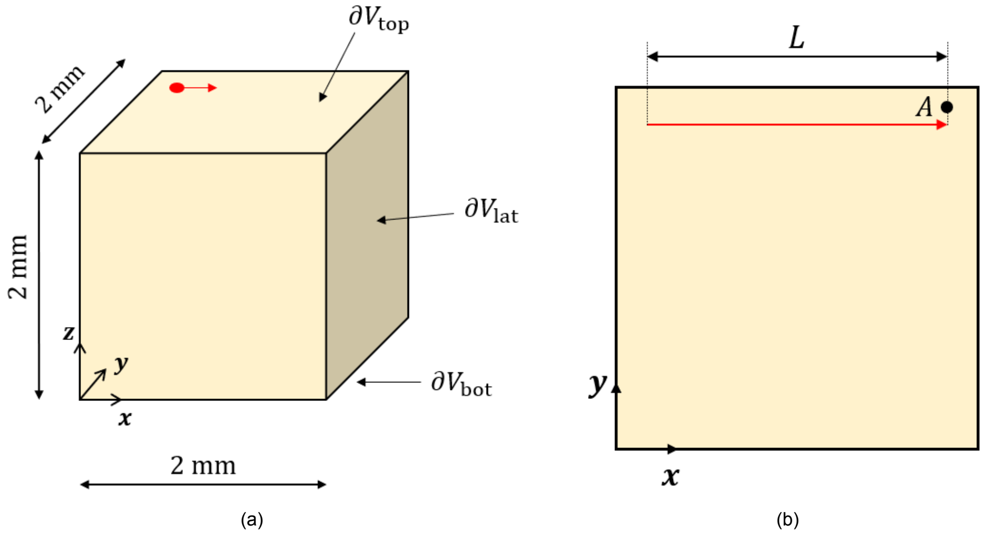

Figure 4.1: (a) Schematic of the body V and its dimensions. The body is attached to the base plate at ∂V_{bot} and the boundaries ∂V_{top} and ∂V_{lat} are insulated. (b) Schematic of the top surface of the body V, where a moving laser heats the body. The scanning laser track, with a length of L = 1.8 mm, is shown in red. The coordinates of point A are (1.9,1.8,2) mm.

The laser scanning vector scans the top surface of the domain. The process parameters of the laser are listed in Table 4.2. In this case, a single laser track is studied as shown in Figure 4.1b. The length of the laser track is L = 1.8 mm.

Table 4.2: Process parameters of the laser beam

Laser power P (W)	35
Laser velocity v_{las} (m/s)	0.3
Laser spot radius r_{las} (μm)	35
Temperature of base plate T_c (K)	453

To obtain the temperature distribution of the domain, the semi-analytical model proposed in [6] and the anisotropic mirror source in the semi-analytical model are both implemented in MATLAB [31]. For the model proposed in [6], the analytical solution, given by $\tilde{T}+\check{T}$, is obtained as described in Sections 2.2 and 2.3, while the analytical solution of the anisotropic mirror source model is obtained as described in Sections 2.2 and 2.4. For both models, the numerical correction, given by $\hat{T}$, is obtained by implementing a finite difference scheme, as described in Section 3.1, where the part in Figure 4.1a is discretized using an equidistant grid of size 0.1 mm, that is $\Delta x = \Delta y = \Delta z = 0.1$ mm. To calculate the numerical time step for the finite difference scheme to be stable and convergent, the following expression will be used.

$$\left(\frac{\alpha}{\Delta x^2}+\frac{\alpha}{\Delta y^2}+\frac{\alpha}{\Delta z^2}\right)\Delta t \leq \frac{1}{2} \tag{4.1}$$

For an equidistant grid of size 0.1 mm, the time step Δt should be smaller than 1.74×10^{-4} s. Nevertheless, it was shown in [6] that temporal convergence was attained for a time step size of 5×10^{-5} s independent of the chosen diffusivity value, α. Therefore, the time step size of 5×10^{-5} s will be used in the finite difference scheme.

4.1.1. Single scan track

In this section a single laser scan track will be studied. Figure 4.2 shows snapshots of the temperature distribution at the top surface of the domain at different instants of time. The temperature fields correspond to the single laser track shown in Figure 4.1b at different time instants. The top row of Figure 4.2 shows the temperature distribution predicted by the semi-analytical model proposed in [6], while the bottom row shows the temperature distribution predicted by the anisotropic mirror source model proposed in this thesis project. It can be seen that Figures 4.2a and 4.2d are obtained at the same time instant, that is t = 0.001 s, Figures 4.2b and 4.2e are obtained at t = 0.003 s, and Figures 4.2c and 4.2f are obtained at t = 0.006 s, which is when the last point source of the laser scan vector is active in the domain. This means that a single laser track is scanned in 0.006 s. It can be observed that the temperature in the domain is between T_c, the temperature of the base plate, and T_m, the melting temperature of the material. In the area where the temperature is T_m, the material has been melted as the temperature of these points are equal to T_m or above (there are points that reach 4500 K). Thus, it can be appreciated that the area near the laser spot has reached the melting point. Furthermore, Figure 4.3 shows snapshots of the temperature distribution of the whole domain at t = 0.006 s. Figure 4.3a shows the temperature distribution predicted by the semi-analytical model in [6], while Figure 4.3b shows the temperature distribution predicted by the anisotropic mirror source model. It can be observed that, in both cases, the temperature of the domain is maintained at the temperature of the base plate, T_c, while the laser scan vector heats up the top surface.

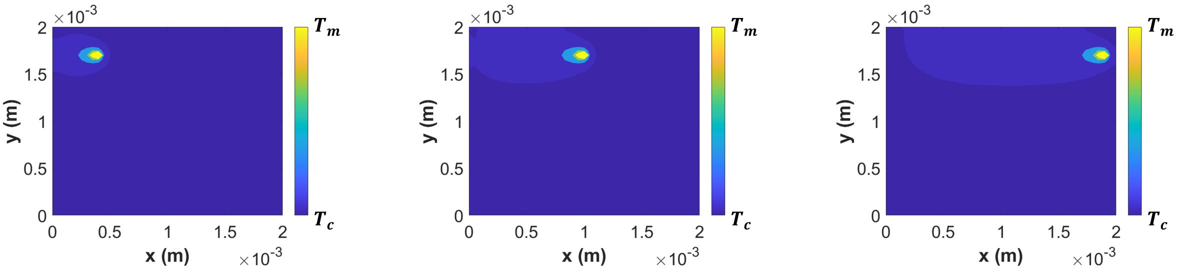

(a) t = 0.001 s (b) t = 0.003 s (c) t = 0.006 s

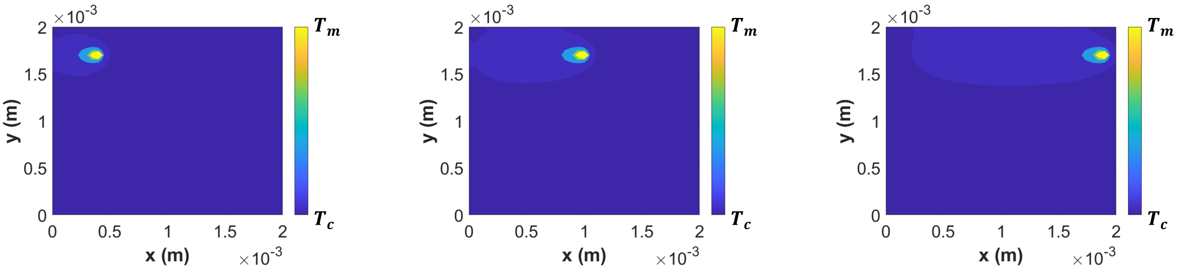

(d) t = 0.001 s (e) t = 0.003 s (f) t = 0.006 s

Figure 4.2: Snapshots of the temperature distribution at the top surface of the domain in Figure 4.1a at different instants in time. The first row, pictures (a), (b) and (c), show the temperature distribution obtained with the semi-analytical model proposed in [6]. The second row, pictures (d), (e) and (f), show the temperature distribution of the semi-analytical model with the anisotropic mirror source. These contour plots were obtained using an equidistant grid size of 0.05 mm to increase the spatial resolution.

To better compare the temperature distribution around the laser beam, Figure 4.4 shows a close up of the contour plots of the temperature distribution around the laser beam of Figures 4.2b and 4.2e, which are obtained at t = 0.003 s. It can be noted that the temperature around the laser spot reaches the melting point, with points reaching 4500 K, while away from the laser spot the temperature is maintained at the temperature of the base plate, T_c. With this close up, it can be seen that the prediction of the temperature distribution done by the anisotropic mirror source model is similar to the prediction obtained with the semi-analytical model proposed in [6].

Furthermore, Figure 4.5 shows the comparison of the thermal history at point A at the top surface predicted by the anisotropic mirror source model, highlighted in red, and the semi-analytical model in [6], highlighted in blue. The location of point A is (1.9, 1.8, 2) mm as shown in Figure 4.1b, which is close to the end of the laser scan track and close to the boundary. Therefore, it can be seen in Figure 4.5 that the temperature peak of the thermal history at point A is attained close to t = 0.006 s. It can be noted that the prediction of the thermal history obtained by the anisotropic mirror source model is similar to the prediction of the semi-analytical model in [6], with a slight difference of 2 K once the temperature peak is surpassed. Nonetheless, as time passes by and heat is diffused it can be seen

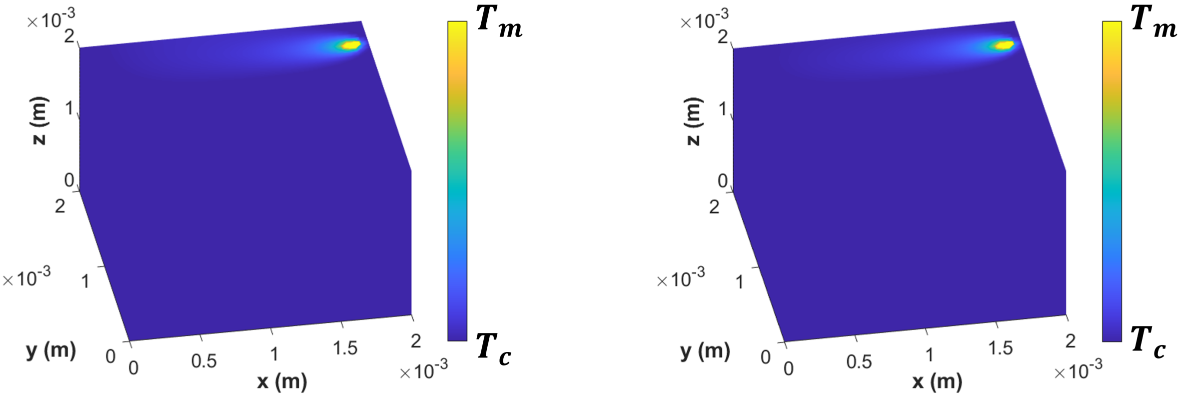

(a) t = 0.006 s (b) t = 0.006 s

Figure 4.3: Snapshots of the temperature distribution of the bounded domain of Figure 4.1a at t = 0.006 s. (a) Shows the temperature distribution of the domain predicted the semi-analytical model proposed in [6]. (b) Shows the temperature distribution of the domain predicted by the the semi-analytical model with the anisotropic mirror source. As before, these contour plots were obtained using an equidistant grid size of 0.05 mm to increase the spatial resolution.

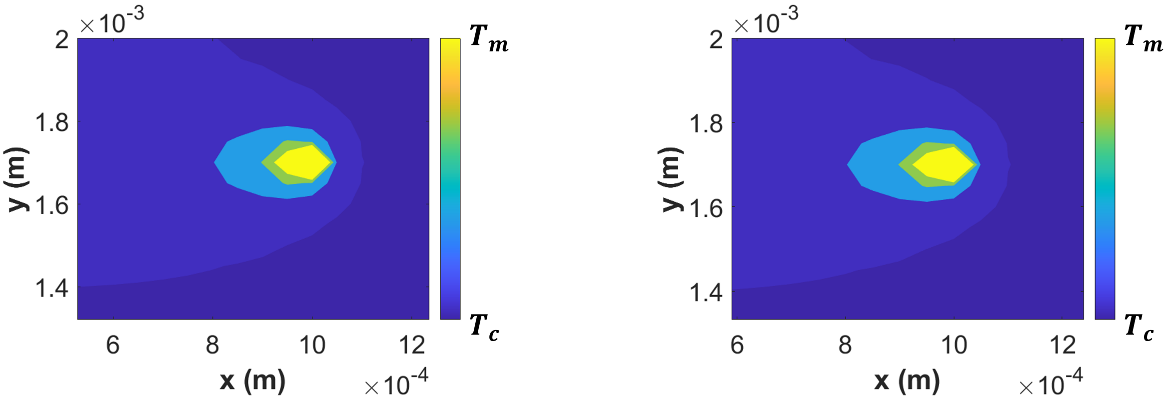

(a) t = 0.003 s (b) t = 0.003 s

Figure 4.4: Close up of the temperature distribution around the laser beam of Figures 4.2b and 4.2e. (a) Shows the temperature distribution around the laser beam predicted by the semi-analytical model proposed in [6]. (b) Shows the temperature distribution around the laser beam predicted by the semi-analytical model with the anisotropic mirror source. As before, these contour plots were obtained using an equidistant grid size of 0.05 mm to increase the spatial resolution.

that both models are identical and converge to the temperature of the base plate, T_c.

4.1.2. Discussion

As it can be seen, the anisotropic mirror source in the semi-analytical model is capable of predicting the thermal fields of a bounded domain of convex geometry, as its results are comparable to the ones obtained by the semi-analytical model in [6]. The anisotropic mirror source is able to predict the temperature distribution in the vicinity of the laser beam with an approximation as good as the semi-analytical model in [6]. Moreover, by studying the thermal history at point A with the anisotropic mirror source model and comparing it to the semi-analytical model in [6], it is clear that anisotropic mirror sources can also be applied to predict the thermal history of any material point of interest in a bounded domain of convex geometry as it correctly imposes the boundary conditions. Furthermore, as mentioned before, the main advantage of the semi-analytical model in [6] is the possibility of obtaining the temperature distribution with a low computational time. In the same way, the anisotropic mirror source model is also able to predict the thermal fields without any additional computational expense. Table 4.3 shows the comparison of the computation time required to scan a single laser scan track by the semi-analytical model in [6] and the anisotropic mirror source model. It can be appreciated that both models are able to predict the total temperature field, T, in less than 3 s of computation time. The simulations were performed in a Intel Core i5-6300HQ processor with a clock speed of 2.30 GHz and with 16 GB RAM.

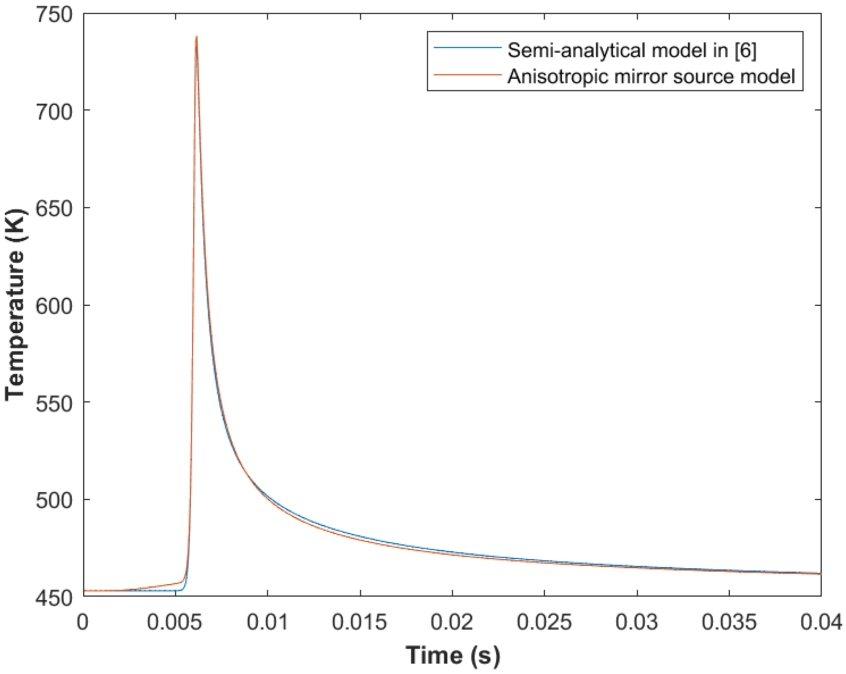

Figure 4.5: Comparison of the thermal history at point A obtained with the semi-analytical model with the anisotropic mirror source, highlighted in red, and the semi-analytical model proposed in [6], highlighted in blue.

Table 4.3: Comparison of the computation time required to scan a single laser scan track by the semi-analytical model in [6] and the anisotropic mirror source in the semi-analytical model.

Temperature field	$T = \tilde{T} + \breve{T} + \hat{T}$
Computation time for semi-analytical model in [6]	2.63 s
Computation time for anisotropic mirror source model	2.35 s

4.2. Finite non-convex domain

In this section the prediction of the thermal field will be done in a bounded domain of non-convex geometry, as shown in Figure 4.6. The body V has an inverted L-shape geometry with dimensions of 2 mm x 2 mm x 2 mm, as shown in Figure 4.6a. The same way as before, the part is built by adding layers in the positive z-direction and the bottom surface, ∂V_{bot}, is attached to the base plate, where the temperature is assumed to be constant and equal to T_c. The top surface, ∂V_{top}, and the lateral surfaces, ∂V_{lat}, are insulated. Similarly as before, the laser scanning vector scans the top surface of the domain. In this case, the laser scan vector is placed close to the concave boundaries. As shown in Figure 4.6b, a single laser track will be studied with a length of L = 0.8 mm. The material of the part is also Ti-6Al-4V and its properties are listed in Table 4.1, while the process parameters of the laser beam are listed in Table 4.2.

As it was explained in Sections 1.3.2 and 2.3, the method of images used in [6] cannot be applied in a non-convex domain as the mirror sources create an erroneous heat flux near the concave boundary, which interferes with the boundary conditions. In this case, the anisotropic mirror source is introduced to allow for the use of the method of images in non-convex geometries. Moreover, as explained in Section 1.3.2, numerical models have been used in literature to obtain the thermal history of complex geometries as the application of analytical models with the method of images is restrictive. Therefore, to be able to determine if the anisotropic mirror source in the semi-analytical model is capable of predicting and obtaining the thermal history of non-convex geometries, its results will be compared to a semi-analytical model with no image sources, which we denote as no mirror source model. In this case, the no mirror source model will make use of the superposition principle described in Section 2.2 in which the temperature field is decomposed as $T = \tilde{T} + \hat{T}$. The same way as before, the tempera-

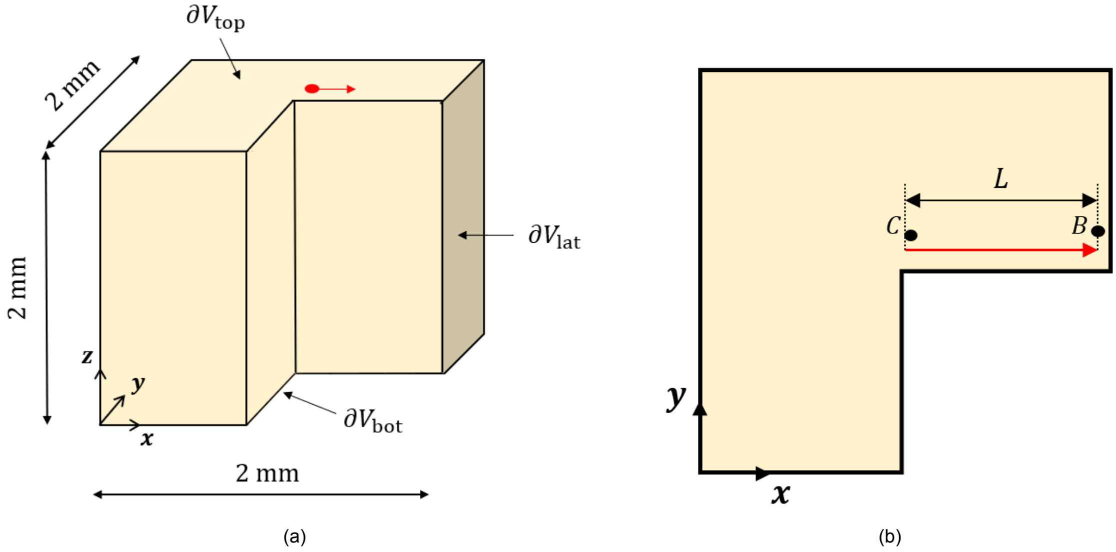

Figure 4.6: (a) Schematic of the non-convex body V and its dimensions. The body is attached to the base plate at ∂V_{bot} and the boundaries ∂V_{top} and ∂V_{lat} are insulated. (b) Schematic of the top surface of the body V, where a moving laser heats the body. The scanning laser track, with a length of L = 0.8 mm, is shown in red. The coordinates of point B and point C are (1.9, 1.2, 2) mm and (1.15, 1.2, 2) mm, respectively.

ture field, $\tilde{T}$, is the analytical solution that captures the high spatial gradients in the vicinity of the laser beam, and the temperature field, $\hat{T}$, is the numerical solution that accounts for the finite dimensions of the domain and enforces the boundary conditions. Moreover, the laser beam is also represented by a finite number of point heat sources. However, in this no mirror source model, as the method of images is not used, when there are point sources within a critical distance from the boundary a finer discretization is required for the numerical solution to capture the steep temperature gradients of $\tilde{T}$. This finer discretization will be applied to the whole domain and it will be in the range of the laser spot radius, which is 10 - 100 μm.

To obtain the temperature distribution of the domain of Figure 4.6a, the anisotropic mirror source in the semi-analytical model and the no mirror source model are both implemented in MATLAB [31]. For the anisotropic mirror source model, the analytical solution of $\tilde{T}$ is obtained following Equation 2.9, while the analytical solution of $\tilde{T}$ is obtained following Equation 2.23. Moreover, the numerical solution of $\hat{T}$ is obtained by implementing the finite volume method described in Section 3.2. Recall that the finite volume method was found effective to properly impose the boundary conditions on non-convex geometries and correctly determine the equations to numerically obtain the temperature field $\hat{T}$. As it was shown in Figure 4.2 in Section 4.1.1, to increase the spatial resolution the results were obtained using an equidistant grid size of 0.05 mm. Thus, this grid size will be used in the anisotropic mirror source model to obtain the temperature distribution of the non-convex domain of Figure 4.6. For this case, for a grid size of $\Delta x = \Delta y = \Delta z = 0.05$ mm, the numerical time step should be lower than 4.33×10^{-5} s, following Equation 4.1. Then, for the numerical solution to be stable and convergent, the numerical step chosen in this case is 1×10^{-5} s. On the other hand, for the no mirror source model, the analytical solution of $\tilde{T}$ is also obtained following Equation 2.9 and the numerical correction of $\hat{T}$ is also obtained through the finite volume method. In this case, a finer discretization is required to correctly obtain the temperature distribution of the non-convex domain. As it was mentioned before, the discretization of the no mirror source model should be in the range of the laser spot radius, which is usually between 10 – 100 μm. In this case, it was found that with a grid size, l_e, of 16.67 μm the boundary conditions are correctly imposed and the thermal fields are accurately obtained. Moreover, with this grid size, the numerical step necessary for the numerical correction to be stable and convergent has to be reduced. In this case, the numerical step chosen is 4×10^{-6} s. To illustrate the difference between the grid used in the anisotropic mirror source model and the no mirror source model, Figure 4.7 shows a close up in an area of 0.1×0.1 mm. It can be seen that in a length of 0.1 mm, with a grid of 0.05 mm for the anisotropic mirror source model, only 3 grid points are used. Meanwhile, in that same length, with a grid size of 16.67 μm for the no mirror source model, 7 grid points are used. By applying this finer discretization in the numerical correction of the no mirror source model, the boundary conditions will be correctly imposed when the point heat sources are close to the boundary. Therefore, the grid size shown in Figure 4.7b and the numerical step of 4×10^{-6} s will be used in the no mirror source model to predict the temperature distribution of the non-convex domain in Figure 4.6a and it will be compared to the prediction obtained with the anisotropic mirror source in the semi-analytical model.

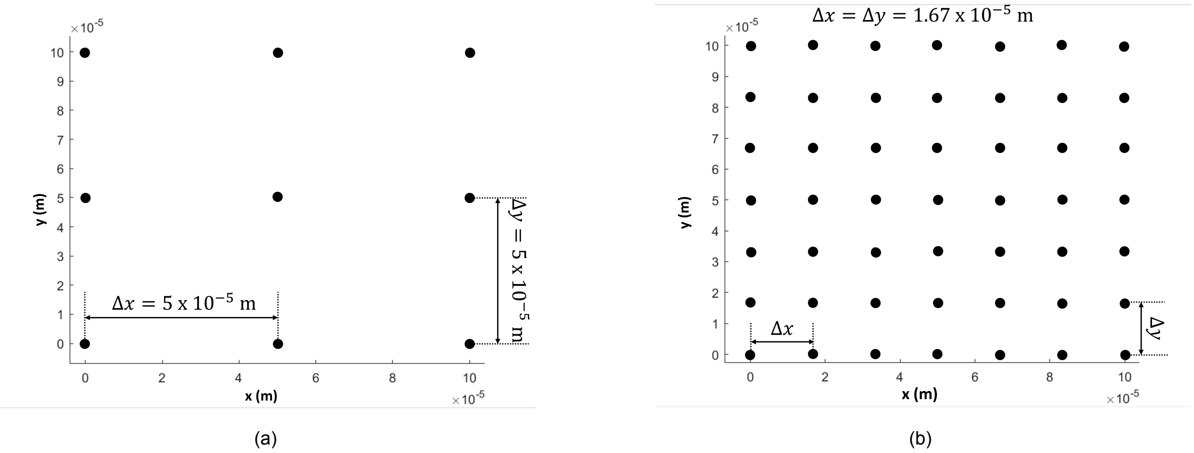

(a)

(b)

Figure 4.7: Schematic illustration of the grid used for the anisotropic mirror source model and the no mirror source model. (a) Shows the grid used for the anisotropic mirror source model, where Δx = Δy = Δz = 0.05 mm. (b) Shows the grid used for the no mirror source model, where Δx = Δy = Δz = 0.0167 mm.

4.2.1. Single scan track

In this section a single laser scan track will be studied. Figure 4.8 shows snapshots of the temperature distribution at the top surface of the domain in Figure 4.6a at different instants of time. The contour plots show different instants of time of the thermal fields of the scan vector shown in Figure 4.6b. The top row of Figure 4.8 shows the temperature distribution predicted by the no mirror source model with a grid size of 16.67 μm, while the bottom row shows the temperature distribution predicted by the anisotropic mirror source in the semi-analytical model. It can be noted that Figures 4.8a and 4.8d are obtained at the same time instant, that is t = 0.0005 s, Figures 4.8b and 4.8e are obtained at t = 0.001 s, and Figures 4.8c and 4.8f are obtained at t = 0.00267 s. Similarly as before, at the instant t = 0.00267 s the last point source of the laser scan vector is active in the domain. Thus, the single scan track vector of Figure 4.6b is scanned in 0.00267 s. As mentioned previously, it can be observed that the temperature in the domain is between T_c and T_m. The area near the laser spot has been melted and there are points with temperatures equal to T_m or above. In addition, Figure 4.9 shows snapshots of the temperature distribution of the whole domain at t = 0.00267 s. Figure 4.9a is obtained by the no mirror source model with a grid size of 16.67 μm, while Figure 4.9b is obtained by the anisotropic mirror source model. It can be noted that the laser beam heats up the top surface, while the rest of the domain is maintained at the temperature of the base plate, T_c. It is important to note that the simulations in Figure 4.9 were performed in a different layer with a height of 1 mm, instead of 2 mm as shown in Figure 4.6a. This change was done to avoid 'Out of Memory' errors in the simulations performed in MATLAB. The grid size of the no mirror source model and the anisotropic mirror source model are maintained the same as mentioned above, that is an equidistant grid size of 16.67 μm for no mirror source model and 0.05 mm for the anisotropic mirror source model. Therefore, as the height is reduced, less grid points are necessary in the z-direction. This allowed for the results to be obtained quicker and avoid memory errors.

With the same approach as before, to compare better the temperature distribution in the vicinity of the laser beam, Figure 4.10 shows a close up of Figures 4.8c and 4.8f. These close ups show the contour plots of the thermal fields around the laser beam at time t = 0.00267 s, which corresponds to the end of the laser scan track. It can be appreciated that, in both models, the area around the laser

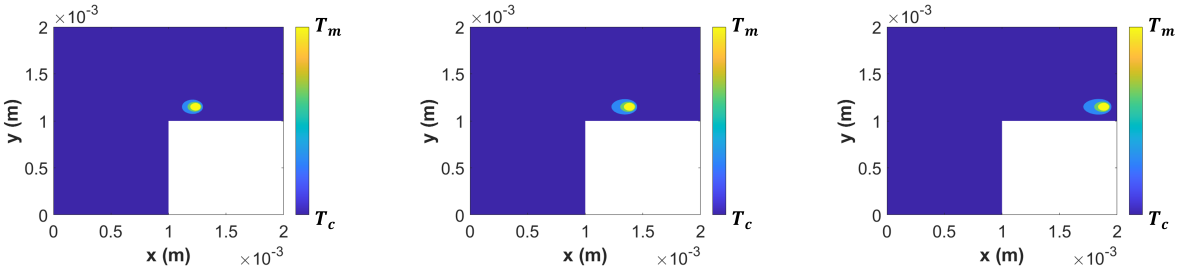

(a) t = 0.0005 s (b) t = 0.001 s (c) t = 0.00267 s

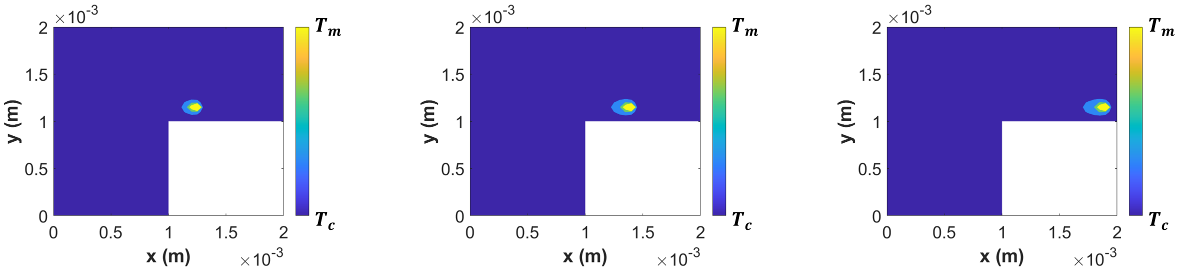

(d) t = 0.0005 s (e) t = 0.001 s (f) t = 0.00267 s

Figure 4.8: Snapshots of the temperature distribution at the top surface of the domain in Figure 4.6a at different instants in time. The first row, pictures (a), (b) and (c), show the temperature distribution obtained with no mirror source model with a grid size of 16.67 μm. The second row, pictures (d), (e) and (f), show the temperature distribution obtained with the semi-analytical model with the anisotropic mirror source with a grid size of 0.05 mm.

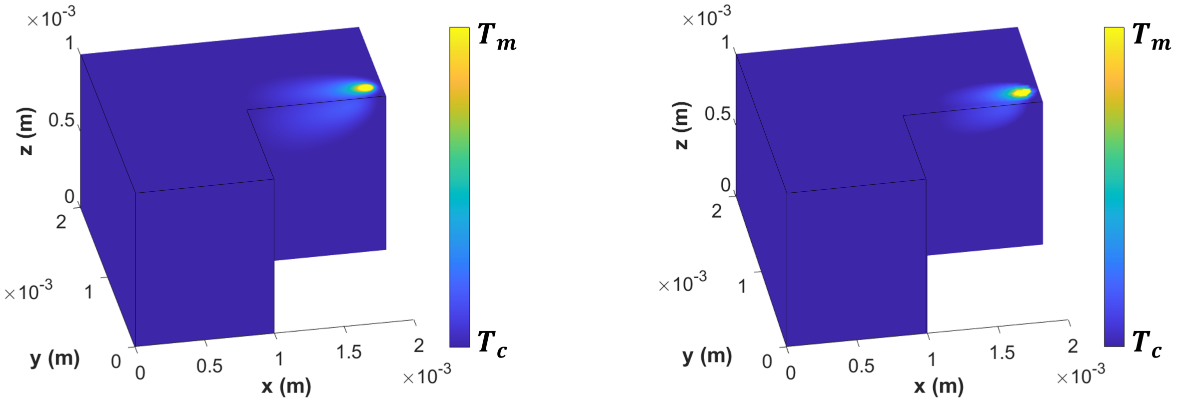

(a) t = 0.00267 s (b) t = 0.00267 s

Figure 4.9: Snapshot of the temperature distribution of the bounded domain of Figure 4.6a. Recall that the simulations are performed in a layer of 1 mm, instead of 2 mm. (a) Shows the temperature distribution of the domain predicted by the no mirror source model with a grid size of 16.67 μm. (b) Shows the temperature distribution of the domain predicted by the semi-analytical model with the anisotropic mirror source with a grid size of 0.05 mm.

spot reaches the melting temperature, with some points reaching 4000 K, while the material points further away are maintained at approximately T_c. Moreover, it can be noted that grid points have been included in Figure 4.10 to show the discretization used in each model: l_e = 16.67 μm for the no mirror source model and l_e = 0.05 mm for the anisotropic mirror source model. It can be seen that in both models the prediction of the contour plots of the melt pool is similar, with just the difference that, due to the finer discretization of the numerical method in the no mirror source model, the circular geometry of the melt pool is approximated better compared to the geometry obtained with the anisotropic mirror source model.

To show better the agreement between the anisotropic mirror source model and the no mirror source model, the thermal history of point B and point C in Figure 4.6b are studied. Figure 4.11 shows the thermal history of point B predicted by the anisotropic mirror source model, highlighted in red, and the

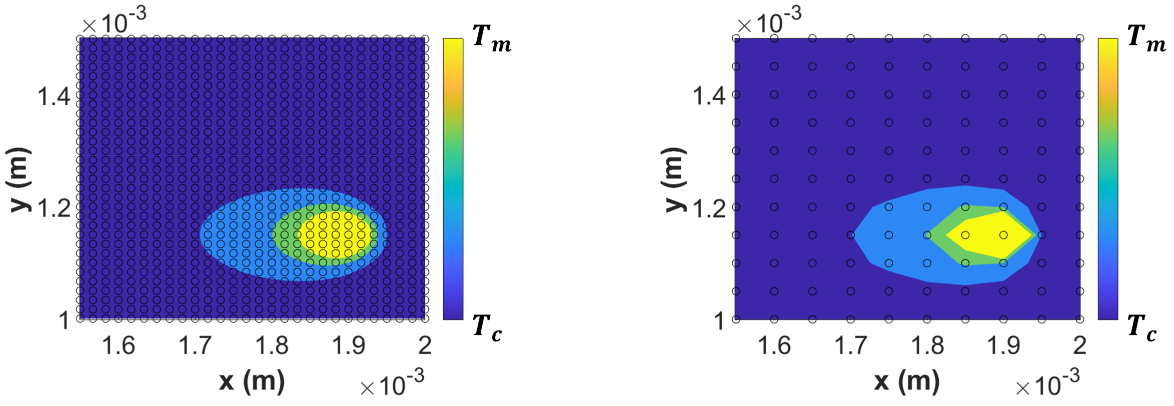

(a) t = 0.00267 s

(b) t = 0.00267 s

Figure 4.10: Close up of the temperature distribution around the laser beam of Figures 4.8c and 4.8f. (a) Shows the temperature distribution around the laser beam of the no mirror source model with a grid size of 16.67 μm. (b) Shows the temperature distribution around the laser beam of the semi-analytical model with the anisotropic mirror source with a grid size of 0.05 mm. The grid points have been included to help visualize the difference between both models.

no mirror source model, highlighted in blue. The location of point B is (1.9, 1.2, 1) mm, as shown in Figure 4.6b, which is at the end of the laser scan track and close to the boundary. Recall that the simulations were performed in a layer of height 1 mm, instead of 2 mm (as it was originally intended). It can be seen that the temperature peak of the thermal history of point B is attained at t = 0.00267 s. Moreover, it can be observed that the prediction obtained by the anisotropic mirror source model is similar to the prediction obtained by the no mirror source model with a grid size of 16.67 μm.

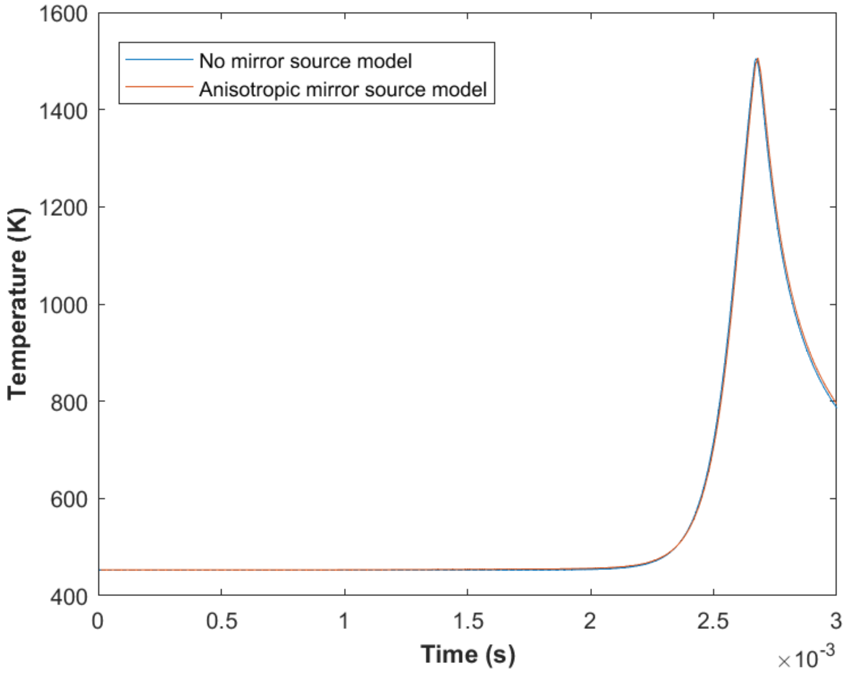

Figure 4.11: Comparison of the thermal history at point B obtained with the anisotropic mirror source in the semi-analytical model, highlighted in red, and the semi-analytical model with no mirror sources, highlighted in blue, with a grid size of l_e = 16.67 μm.

Figure 4.12 shows the thermal history of point C of Figure 4.6b predicted by the anisotropic mirror source model, highlighted in red, and the no mirror source model, highlighted in blue. The location of point C is (1.15, 1.2, 1) mm, which is close to the concave corner and at the beginning of the laser scan track. As before, recall that the simulations were performed in a layer of height 1 mm, instead of 2 mm. In this case, since the point is really close to the start of the scan track, the temperature quickly rises and the temperature peak is attained at approximately t = 0.00025 s. It can be seen that the prediction obtained by the anisotropic mirror source model is also similar to the prediction obtained by the no mirror source model.

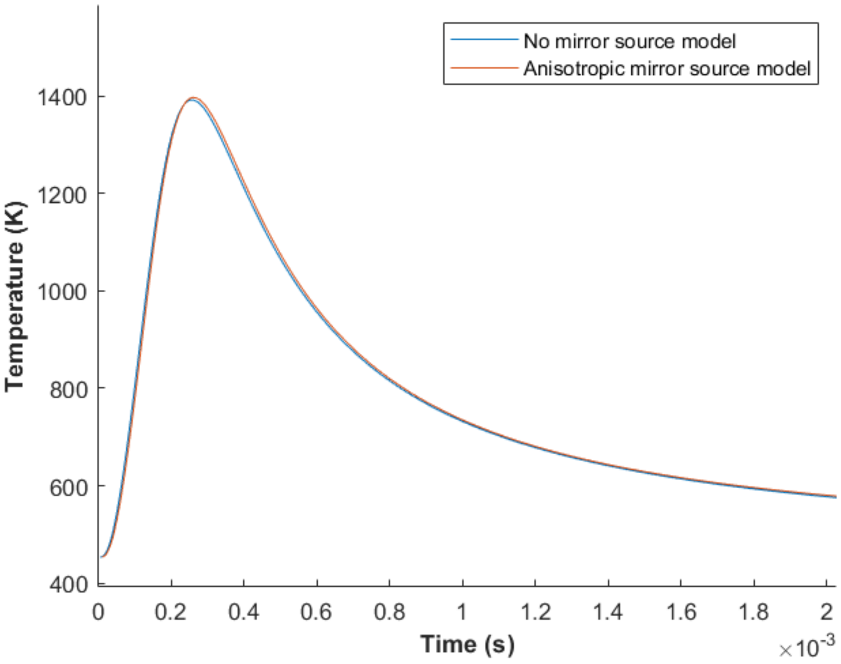

Figure 4.12: Comparison of the thermal history at point C obtained with the anisotropic mirror source in the semi-analytical model, highlighted in red, and the semi-analytical model with no mirror sources, highlighted in blue, with a grid size of l_e = 16.67 μm.

As explained before, the no mirror source model with a grid size of 16.67 μm is capable of accurately predicting the thermal fields of the non-convex domain, as its discretization is fine enough to correctly impose the boundary conditions. Therefore, since the predictions of the thermal history of points B and C obtained by the anisotropic mirror source model are similar to the no mirror source model, it can be concluded that the anisotropic mirror source in the semi-analytical model is capable of predicting the thermal field of the non-convex domain of Figure 4.6a. Moreover, since point C is located close to the concave corner and its respective boundaries, it can be seen that the anisotropic mirror source model is able to correctly impose the boundary conditions near the concave boundary with the use of the method of images.

4.2.2. Contour scan of the non-convex domain

To further study the application of the anisotropic mirror source model to obtain the thermal fields of non-convex geometries, laser scan tracks along the perimeter of the non-convex domain are studied. As shown in Figure 4.13, the laser beam scans counter-clockwise the perimeter of the top surface of the non-convex domain. Moreover, as in Section 4.2, the boundary conditions imposed on the body V are unchanged. The material of the body V is Ti-6Al-4V and its properties are listed in Table 4.1, while the process parameters of the laser beam are listed in Table 4.2.

To obtain the temperature distribution of the non-convex domain with the scan tracks of Figure 4.13, the anisotropic mirror source model is implemented in MATLAB [31] the same way as in Section 4.2. The analytical solution of $\tilde{T}$ is obtained as described in Section 2.2 and the analytical solution of $\check{T}$ is obtained as described in Section 2.4, while the numerical solution of $\hat{T}$ is obtained by implementing the finite volume method described in Section 3.2 with a grid size of 0.05 mm. However, in this case, the

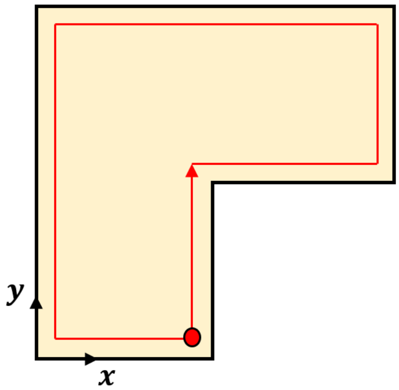

Figure 4.13: Schematic of the laser scan track, shown in red, along the perimeter of the top surface of the non-convex body V of Figure 4.6a. The red point shows the start of the laser scan track.

number of point heat sources that represent the laser scan track increases as the length of the scan track is bigger. In the same way, this increases the number of mirror sources. It can be noted that the formulation of the anisotropic mirror sources is different depending on the location of the laser scan track. The boundary closest to the scan track will define the boundary of reflection of the anisotropic mirror source and, therefore, the anisotropic behavior of the thermal conductivity. Nonetheless, the formulation of the analytical solution of $\breve{T}$ of the anisotropic mirror source will be defined following Equation 2.23 or Equation 2.27.

Figure 4.14 shows the temperature distribution at the top surface of the domain in Figure 4.6a at different instants in time predicted by the anisotropic mirror source model. It can be seen that the snapshots correspond to the laser scan track shown in Figure 4.13, where the laser beam scans the perimeter of the non-convex domain. It can be seen that as the laser beam moves along the perimeter of the domain it heats the top surface. At the vicinity of the laser beam, the temperature reaches the melting point, with parts reaching up to 4500 K, while, for points farther away from the laser beam, the temperature is approximately the temperature of the base plate, T_c.

In this case, a comparison of this study could not be performed with the no mirror source model due to the large number of point heat sources stored in memory, on top of the fine discretization required to correctly impose the boundary conditions and obtain the temperature distribution of the domain.

4.2.3. Computation time

The main advantage of the semi-analytical model proposed in [6] is the low computational time required to predict the temperature distribution of a bounded domain. As mentioned in Section 1.3.2, the semi-analytical approach with the use of the method of images is able to analytically enforce the boundary conditions for point sources close to the boundaries. This allows for the numerical correction to be performed in a coarser grid, which reduces the computational cost. Therefore, by applying the semi-analytical approach with the anisotropic mirror source to obtain the thermal fields of a bounded domain of non-convex geometry the computational cost is also reduced. Table 4.4 shows the comparison of the computation time required to scan a single laser scan track by the no mirror source model with a grid size of 16.67 μm and the anisotropic mirror source model with a grid size of 0.05 mm. It can be noted that the computational cost of the no mirror source model is of 26 hours, while the computational cost of the anisotropic mirror source model is only 37 s. This big difference is due to the fine spatial and temporal discretization used in the no mirror source model in comparison to the discretization used in the anisotropic mirror source model. Recall that the temporal discretization of the no mirror source model was of 4×10^{-6} s, while the anisotropic mirror source model was of 1×10^{-5} s. As in Section 4.1.2, the simulations were performed in an Intel Core i5-6300HQ processor with a clock speed of 2.30 GHz and with 16 GB RAM.

On the other hand, the computational time required to scan the perimeter of the non-convex domain

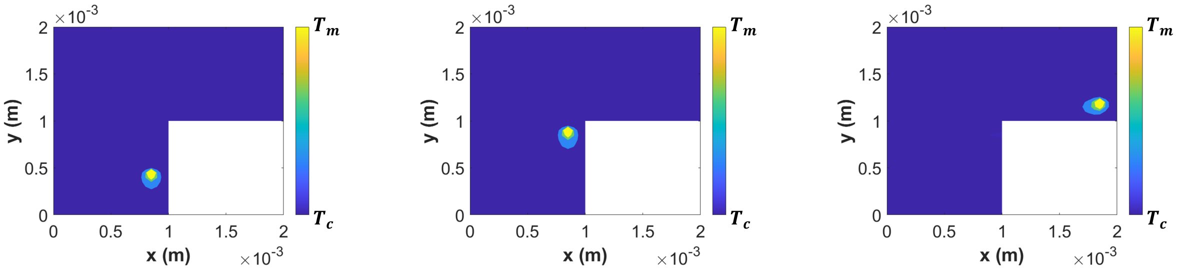

(a) t = 0.001 s (b) t = 0.0025 s (c) t = 0.0055 s

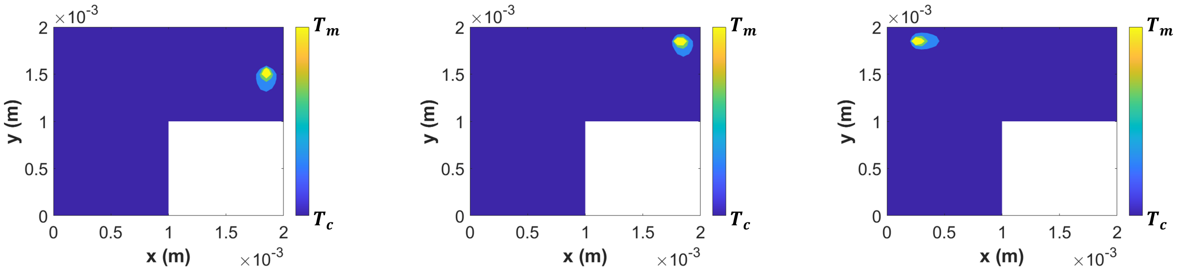

(d) t = 0.0066 s (e) t = 0.0078 s (f) t = 0.013 s

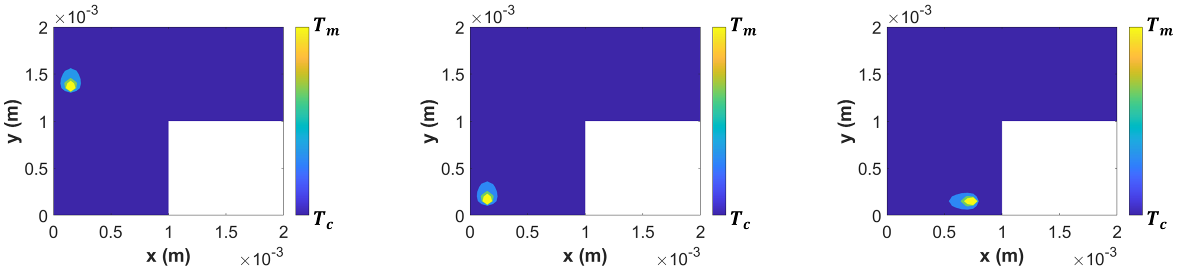

(g) t = 0.015 s (h) t = 0.019 s (i) t = 0.021 s

Figure 4.14: Snapshots of the temperature distribution of the contour scans at the top surface of the domain in Figure 4.6a at different instants in time predicted by the anisotropic mirror source model.

Table 4.4: Comparison of the computation time required to scan a single laser scan track by the no mirror source model and the anisotropic mirror source in the semi-analytical model.

Temperature field	$T = \tilde{T} + \breve{T} + \hat{T}$
Computation time for no mirror source model with grid size 16.67 μm	96397.55 s = 26.77 hours
Computation time for anisotropic mirror source model	37 s

by the anisotropic mirror source model is shown in Table 4.5. In this case, the computational time is decomposed on the time required to obtain each temperature field. It can be seen that the computational time to obtain the analytical solution of $\tilde{T}$ and $\breve{T}$ is similar. However, it is much higher than the computational time required to obtain the numerical solution of $\hat{T}$. This is due to the large number of point heat sources and anisotropic mirror sources stored in memory. Nonetheless, it can be seen that the solution is tractable with a total computational time of 55 minutes.

Table 4.5: Comparison of the computation time required to scan the perimeter of the non-convex domain by the anisotropic mirror source in the semi-analytical model.

Temperature field	$\tilde{T}$	$\breve{T}$	$\hat{T}$	$T = \tilde{T} + \breve{T} + \hat{T}$
Computation time for anisotropic mirror source model	1669 s	1661 s	18 s	3348 s

It is important to emphasize again that the results shown in Section 4.2.1 were obtained on a domain of lower height than the one first chosen to avoid 'Out of Memory' errors in MATLAB. This means that if the simulations were performed in a domain of 2 mm height, more grid points would have been required in the z-direction and the computational expense of the no mirror source model would have been higher. Moreover, the results of the scan tracks along the perimeter of the non-convex domain obtained with the anisotropic mirror source model in Section 4.2.2 could not be compared to the no mirror source model. This was due to the large number of point heat sources stored in memory, as well as the large number of elements required in the discretization of the domain. With the available computer, these results could not be achieved. This shows that by applying the anisotropic mirror source in the semi-analytical model the temperature of non-convex geometries can be obtained with a low computational cost.

4.2.4. Discussion

As it was shown, the anisotropic mirror source in the semi-analytical model is capable of predicting the thermal fields of a non-convex domain with a low computational cost. The results obtained by the anisotropic mirror source model are similar to the results obtained by the no mirror source model with a grid size of 16.67 μm. With a grid size of 16.67 μm or lower, the no mirror source model was capable of correctly imposing the boundary conditions in a bounded domain of non-convex geometry and predicting the temperature distribution of a single laser scan track. Therefore, as the results obtained by the anisotropic mirror source model are similar, it can be concluded that the anisotropic mirror source model is capable of correctly imposing the boundary conditions in a bounded domain of non-convex geometry and predicting the thermal evolution of any material point of interest. Moreover, it is capable of doing this with a low computational cost as shown previously. By employing the anisotropic mirror source in the method of images, the boundary conditions are correctly impose for point heat sources close to a boundary, while with a coarse discretization the numerical correction imposes the boundary conditions in other boundaries. To further illustrate this, Figure 4.15 shows the thermal history of point B of Figure 4.6a predicted by the anisotropic mirror source model, highlighted in red, compared to the no mirror source model with different grid sizes. These grid sizes are l_e = 0.1 mm, 0.03 mm, and 0.01667 mm.

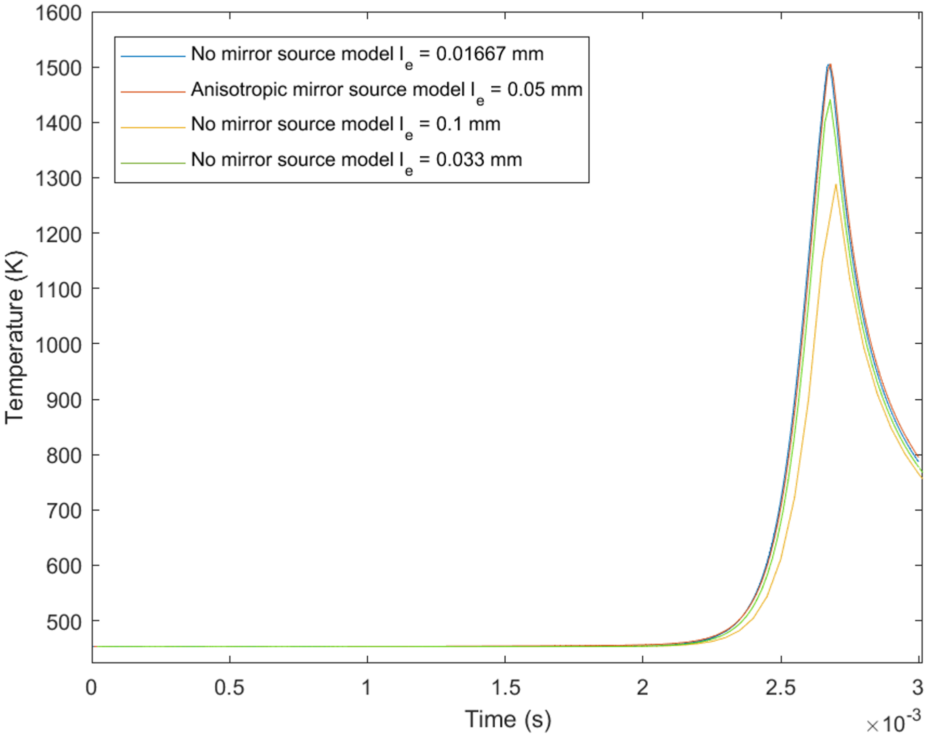

Figure 4.15: Comparison of the thermal history at point B obtained with the anisotropic mirror source in the semi-analytical model (with a grid size of 0.05 mm), highlighted in red, and the no mirror source model with different grid sizes, l_e = 0.1 mm, 0.033 mm and 0.01667 mm, highlighted in yellow, green and blue, respectively.

It can be seen in Figure 4.15 that these grid sizes were used in the no mirror source model to calculate the thermal fields of the non-convex domain and its results are compared to the anisotropic mirror source model. The results attained with the grid sizes l_e = 0.01 mm and 0.033 mm (highlighted in yellow and green, respectively, in Figure 4.15) are not comparable to the result obtained with the anisotropic mirror source model. There is a difference of approximately 220 K in the peak temperature between the numerical model with grid size 0.01 mm and the anisotropic mirror source model, and approximately 65 K in the peak temperature with the grid size 0.033 mm compared to the anisotropic mirror source model. Moreover, it can be noted that as the grid size decreases, the results converge to the ones obtained by the anisotropic mirror source model (which has a grid size of 0.05 mm), and the no mirror source model with grid size 16.67 μm is capable of obtaining comparable results. This results are as expected: to be able to correctly impose the boundary conditions in a bounded domain without the use of the method of images an extremely fine discretization is required. Since the results obtained by the anisotropic mirror source model are similar to the results obtained by the no mirror source model with a grid size of 16.67 μm and there is a big difference with the results obtained by the no mirror source model with a coarser grid, it is clear that the anisotropic mirror source model is capable of predicting the thermal fields of a bounded domain of non-convex geometry.

5

Conclusion and Recommendations

5.1. Conclusion

In this report, a thermal model was presented to model the thermal fields of bounded domains of non-convex geometry. The model was based on the semi-analytical approach proposed by Yang et al. [6], in which the superposition principle and the method of images is used. In this case, in the thermal model proposed in this thesis, a correction to the method of images is performed so that image sources can be applied in non-convex geometries.

The semi-analytical approach is used in this thermal model, in which the laser scan vector is represented as a finite number of point heat sources. The formulation of the proposed thermal model is based on the superposition principle that decomposes the thermal fields in the temperature fields due to the point heat sources in semi-infinite space, which are obtained analytically, and correction fields that impose the boundary conditions. To correctly enforce the boundary conditions, two correction fields are included in the formulation. First, the method of images is applied to analytically account for the steep temperature gradients that arise at the boundary when point heat sources are located within a critical distance. In this case, for non-convex geometries, the anisotropic mirror source is introduced to be able to account for the steep temperature gradients that arise at the boundary of concave geometries without compromising the boundary conditions. The anisotropic mirror source is capable of this due to the anisotropic behavior of the thermal conductivity. Depending on the boundary with respect to which the image source is reflected, the thermal conductivity will be different. This will allow to enforce analytically the boundary condition on the concave boundaries located near the point heat sources, while avoiding the creation of steep temperature gradients in other boundaries. Secondly, to ensure that the boundary conditions on the rest of the boundaries are imposed, a numerical correction field is obtained through the finite volume method. In this case, since the steep temperature gradients are handled analytically, the numerical correction field can be performed on a coarse mesh.

It was shown that the anisotropic mirror source model is capable of predicting the thermal fields of a bounded domain of convex geometry, as its results are comparable to the prediction obtained with the semi-analytical model proposed in [6]. Performing this comparison allows to determine that the anisotropic mirror source model ensures the boundary conditions when the point heat sources are located within a critical distance from a convex boundary. Moreover, to fully study the potential of the anisotropic mirror source model, the prediction of the thermal fields was performed in a bounded domain of non-convex geometry. The results obtained by the anisotropic mirror source model were compared to a semi-analytical model with no mirror sources. The no mirror source model required a fine discretization to account for the steep temperature gradients as it did not include the method of images in its formulation. It was shown that the anisotropic mirror source model is capable of predicting the temperature field of non-convex geometries by correctly imposing the boundary conditions, as its results were comparable to the results obtained with the no mirror source model of fine discretization.

The main advantages of this formulation are that the anisotropic mirror source model allows to obtain the thermal fields of non-convex geometries by applying the method of images in the semi-analytical approach and it has a low computational cost. It was shown that the anisotropic mirror source model is capable of predicting the thermal fields of a single laser scan track approximately 2530 times faster

than the no mirror source model.
However, a limitation of the anisotropic mirror source model is that this formulation can only be applied to straight boundaries. For curved concave boundaries the formulation cannot be applied as the anisotropic behavior of the thermal conductivity is dependant on the boundary of reflection parallel to the Cartesian coordinates system. Curved concave boundaries are not parallel to any Cartesian coordinates axes, and, therefore, anisotropic mirror sources cannot be created when point heat sources are close to it.
Therefore, to further improve this thermal model, in the next section, recommendations for future work are presented.

5.2. Recommendations

To further improve this thermal model, the following recommendations are presented:

- Properly compare with a no mirror source model the results obtained of the scanning of the perimeter of the non-convex domain. In this case, the no mirror source model could be optimized to reduce the number of point sources stored in memory by locally storing these variables.
- Combine this thermal model with a mechanical model to investigate the residual stresses and possible defects of parts of non-convex geometry, specially to study the defects that can arise at the concave corners.
- On the same note as the previous recommendation, investigate the application of different scanning strategies and how it affects the thermal history and the residual stresses of the part, specially on the concave corners.
- Investigate the possibility of combining the method of images proposed in [6] with the anisotropic mirror source model in parts that have both convex and concave boundaries. Specially investigate the critical distance at which the regular mirror sources will affect concave boundaries.
- Investigate the application of the anisotropic mirror source model in geometries that are more common in the industry. In this report, the domain studied was a concave polyhedron with a 270º L-shaped corner. A proposal is to investigate parts with corners that have angles between 180º to 270º or 270º to 360º, as shown in Figure 5.1a, or parts with cavities as shown in Figure 5.1b.
- Investigate the possibility of applying the anisotropic mirror source model in curved concave boundaries. As it was mentioned before, as of now, the proposed thermal model cannot be applied in curved concave boundaries. A proposal is to investigate the possibility of combining the anisotropic mirror source model with a mesh refinement in the vicinity of the curved concave boundary. In this case, to be able to apply the mesh refinement, it is more suitable to perform a finite element analysis.

(a)

(b)

Figure 5.1: (a) Schematic of a concave corner with an angle between 270º to 360º. (b) Schematic of a part with a cavity.

Bibliography

[1] N. Guo and M. Leu. "Additive manufacturing: technology, applications and research needs". In: *Frontiers of Mechanical Engineering* 8.3 (2013), pp. 215–243. DOI: `10.1007/s11465-013-0248-8`.

[2] D. Herzog, V. Seyda, and E. Wycisk et al. "Additive manufacturing of metals". In: *Acta Materialia* 117 (2016), pp. 371–392. URL: `http://dx.doi.org/10.1016/j.actamat.2016.07.019`.

[3] R. Brighenti, M. P. Cosma, and L. Marsavina et al. "Laser-based additively manufactured polymers: a review on processes and mechanical models". In: *Journal of Materials Science* 56 (2021), pp. 961–998. URL: `https://doi.org/10.1007/s10853-020-05254-6`.

[4] I. Gibson, D. Rosen, and B. Stucker et al. "Introduction and Basic Principles". In: *Additive Manufacturing Technologies*. Springer, Cham, 2021. Chap. 1, pp. 1–21. URL: `https://doi.org/10.1007/978-3-030-56127-7`.

[5] I. Gibson, D. Rosen, and B. Stucker et al. "Generalized Additive Manufacturing Process Chain". In: *Additive Manufacturing Technologies*. Springer, Cham, 2021. Chap. 3, pp. 53–76. URL: `https://doi.org/10.1007/978-3-030-56127-7`.

[6] Y. Yang, M. Knol, and F. van Keulen et al. "A semi-analytical thermal modelling approach for selective laser melting". In: *Additive Manufacturing* 21 (2018), pp. 284–297. URL: `https://doi.org/10.1016/j.addma.2018.03.002`.

[7] T. D. Ngo, A. Kashani, and G. Imbalzano et al. "Additive manufacturing (3D printing): A review of materials, methods, applications and challenges". In: *Composites Part B* 143 (2018), pp. 172–196. URL: `https://doi.org/10.1016/j.compositesb.2018.02.012`.

[8] I. Gibson, D. Rosen, and B. Stucker et al. "Industrial Drivers for AM Adoption". In: *Additive Manufacturing Technologies*. Springer, Cham, 2021. Chap. 21, pp. 623–646. URL: `https://doi.org/10.1007/978-3-030-56127-7`.

[9] Y. Zhang, W. Jarosinski, and Y. Jung et al. "Additive manufacturing processes and equipment". In: *Additive Manufacturing: Materials, Processes, Quantifications and Applications*. Ed. by J Zhang and Y Jung. Butterworth-Heinemann, 2018. Chap. 2, pp. 39–51. DOI: `http://dx.doi.org/10.1016/B978-0-12-812155-9.00002-5`.

[10] M. Gouge and P. Michaleris. "An Introduction to Additive Manufacturing Processes and Their Modelling Challenges". In: *Thermo-Mechanical Modeling in Additive Manufacturing*. Ed. by M Gouge and P Michaleris. Butterworth-Heinemann, 2018. Chap. 1, pp. 3–18. DOI: `10.1016/B978-0-12-811820-7.00002-1`.

[11] W. Frazier. "Metal Additive manufacturing: A Review". In: *Materials Engineering and Performance* 23.6 (2014), pp. 1917–1928. DOI: `10.1007/s11665-014-0958-z`.

[12] W. Zhang, M. Tong, and N. M. Harrison. "Scanning strategies effect on temperature, residual stress and deformation by multi-laser beam powder bed fusion manufacturing". In: *Additive Manufacturing* 36 (2020). URL: `https://doi.org/10.1016/j.addma.2020.101507`.

[13] D. Mejia-Parra, D. Montoya-Zapata, and A. Arbelaiz et al. "Fast Analytic Simulation for Multi-Laser Heating of Sheet Metal in GPU". In: *Materials* 11 (2018), p. 2078. DOI: `10.3390/ma11112078`.

[14] M. Bayat, W. Dong, and J. Thorborg et al. "A review of multi-scale and multi-physics simulations of metal additive manufacturing processes with focus on modeling strategies". In: *Additive Manufacturing* 47 (2021), p. 102278. ISSN: 2214-8604. DOI: `10.1016/j.addma.2021.102278`.

[15] S. Afazov, A. Roberts, and L. Wright et al. "Metal powder bed fusion process chain: an overview of modelling techniques". In: *Progress in Additive Manufacturing* (2021). DOI: `10.1007/s40964-021-00230-1`.

[16] J. Zhang, Y. Zhang, and W. H. Lee et al. "A multi-scale multi-physics modeling framework of laser powder bed fusion additive manufacturing process". In: *Metal Powder Report* 73.3 (2018), pp. 151–157. DOI: `10.1016/j.mprp.2018.01.003`.

[17] H. Jia, H. Sun, and H. Wang. "Scanning strategy in selective laser melting (SLM): a review". In: *International Journal of Advanced Manufacturing Technology* 113 (2021), pp. 2413–2435. URL: `https://doi.org/10.1007/s00170-021-06810-3`.

[18] M. Masoomi, S. M. Thompson, and N. Shamsaei. "Quality part production via multi-laser additive manufacturing". In: *Manufacturing Letters* 13 (2017), pp. 15–20. URL: `https://doi.org/10.1016/j.mfglet.2017.05.003`.

[19] S. Zou, H. Xiao, and F. Ye et al. "Numerical analysis of the effect of the scan strategy on the residual stress in the multi-laser selective laser melting". In: *Results in Physics* 20 (2020). ISSN: 2211-3797. URL: `https://doi.org/10.1016/j.rinp.2020.103005`.

[20] Z. Luo and Y. Zhao. "A survey of finite element analysis of temperature and thermal stress fields in powder bed fusion Additive Manufacturing". In: *Additive Manufacturing* 21 (2018), pp. 318–332. DOI: `10.1016/j.addma.2018.03.022`.

[21] B. Cheng, S. Shrestha, and K. Chou. "Stress and deformation evaluations of scanning strategy effect in selective laser melting". In: *Additive Manufacturing* 12 (2016), pp. 240–251. URL: `https://doi.org/10.1016/j.addma.2016.05.007`.

[22] M. Masoomi, S. M. Thompson, and N. Shamsaei. "Laser powder bed fusion of Ti-6Al-4V parts: Thermal modeling and mechanical implications". In: *International Journal of Machine Tools and Manufacture* 118-119 (2017), pp. 73–90. DOI: `10.1016/j.ijmachtools.2017.04.007`.

[23] Y. Yang, F. van Keulen, and C. Ayas. "A computationally efficient thermal model for selective laser melting". In: *Additive Manufacturing* 31 (2020). URL: `https://doi.org/10.1016/j.addma.2019.100955`.

[24] J. Steuben, A. Birnbaum, and J. Michopoulos et al. "Enriched analytical solutions for additive manufacturing modeling and simulation". In: *Additive Manufacturing* 25 (2019), pp. 437–447. URL: `https://doi.org/10.1016/j.addma.2018.10.017`.

[25] Y. A. Cengel and A. J. Ghajar. "Heat Conduction Equation". In: *Heat and Mass Transfer: Fundamentals and Applications*. New York: McGraw-Hill Education, 2015. Chap. 2, pp. 67–142.

[26] L. C. Evans. *Partial Differential Equations*. American Mathematical Society, 1998.

[27] H. S. Carslaw and J. C. Jaeger. "Linear Flow of Heat: The Infinite and Semi-Infinite Solid". In: *Conduction of Heat in Solids*. London: Oxford University Press, 1959. Chap. 2, pp. 50–91.

[28] H. S. Carslaw and J. C. Jaeger. "The Use of Sources and Sinks in Cases of Variable Temperature". In: *Conduction of Heat in Solids*. London: Oxford University Press, 1959. Chap. 10, pp. 255–281.

[29] J. Taler and P. Duda. "Finite Difference Method". In: *Solvind Direct and Inverse Heat Conduction Problems*. Berlin, Heidelberg: Springer Berlin Heidelberg, 2006. Chap. 21, pp. 605–657. URL: `https://doi.org/10.1007/978-3-540-33471-2_21`.

[30] J.C. Tannehill, D.A. Anderson, and R.H. Pletcher. *Computational Fluid Mechanics and Heat Transfer*. 2nd ed. Taylor Francis, 1984.

[31] The MathWorks Inc. *MATLAB version: 9.13.0 (R2022b)*. Natick, Massachusetts, United States, 2022. URL: `https://www.mathworks.com`.